Automated quantitative analysis of first-pass myocardial perfusion magnetic resonance imaging data

Scannell, Cian

Awarding institution:
King's College London

Automated quantitative analysis of first-pass myocardial perfusion magnetic resonance imaging data

Cian Michael Scannell

School of Biomedical Engineering and Imaging Sciences
King's College London

This dissertation is submitted for the degree of
Doctor of Philosophy

Supervisors:
Dr. A. Chiribiri
Dr. J. Lee

October 2020

Declaration

I hereby declare that except where specific reference is made to the work of others, the contents of this dissertation are original and have not been submitted in whole or in part for consideration for any other degree or qualification in this, or any other university. This dissertation is my own work except where explicitly stated otherwise in the text

Cian Michael Scannell
October 2020

Acknowledgements

I am indebted to my primary supervisor Amedeo Chiribiri for his hard-work and kindness through-out the four years of this PhD. None of this would have been possible without his support and guidance. I would also like to thank Jack Lee for his productive comments and advice.

I am grateful to Philips Healthcare for co-funding my studentship and would like to especially thank Marcel Breeuwer for his mentorship and Torben Schneider for his scanner and software advice.

I would also like to thank all my collaborators for making this work possible. In particular, I was extremely lucky to work with Mitko Veta and Adriana Villa, who taught me so much. Without their help and fruitful discussions, this would have been a much different thesis.

I was fortunate to do this work in the CDT in Medical Imaging and I am grateful for all the extra help that was provided by the CDT. I am also thankful to the close friends that I met here: Pam, Dan, George, and Marina who made this process a lot more enjoyable.

Finally, I would like to thank my family, and most of all my parents, not just for their support during my PhD but for everything leading up to this. I couldn't have done it without you.

Abstract

Coronary artery disease (CAD) remains the world's leading cause of mortality and the disease burden is continually expanding as the population ages. Recently, the MR-INFORM randomised trial has demonstrated that the management of patients with stable CAD can be guided by stress perfusion cardiovascular magnetic resonance (CMR) imaging and it is non-inferior to the using the invasive reference standard of fractional flow reserve. The benefits of using stress perfusion CMR include that it is non-invasive and significantly reduces the number of unnecessary coronary revascularisations. As compared to other ischaemia tests, it boasts a high spatial resolution and does not expose the patient to ionising radiation. However, the main limitation of stress perfusion CMR is that the diagnostic accuracy is highly dependent on the level of training of the operator, resulting in the test only being performed routinely in experienced tertiary centres.

The clinical translation of stress perfusion CMR would be greatly aided by a fully-automated, user-independent, quantitative evaluation of myocardial blood flow. This thesis presents major steps towards this goal: robust motion correction, automated image processing, reliable quantitative modelling, and thorough validation. The motion correction scheme makes use of data decomposition techniques, such as robust principal component analysis, to mitigate the difficulties in image registration caused by the dynamic contrast enhancement. The motion corrected image series are input to a processing pipeline which leverages the recent advances in image processing facilitated by deep learning. The pipeline utilises convolutional neural networks to perform a series of computer vision tasks including myocardial segmentation and right ventricular insertion point detection. The tracer-kinetic model parameters are subsequently estimated using a Bayesian inference framework. This incorporates the prior information that neighbouring voxels are likely to have similar kinetic parameters and thus improves the reliability of the estimated parameters. The full process is validated in a well characterised patient population against coronary angiography and invasive measurements. It is shown to be accurate at detecting reductions in myocardial blood flow while further discriminating between patients with no significant CAD and those with obstructed coronary arteries or microvascular dysfunction.

Table of contents

List of figures

List of tables

Chapter 1

Introduction

1.1 Motivation

Stress perfusion cardiovascular magnetic resonance (CMR) imaging has a class IA indication in the European guidelines for the evaluation of patients with an intermediate risk of coronary artery disease [1]. However, myocardial perfusion imaging is performed far less frequently with CMR than with the alternative nuclear imaging approaches: single-photon emission computed tomography (SPECT) and positron emission tomography (PET). This is despite the fact that CMR boasts superior spatial resolution, a lack of ionising radiation, and can also provide a full assessment of cardiac function and tissue viability. Furthermore, multiple trials and studies have shown CMR to have at least comparable diagnostic accuracy to SPECT [2, 3] and to be non-inferior to invasive measurements for the management of patients [4].

In fact, stress perfusion CMR is primarily used in highly experienced centres and there is a need to encourage its adoption in less specialised centres. This need, however, is hampered by the dependence of the diagnostic accuracy of the test on the level of training of the operator [5]. A possible solution to this is the quantification of myocardial perfusion which offers a user-independent assessment of the images that could facilitate the adoption of stress perfusion CMR in less specialised centres.

The aim of this thesis is to develop methods to overcome the technical difficulties of quantitative myocardial perfusion CMR. Challenges such as respiratory motion, the reliability of the analysis, and the time consuming processing have lead to the approach only being used as a research tool and not in clinical practice. This thesis deals with the contrast-enhancement during motion compensation in a principled manner, introduces more robust kinetic parameter estimation approaches and combines this with a deep learning-based image processing pipeline to make the analysis fully automated. The initial clinical validation of the proposed methods is also reported.

1.2 Contribution of the thesis

The original contributions of the thesis can be summarised as follows:

- **Robust motion compensation.** The motion compensation of myocardial perfusion CMR, using image registration, is difficult due to the rapidly changing contrast during the passing of the gadolinium bolus. This invalidates the assumptions of the similarity measures optimised in the image registration. This work proposes the use of robust principal component analysis (RPCA) to decompose the baseline signal from the dynamic contrast-enhancement. Image registration is then more readily applied in the absence of the dynamic contrast-enhancement. The proposed approach is evaluated qualitatively by expert clinicians, as well as quantitatively.

- **Fully automated image processing.** Deep learning is used to automate the computer vision tasks required for the quantitative modelling. This includes the automation of the myocardial segmentation, the identification of the arterial input function, and the detection of the right ventricular insertion points. Each step is evaluated individually using a suitable metric and additionally, the full automated pipeline is compared to the manual processing.

- **Reliable quantitative modelling.** The identification of the tracer-kinetic parameters from the imaging data is an ill-posed inverse problem, and as such, the estimated values are subject to uncertainties [6]. This work introduces Bayesian inference as a principled approach to incorporate prior information in the parameter estimation. In particular, the prior knowledge that neighbouring pixels are likely to have similar kinetics is used to constrain the parameter estimation and improve reliability.

Furthermore, an initial assessment of the performance of the proposed pipeline in comparison to invasive coronary angiography. This is performed on an external validation set (i.e, none of the patient data considered in this assessment has been used in the development of any of the underlying methods) to give an accurate reflection of the clinical performance.

1.3 Outline of the thesis

The thesis is organised into 7 further chapters, the contents of which are:

- **Chapter 2:** a brief background on the physiology and pathophysiology of coronary artery disease is first provided. The chapter subsequently gives an overview of some of the imaging approaches to diagnosing coronary artery disease.
- **Chapter 3:** gives an introduction to myocardial perfusion CMR. This includes the background on the MR acquisition of the data, the tracer-kinetic modelling, and a review of the state-of-the-art approaches in the literature.
- **Chapter 4:** introduces the problem of motion compensation of myocardial perfusion CMR, and describes RPCA and how it is used. The proposed approach to the problem is then described and evaluated.
- **Chapter 5:** firstly, introduces the image processing problems and gives the requisite deep learning background. It then describes the automated image processing pipeline and considers its application and evaluation. The pipeline is further compared to the manual processing by expert operators.
- **Chapter 6:** discusses the limitations of the conventional parameter estimation methods. Then, the Bayesian approach with spatial priors is developed and evaluated both in simulated and patient data.
- **Chapter 7:** applies the methods developed in Chapters 4-6 prospectively to an initial patient cohort and reports the diagnostic accuracy in comparison to the invasive measurements.
- **Chapter 8:** summarises the contributions made in this thesis and considers both the future work required and the potential clinical impact of that work.

Chapter 2

Background

2.1 Cardiac anatomy and function

The heart is the centre of the cardiovascular system. It acts as a pump in order to distribute oxygen and nutrients to the tissue around the body and to subsequently remove waste products [7]. This function is essential for sustaining activity in the tissue and to avoid tissue necrosis. The heart is responsible for the circulation of both oxygenated and deoxygenated blood and does so using a series of chambers and vessels, as shown in Figure 2.1. In order to deal with both the distribution of oxygenated blood and the reception of deoxygenated blood, the heart is divided into two systems: the pulmonary circulatory system and the systemic circulatory system. The pulmonary circulation starts at the right atrium from which the right ventricle is filled with deoxygenated blood. The right ventricle then pumps this blood to the lungs through the pulmonary arteries. The blood is oxygenated in the lungs and returns to the heart, specifically the left atrium, through the pulmonary veins. In the systemic circulation, the left ventricle is filled from the left atrium and the blood is pumped, through the aorta, around the body. Deoxygenated blood returns to the heart through the superior and inferior venae cavae to complete the cycle.

The heart muscle, as shown in Figure 2.2, is made up of three layers: a thick middle layer known as the myocardium, the inner endocardium, and the outer epicardium (also known as the visceral pericardium). As with all other tissue, cardiac muscle requires oxygen and nutrients in order to sustain viability and keep pumping blood. The cardiac tissue does not receive oxygen and nutrients by simply holding oxygenated blood. Thus, the requisite oxygen and nutrients need to be delivered to the muscle and this is done through the coronary circulatory system.

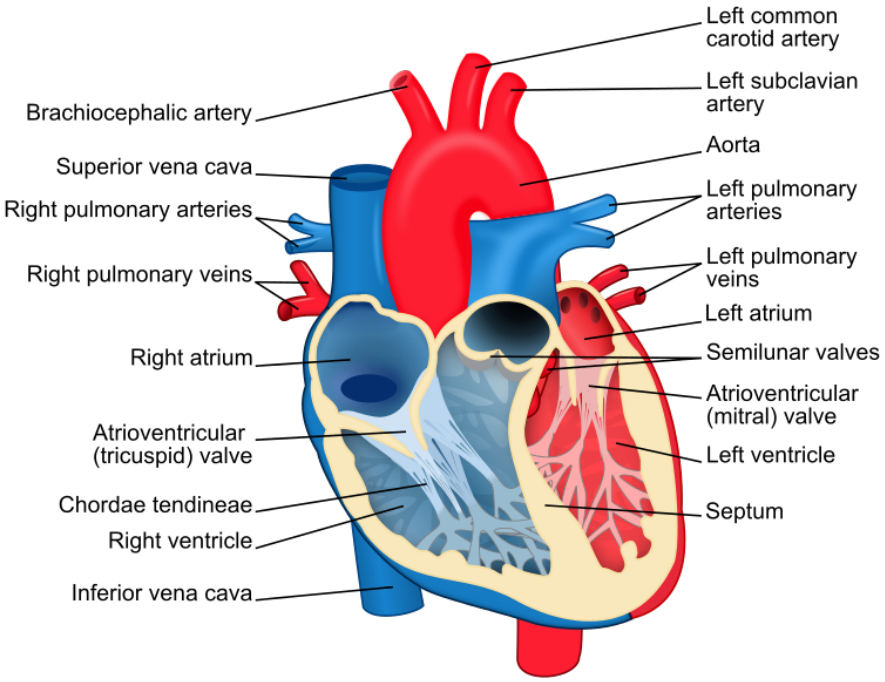

Fig. 2.1 The anatomy of the heart with the chambers, major vessels and valves labelled. The colour blue indicates the structure is a constituent part of the pulmonary circulatory system and similarly red identifies the systemic circulatory system, taken from [8].

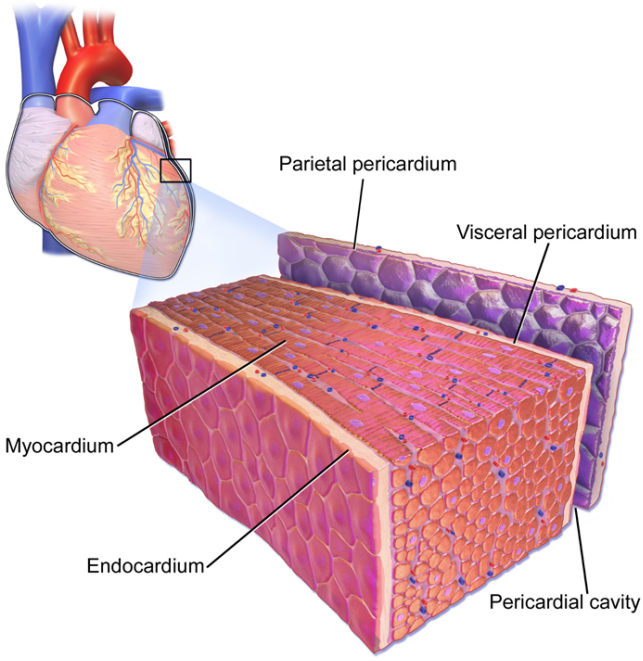

Fig. 2.2 The underlying structure of the cardiac muscle, adapted from [9].

2.2 The coronary circulatory system

The passage of blood between the chambers of the heart is controlled by four valves, shown in Figure 2.1, which separate the atria from the ventricles and the ventricles from a blood vessel. The valves are made of leaflets (flaps) which are opened and closed by changing flow and pressure. The left ventricle is separated from the aorta by the aortic valve. On the leaflets of the aortic valve lies the coronary ostium, the openings of the left and right coronary arteries. The left coronary artery (LCA) branches into the left anterior descending (LAD) and left circumflex (LCx) branches. The right coronary artery (RCA), the LAD, and LCx further subdivide in order to cover the breadth of the epicardium and distribute oxygen and nutrients to the muscle. Though the exact anatomical structure varies from person to person, generally, the RCA supplies the right atrium, right ventricle, and the back of the septum. The front of the septum is supplied by the LAD, as well as the front and bottom of the left ventricle. The left atrium and the back and side of the left ventricle is supplied by the LCx [10].

The coronary circulatory system performs a particularly important role as the myocardium demands 20 times more oxygen than skeletal muscle, at peak heart rate [7]. To satisfy this high demand, even under normal resting conditions the myocardium needs to extract 70-80% of the available oxygen [11]. During exercise, the rate at which the heart beats increases in order to satisfy the increased systemic demand for oxygen and thus the myocardium also demands more oxygen. Since the extraction rate of oxygen from blood is already high, there is limited scope for increased extraction and the increased demand must be met by increasing coronary blood flow [7].

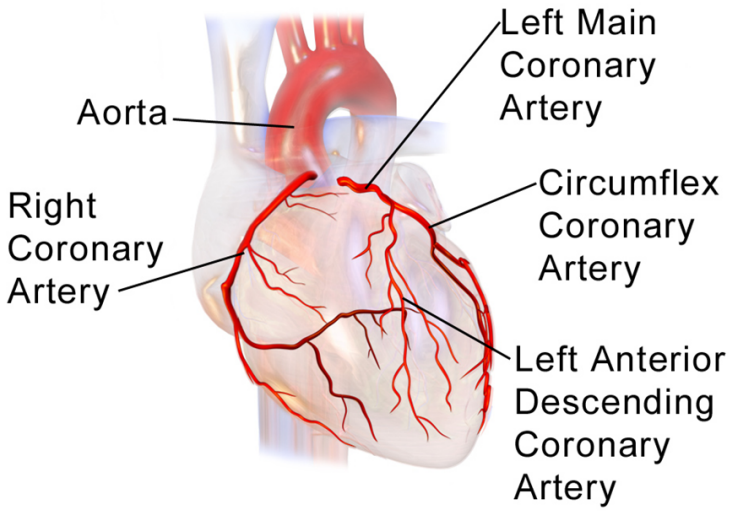

Fig. 2.3 The coronary arteries shown traversing the wall of the heart, adapted from [12].

Coronary blood flow is primarily driven by the pressure gradient between the aorta and the right atrium [10]. Since the coronaries are constricted when the is heart contracted (systole) most flow occurs when the heart is relaxed (diastole). This further inhibits coronary blood flow at higher heart rate. As the heart rate increases, the diastolic proportion of the cardiac cycle falls faster than systole, leading to less unrestricted flow [7]. Blood also flows faster through wider vessels, as there is less resistance. Natural or pharmacologically-induced vasodilation thus increase blood flow [10]. Conversely, the narrowing of the vessels can lead to reduced flow. The coronary arteries can be narrowed by atherosclerosis. This is a disease in which there is a build-up of plaque in the walls of the vessels.

The heart has an innate ability to adapt to changing circumstances. In a processes known as autoregulation, blood flow is well regulated in spite of changes in the available pressure gradient [13]. For example, in the case of the narrowing of a vessel, there will be a proportional increase in coronary perfusion in order to maintain roughly constant flow. From a myogenic point of view, the vessel stretching caused by the increased pressure leads to the depolarisation of the cells and subsequent vasoldilation [13]. Metabolic mechanisms of autoregulation are also at play and stem from the coupling between metabolic activity and blood flow. Hypoxia, a oxygen deficiency, is known to cause vasodilation as it leads to the release of adenosine, which relaxes the vessels. Hypoxia is also thought to open adenosine triphosphate-sensitive potassium (K^+) channels and the increase in interstitial K^+ dilates the vessels [14].

2.3 Ischaemic heart disease

Myocardial ischaemia is the process ensuing when coronary blood flow fails to meet the muscles oxygen and nutrient requirements. The tissue becomes hypoxic and if sustained can undergo irreversible cell necrosis, known as a myocardial infarction or more commonly, a heart attack.

As discussed, ischaemia does not occur under ideal, healthy conditions due to the elegant coupling between oxygen requirements and coronary blood flow. However, such ideal conditions are not guaranteed and in particular are precluded by the atherosclerosis of the coronary arteries. The cholesterol-rich plaque, atheroma, builds up naturally over time in the vessels, though it can be significantly accelerated by lifestyle choices. This build-up can lead to a reduction in blood flow known as ischaemic heart disease (IHD) or coronary artery disease (CAD). Cardiovascular disease (CVD), of which CAD is the most prevalent, is the leading cause of death globally. It accounted for an estimated 17.9 million deaths in 2016 and there is expected to be more hospitalisations and deaths as the population ages, particularly in western countries [15].

The increased pressure caused by the lumen narrowing can be well regulated under resting conditions. It could be that even for moderately narrowed vessels, the increased resistance in the vessel can be offset by distal vasodilation [7]. However, for significantly narrowed vessels, coronary blood flow or perfusion (which are used synonymously in this thesis) will be reduced. The problem is exacerbated during stress or exercise as increased flow is required but the distal vasodilation is not sufficient to achieve this. The effect of a single stenosis on the myocardium can be particularly pronounced due to the limited flow between branches of the coronary tree [7]. The result being that most of the tissue downstream of a stenosis will be affected.

Angina (pectoris) is the term used to describe the chest pain associated with myocardial ischaemia and is in nature either stable or unstable. Stable angina is typically absent at rest and increases with increasing stress or physical exertion. Unstable angina is less predictable. It can be caused by the built-up plaque rupturing and forming blood clots which cut off flow [16]. This may be unrelated to physical exertion and there may have been no prior warning.

The damage associated with myocardial ischaemia can be reversed if the oxygen deprivation is transient. However, if sustained for a period of time, the ischaemia will lead to a myocardial infarction. The oxygen deprivation does not instantaneously lead to cell necrosis, rather it triggers a series of predictable events, commonly referred to as the ischaemic cascade. The series of events, shown in Figure 2.4, begins with reduced perfusion which will in turn lead to impaired diastolic function, (subsequently) impaired systolic function, and culminate in angina and myocardial infarction.

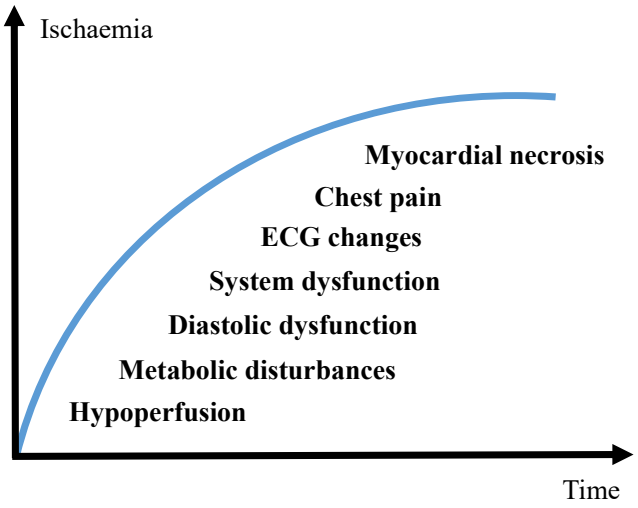

Fig. 2.4 A schematic representation of the ischaemic cascade

The ischaemic cascade is central to any discussion on the diagnosis of CAD as earlier diagnosis (and treatment) is known to improve outcomes [17]. While traditional clinical assessment is concerned with angina and ECG changes, as will be discussed in this thesis,

state-of-the-art imaging techniques are focussed on identifying earlier and earlier markers of CAD.

Myocardial infarctions are classified based on their effect on the electrocardiogram (ECG) of the patient. An elevation of the ST segment of the ECG can be caused by a thrombus, a completely blocked lumen leading to transmural ischaemia and a so-called ST-elevation myocardial infarction (STEMI) [18]. Non-transmural ischaemia can lead to a non ST-elevation myocardial infarction (NSTEMI), this is typically less dangerous as it affects less of the myocardium.

The result of an infarction is that the tissue forms a fibrotic scar [19]. This non-viable tissue has a reduced ability to conduct electrical activity and results in the ventricles being unable to contract properly. The impaired ventricular function causes a reduction in cardiac output and can progressively lead to heart failure [16].

2.4 Imaging coronary artery disease

Imaging for the diagnosis of CAD follows two main directions: anatomical imaging and functional imaging. Anatomical imaging is focused on the visualisation of the coronary arteries and the narrowing thereof. Functional imaging assess the functional significance of the narrowing arterial lumen. Functional tests are usually performed during stress in order to induce perfusion or wall motion abnormalities. The ideal test would, as well as being both sensitive and specific, be safe. With this in mind, non-invasive imaging is preferable as it reduces the risk of adverse advents as a result of the testing and the test ideally would limit the patient's exposure to ionising radiation. In order to maximise the sensitivity of the test it would be desirable for the test to probe effects that are observable at early stages of the ischaemic cascade. In particular, with regards to the functional testing, the ability to detect subtle effects at earlier stages of disease is advantageous and requires either high spatial or temporal resolution.

The history of CAD imaging began with the use of anatomical imaging and then progressed towards the use of functional imaging to diagnose CAD earlier. However, there has been a recent move back towards anatomical imaging, especially in order to rule out CAD. This is based on the argument that even after an abnormal functional test, some form of anatomical imaging is required to confirm the diagnosis of CAD. However, as discussed, this does not provide information on the haemodynamical consequences of the disease and indeed the future probably lies in a combined functional and anatomical assessment.

The following subsections will detail the available forms of CAD testing and include a brief discussion of their respective pros and cons.

2.4.1 X-ray coronary angiography

The coronary angiography is considered to be the gold standard for the diagnosis of CAD [20]. Catheters are inserted into the patients arteries through either the radial or femoral artery and guided to the ascending aorta. An iodine-based radio-opaque contrast agent is then injected in order to visualise the blood vessels and potential narrowings on the X-ray images. While the test is highly diagnostic, the major downsides of the procedure are the risk of complications, including puncturing a vessel, the use of ionising radiation, and the discomfort caused to the patient.

There are further benefits to the approach. It is possible to derive quantitative measures such as the fractional flow reserve (FFR). For this, a pressure sensor is used on the tip of the wire inserted and the FFR value is computed as the ratio of the pressures measured in the aorta and immediately downstream of a lesion. Furthermore, upon the identification of a haemodynamically significant lesion, it is possible to treat it with a stent or a balloon in a procedure known as percutaneous coronary intervention (PCI).

2.4.2 Electrocardiogram

The ECG monitors the electrical activity in and around the heart. As previously discussed, myocardial infarctions can alter the way that the heart conducts electrical activity and this can be observed on an ECG. Since the test is cheap and safe, it is often one of the first assessments that a patient receives [21]. The limitation of the ECG is that the changes in electrical activity only occur at an advanced stage of the ischaemic cascade, though ischaemia can be detected earlier under exercise stress.

2.4.3 Echocardiogram

The echocardiogram (echo) is a cardiac ultrasound and uses a transducer to send and receive ultrasound beams to allow the visualisation of cardiac anatomy. It provides a quick and easy assessment of cardiac structures, wall motion, and, using Doppler-based imaging, even blood flow [22]. An echo is cheap, free from ionsing radiation, and the devices can be brought to a patients bedside. As a result, it is the most commonly performed imaging assessment of the heart [21]. The main limitations to the general applicability of echocardiography in clinical practice are that the image quality depends on the anatomy and acoustic window of the patient, the positioning of the transducers, and the skill of the operator. The images can suffer from a significant amount of speckle noise and may, thus, not be of diagnostic quality. Furthermore,

the wall motion abnormalities probed by the test also only manifest themselves at a late stage of the ischaemic cascade.

2.4.4 Single-photon emission computed tomography

SPECT is one of the most commonly used cardiac imaging techniques. It is a particularly important imaging modality to consider as it can assess myocardial blood flow [23]. This is crucial for the early diagnosis, and to guide the management, of patients with CAD as impaired perfusion occurs early in the ischaemic cascade. SPECT counts the number of photons emitted in an area (and thus the amount of radioisotope accumulated), this is assumed to be proportional to blood flow in the tissue. The imaging is typically carried out with the use of vasodilator stressor agents in order to identify stress-inducible ischaemia.

The major limitation of the modality is that the spatial resolution achievable is typically on the order of 10mm^3. This makes it difficult to identify regional perfusion abnormalities and the images are subject to motion and partial volume effects. Additionally, long imaging times required to record sufficient signal and the photon emitting radioisotopes injected typically have long half-lives meaning significant exposure to ionising radiation for the patient [23].

2.4.5 Positron emission tomography

PET is, in principle, similar to SPECT except that the radiotracers are labelled with positron emitting isotopes. The signal recorded, by an array of detectors around the body, is from the gamma rays emitted when the positrons collide with the electrons in the tissue [21]. Metabolism can be quantified in absolute terms and it is also possible to derive quantitative values of myocardial blood flow (MBF) in units of millilitres per minute per gram of tissue (ml/min/g) [24]. The quantitative values easily identify areas of ischaemia while the patient is stressed. The array of detectors yield superior spatial resolution to SPECT and furthermore, the short half-lives of the radiotracers used, as compared to SPECT, means less exposure to ionising radiation for the patient. However, the amount of radiation and spatial resolution are still limiting.

2.4.6 Computed tomography

Computed tomography (CT) has developed into an emerging technology in the application of non-invasive CAD diagnosis. In particular, coronary CT angiography (CCTA) facilitates the visualisation of the coronary arteries and the National Institute for Health and Care Excellences (NICE) guidelines also include fractional flow reserve derived from CCTA (FFRct). FFRct can

determine the functional significance of a lesion [25]. Recent improvements in CT detector rows have made it possible to test for ischaemia using dynamic stress perfusion CT [26]. However, this is yet to see widespread adoption due to concerns about the radiation dose, technical difficulties leading to motion artefacts, a low contrast-to-noise ratio, quantification challenges, and a lack of availability [27].

2.4.7 Cardiovascular magnetic resonance

Magnetic resonance imaging (MRI) is a hugely versatile imaging modality and CMR has the potential to overcome many of the limitations of the imaging modalities discussed so far. In particular, myocardial perfusion MRI, the subject of this thesis, has emerged as a sensitive and specific ischaemia test. The benefits of myocardial perfusion MRI over the other ischaemia tests discussed are that it is free from ionising radiation and gives high spatial resolution. Perfusion is typically assessed with dynamic contrast-enhanced imaging, using a Gadolinium-based contrast agent.

The MR-IMPACT II trial showed perfusion MRI to have a similar diagnostic accuracy to SPECT in a multi-centre setting [3] and similarly the CE-MARC trial found multi-parametric CMR to be more accurate than SPECT for the diagnosis of coronary artery disease [2]. While the CE-MARC 2 trial showed CMR imaging is associated with a lower probability of unnecessary coronary angiography than SPECT imaging without an increase in major adverse cardiac events (MACE) [28]. It further found that functional testing outperformed anatomical tests with respect to the endpoint of unnecessary angiography. Recently, the MR-INFORM (MR perfusion imaging to guide management of patients with stable coronary disease) study randomised 918 patients with typical angina to either FFR-guided management or perfusion CMR-guided management [4]. It found perfusion CMR to be non-inferior to FFR for the management of patients with respect to major adverse cardiac events. Additionally, it found that a perfusion MRI-guided approach significantly reduced the number of unnecessary coronary revascularisations. Further adding to the evidence supporting the use of perfusion CMR, the SPINS (stress CMR perfusion imaging in the United States) study retrospectively analysed data from the Society for Cardiovascular Magnetic Resonance (SCMR) registry. In this cohort of nearly 2500 patients across 13 centres, the SPINS study showed the long-term prognostic performance of perfusion MRI in a real-world setting [29]. It also showed the costs benefits of CMR as a gate-keeper test: very low downstream costs for ischaemia testing were reported for patients after negative CMR tests.

Further to the evidence presented, the unique selling point of perfusion CMR may be that it can be incorporated easily into a comprehensive CMR examination. The modality's wide-ranging utility has led to it being described a "one-stop shop" for the assessment of

ischaemic heart disease [30]. In a single examination, it is possible to image ventricular function, myocardial ischaemia using stress perfusion imaging and myocardial viability using late gadolinium enhancement. In the coming years, further technical development will also see CMR be used more frequently for the visualisation of the coronary arteries [31].

Despite all the apparent benefits of stress perfusion CMR, it is still not common place in clinical practice. Thus far, all evidence has been accumulated at expert tertiary centres where there is a vast experience of performing and reporting the scans. One of the reasons limiting the widespread clinical adoption is that there is limited data supporting its use at less specialised centres. The reading of the scans is complex and time consuming, and there is little access to training. A recent study by Villa et al. [5] showed the diagnostic accuracy is highly dependent on the level of training of the reader.

This serves to highlight the need for an objective, user-independent assessment of ischaemia and in particular, the quantitative analysis of stress perfusion CMR. Quantitative measures of myocardial perfusion have the potential to add the benefits of speed, automation, and reproducibility to a test which is already known to be accurate, non-invasive, and free from ionising radiation. The quantitative values also add independent prognostic value [32, 33]. However, quantitative perfusion CMR is still hindered by technical difficulties such as respiratory motion, the time-consuming nature of the image processing, and questions about the reliability of the quantitative values. The solutions to these challenges will be discussed in detail in this thesis.

Chapter 3

Myocardial perfusion MR imaging

The chapter will introduce the basic concepts of MRI and how these relate to the imaging of myocardial perfusion. It will then discuss the theory underlying the quantification of myocardial perfusion: the tracer-kinetic modelling, parameter inference, and arterial input function estimation. The chapter concludes with a review of the state-of-the-art in quantitative myocardial perfusion.

3.1 The basics of MRI

MRI is based on the principle of nuclear magnetic resonance (NMR). NMR is the effect exerted on nucleons with non-zero angular spin when exposed to a magnetic field. Atoms with an odd mass number (an atoms mass number is the total number of protons and neutrons in its nucleus) have half-integer spin and this spin is aligned in the presence of an external magnetic field $\mathbf{B_0}$. This yields a net change in magnetic moment $\mathbf{M} = [M_x, M_y, M_z]$ described by:

$$\frac{\mathrm{d}\mathbf{M}}{\mathrm{d}t} = \gamma \mathbf{M} \times \mathbf{B_0} \tag{3.1}$$

where γ is the gyromagnetic ratio. $\gamma = 2.675$ rad $\mathrm{T}^{-1}\,\mathrm{s}^{-1}$ for the hydrogen atom (^1H) which is the most frequently used atom in MRI as it is omnipresent in the human body. Typically, we are considering an ensemble of spins rather than a single spin with $\mathbf{M}$ then being the sum of magnetisations. In the absence of external forces this will be zero as the spins are pointing in all different directions.

In a static $\mathbf{B_0}$ field, the magnetisation precesses at a frequency dependent on the magnitude of $\mathbf{B_0}$, known as the Larmour frequency:

$$\omega_0 = \gamma B_0. \tag{3.2}$$

With the introduction of a radiofrequency (RF) excitation pulse $\mathbf{B_1}$, $\mathbf{M}$ can be flipped from its equilibrium state $\mathbf{M_0}$ into the transverse plane. The $\mathbf{B_0}$ field is typically thought of as being aligned with the z axis, the longitudinal component, and thus the transverse plane is the x–y plane. The flip angle is given by $\alpha = \gamma B_1 \Delta t$, with Δt being the duration of the RF pulse. $\mathbf{M}$ will begin to return to its equilibrium state after the RF pulse is finished and the temporal evolution of $\mathbf{M}$ is given by the Bloch equations:

$$\frac{\mathrm{d}M_x}{\mathrm{d}t} = \omega_0 M_y - \frac{M_x}{T_2} \tag{3.3}$$

$$\frac{\mathrm{d}M_y}{\mathrm{d}t} = -\omega_0 M_x - \frac{M_y}{T_2} \tag{3.4}$$

$$\frac{\mathrm{d}M_z}{\mathrm{d}t} = \frac{M_0 - M_z}{T_1}. \tag{3.5}$$

T_1 and T_2 are the longitudinal and transverse relaxation constants, respectively. The transverse magnetisation decays exponentially with time constant T_2^* and simultaneously, the longitudinal magnetisation returns exponentially to its equilibrium state with time constant T_1. T_2^* is a longer decay constant which incorporates the additional transverse decay due to magnetic field inhomogeneities T_2' such that:

$$\frac{1}{T_2^*} = \frac{1}{T_2} + \frac{1}{T_2'}. \tag{3.6}$$

It is the differences between these relaxation constants, due to the local molecular environment of tissue, that gives different contrasts between tissues and allows us to generate images. The specific sequence of RF pulses and gradient pulses played to achieve the required MR signal is known as the pulse sequence.

3.2 Introduction to myocardial perfusion CMR

The most common approach to the assessment of myocardial perfusion using MRI is with dynamic contrast-enhanced (DCE) acquisitions, as was first described more than 30 years ago [34]. This is done with paramagnetic contrast agents, the most common of which are gadolinium-based. Gadolinium is highly paramagnetic due to its 7 unpaired electrons [35] and

thus the hydrogen nuclei close to the gadolinium will have reduced relaxation times. The T_1 relaxation time of the water protons is inversely proportional to the concentration of gadolinium [36]:

$$R_1 = R_{10} + r_1[\mathrm{Gd}] \tag{3.7}$$

where $R_1 = 1/T_1$ is the longitudinal relaxation rate, R_{10} is the pre-contrast longitudinal relaxation rate, r_1 is the relaxivity of the contrast agent (4.5 $\mathrm{l\,mmol^{-1}\,s^{-1}}$ for gadovist at 3T [37]), and $[\mathrm{Gd}]$ is the concentration of gadolinium. Thus, areas with a high concentration of gadolinium will appear to be brighter on T1 weighted images. In perfusion CMR, a bolus of contrast agent is administered intravenously and time dynamic images are acquired to observe the temporal evolution of the contrast bolus. Areas of the myocardium with reduced perfusion hence appear hypointense. These perfusion defects correspond to regions of either ischaemia or fibrosis [38].

As discussed in Section 2.2, the principle of autoregulation ensures that for even a relatively large coronary artery stenosis there may be no reduction in myocardial blood flow. For this reason, scans are usually acquired at peak, pharmacologically induced, vasodilation such that autoregulation can no longer account for the stenosis. Since exercise is not feasible in the scanner, vasodilator stress is pharmacologically induced. This is typically done with adenosine which causes flow-mediated vasodilation [39]. Rest images may also be acquired to check for scar or to account for artefacts.

To ensure coverage of the LV, 3 slices are typically acquired in a short-axis view using the 'three-of-five' rule [40] where 5 slices are planned with equal slice gap from the base of the LV to the apex and the middle 3 slices are used, demonstrated in Figure 3.1.

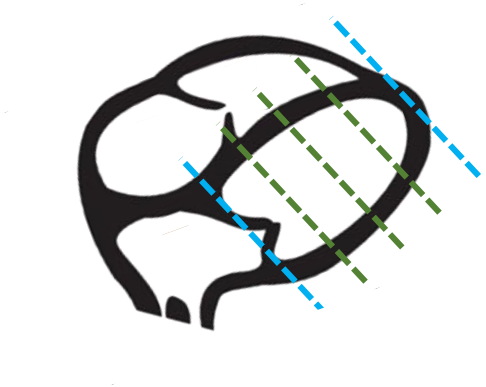

Fig. 3.1 Initially five slices with equidistant gaps are planned and the middle three slices (shown in green) are used.

The most commonly used pulse sequence for perfusion CMR is a 2D multi-slice saturation recovery (SR) sequence [38]. A 90° saturation preparation pulse is used to null the pre-contrast signal and to hence visualise the passage of the contrast bolus. Inversion recovery (IR) rather than SR sequences have also been proposed. In this case the 180° preparation pulse inverts the magnetisation to maximise the dynamic contrast-enhancement. The limitations of IR sequences are the increased imaging time makes it incompatible with high heart rates. IR sequences also makes the contrast dependent on the duration of the R-R interval, which is undesirable in patients with varying heart rates, such as in cases of arrhythmia [41]. The acquisition is ECG-gated, images are acquired a fixed time (trigger time) after the R wave is recorded to the effect that the slices are always acquired in the same cardiac phase [38].

At 3T, the most commonly used readout are spoiled gradient echo readouts. These repeatedly excite the imaging slice with pulses of low flip angle while acquiring k-space data line-by-line. The excitation pulses are with low flip angles to allow rapid imaging, larger flip angles would give more T_1 contrast but would not be possible within a single R-R interval. Balanced steady-state free precession (bSSFP) and echo planar imaging (EPI) readouts are also used but are less commmonly employed.

More recently, 3D [42] and simultaneous multi-slice acquisitions [43] have been proposed in order to increase the coverage of the LV but these are not widely available and have not yet achieved clinical adoption.

Non-contrast alternatives for myocardial perfusion imaging include arterial spin labelled (ASL) and blood oxygen level-dependent (BOLD) CMR. ASL employs RF pulses to locally alter the magnetisation of the arterial blood supply and then images the labelled blood as it reaches the myocardium in order to estimate perfusion [44]. BOLD uses deoxyhaemoglobin as an endogenous contrast agent. Since deoxyhaemoglobin is paramagnetic, it reduces the signal in T_2-weighted images and thus gives a direct assessment of myocardial oxygenation and blood flow [45]. Both approaches have some limited clinical data supporting their use but they still remain research tools. As such, this thesis will focus solely on DCE perfusion CMR.

As discussed, due to its high diagnostic accuracy, stress perfusion CMR has become one of the methods of choice for the diagnosis of CAD. It has a class IA recommendation from the European Society of Cardiology (ESC) for the evaluation of patients with an intermediate pretest probability of CAD [46]. The main limitation of the modality is the difficulty of interpreting the images. The diagnostic accuracy has been shown to be highly dependent on the level of experience of the operator [5]. The difficulty of the interpretation of the images is visualised in Figure 3.2 which shows the same image with different levels of contrast windowing. The identification of perfusion defects, as indicated by the arrows, changes with

different windowing. A potential solution to this is the quantitative analysis of the images which would add user-independence and reproducibility to the high clinical utility of the modality.

Fig. 3.2 An example image demonstrating the difficulty of the visual assessment of perfusion CMR. The diagnosis of the patient from one-vessel disease (orange arrows) changes to two-vessel disease (orange and yellow arrows) with the narrowing of the contrast window. At an intermediate level of windowing (centre), the diagnosis is not clear.

3.3 Quantitative myocardial perfusion CMR

The goal of quantitative myocardial perfusion CMR is to infer the kinetics of the myocardium from the observed signal (contrast) evolution. The quantification of these tissue properties give a high level of diagnostic information about the patient.

3.3.1 Signal intensity to contrast concentration conversion

The first challenge in this process is the conversion of the MR signal intensities (SI) to the concentration of the contrast agent, gadolinium [Gd] (in units of M). In the ideal case, there is a linear relationship between SI and [Gd]. As will be shown in Section 3.3.2, the tracer-kinetics are modelled as a linear time-invariant system so that, in the case of linear relationship, the parameter estimates derived with the SI curves directly are equal to those derived with the concentration curves. The reality, however, is that there is a more complex, non-linear relationship between SI and [Gd] [47] causing a signal saturation for high [Gd] [48]. As a result, the relationship between SI and [Gd] needs to be modelled. This is done by estimating T_1 at each time from the corresponding SI and relating T_1 to [Gd] through equation 3.7. The signal equation, as a function of T_1, for a saturation-recovery spoiled gradient echo sequence,

as commonly used in perfusion CMR, is given as:

$$S = \psi S_0 \left[(1 - \exp(-T_{SAT}/T_1)) a^{n-1} + (1 - \exp(-T_R/T_1)) \frac{1 - a^{n-1}}{1 - a} \right] \tag{3.8}$$

where ψ is a constant scaling factor that absorbs factors such as the coil sensitivities and system gains, S_0 is the baseline signal level, T_{SAT} is the time between the saturation preparation pulse and the acquisition of the central line of k-space, T_R is the repetition time between excitation pulse, $a = \cos\alpha \exp(-T_R/T_1)$, α is the flip angle and n is the number of excitation pulse from the beginning until the centre of k-space [47]. ψ is assumed to be constant over time and can be estimated from the baseline pre-contrast images using a baseline T_{10}. Since $S = \psi f(T_1)$, the estimated ψ is given as $\psi = f(T_{10})/S_0$. The baseline T_{10} can either be taken from literature values or from a pre-contrast T_1 map. The T_1 value at each time point is then determined using a root-finding algorithm.

3.3.2 Tracer-kinetic modelling

In theory, the gadolinium-based contrast agents used in perfusion CMR are indicators rather than tracers as they are not chemically the same as the systemic substance of interest [49]. Nonetheless, the word tracer will be used in order to maintain consistency with the literature.

General theory

A tissue is modelled as system with a series of inlets and outlets through which the system substance can flow. The models are built on the theory of linear time-invariant systems [50]. That is, that the transit time, the time elapsed between entering and leaving the system, does not depend on the time of the contrast injection or the injected concentration. The system is governed by the conservation of mass. This states that no tracer is created or destroyed in the system and gives that the rate of change of concentration in the tissue is the difference between the influx and outflux through the inlets and outlets of the system [50]:

$$v\frac{dC(t)}{dt} = \sum_i F_i C_i(t) - \sum_o F_o C_o(t) \tag{3.9}$$

where v is volume of distribution (the volume of the system that contains the tracer), $C(t)$ is the total concentration of tracer in the system and, F_i, F_o and $C_i(t), C_o(t)$ are the flows through and concentrations at the inlets i and outlets o of the system. The system itself can be made up of a number of interacting compartments with the inlets of a compartment possibly being the

outlets of another compartment. Equation 3.9 can be applied to each compartment to yield a system of n ordinary differential equations (ODEs).

Two-compartment exchange model

In the myocardium, there is a single arterial input and single outlet. The tracer is assumed to be contained in the blood plasma and the extravascular extracellular space (EES) and that each of these spaces are an individual compartment. This gives rise to, under some further assumptions, to the two-compartment exchange model (2CXM) [51]. The further assumptions made are that the influx and outflux of the system is through the plasma compartment, the EES compartment only exchanges with the plasma compartment, and that this exchange is equal in both directions. This then gives two coupled ODEs for the concentration of contrast in the

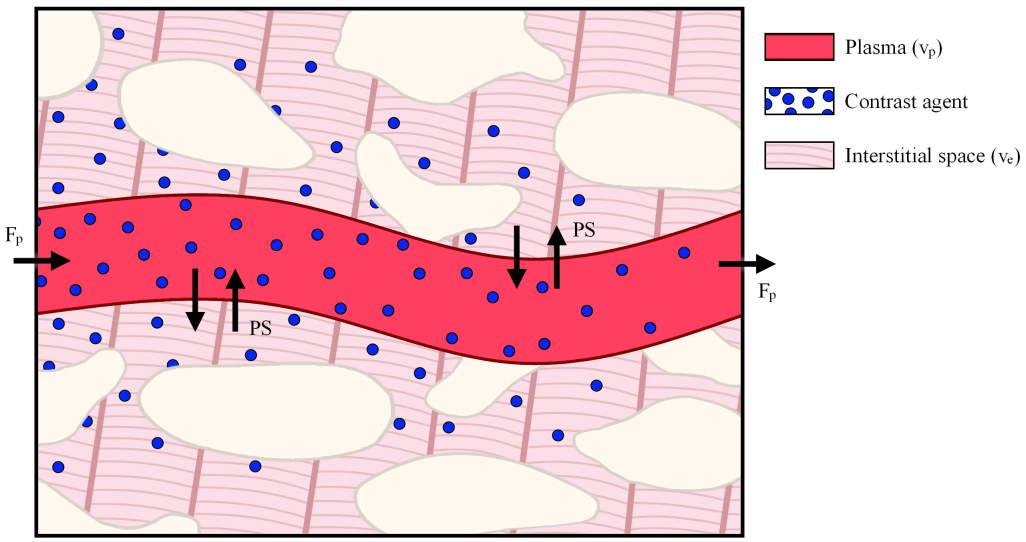

Fig. 3.3 A visualisation of the underlying physiological representation of the 2CXM.

plasma C_p (M) and EES C_e (M) compartments [50]:

$$v_p \frac{dC_p(t)}{dt} = F_p \cdot (C_{AIF}(t) - C_p(t)) + PS \cdot (C_e(t) - C_p(t)) \tag{3.10}$$

$$v_e \frac{dC_e(t)}{dt} = PS \cdot (C_p(t) - C_e(t)). \tag{3.11}$$

In these equations, $C_{AIF}(t)$ (M) is the arterial input function (AIF), the assumed input to the system that is being modelled. F_p is the plasma flow (ml/ min /ml) , v_p is the fractional plasma volume (dimensionless), v_e is the fractional interstitial volume (dimensionless) and PS is the

permeability-surface area product (ml/ min /ml). The total concentration of contrast in the myocardial tissue is then given as the weighted sum of the concentration in the compartments:

$$C_{myo}(t) = v_p C_p(t) + v_e C_e(t). \tag{3.12}$$

The 2CXM can be modified by making additional assumptions that the system contains only one compartment or that there is uptake of contrast rather than exchange of contrast in the tissue [50]. It can further be extended to include a spatial component, i.e to assume that the concentration of contrast is not uniformly distributed over a compartment.

In this thesis, the 2CXM will be the focus as it balances most closely matching the underlying physiology while still having an analytic solution.

Solution of the two-compartment exchange model

An analytic solution for $C_{myo}(t)$ can be obtained using the Laplace transform under the assumption of zero initial concentration $C_p(t=0) = 0$ and $C_e(t=0) = 0$. In the Laplace domain, the coupled ODEs in equations 3.10 and 3.11 become:

$$v_p \tilde{C}_p(s) = F_p \cdot (\tilde{C}_{AIF}(s) - \tilde{C}_p(s)) + PS \cdot (\tilde{C}_e(s) - \tilde{C}_p(s)) \tag{3.13}$$

$$v_e \tilde{C}_e(s) = PS \cdot (\tilde{C}_p(s) - \tilde{C}_e(s)) \tag{3.14}$$

where $\tilde{C}(s)$ is the Laplace transform of $C(t)$. Isolating $\tilde{C}_e$ from equation 3.14 yields:

$$\tilde{C}_e(s) = \frac{PS}{v_e s + PS} \tilde{C}_p(s) \tag{3.15}$$

which can be substituted back into equation 3.13 to give:

$$(v_p s + F_p + PS)\tilde{C}_p(s) = F_p \cdot \tilde{C}_{AIF}(s) + PS \frac{PS}{v_e s + PS} \tilde{C}_p(s) \tag{3.16}$$

and finally:

$$\tilde{C}_p(s) = F_p \cdot \tilde{C}_{AIF}(s) \frac{\frac{1}{v_p}(s + \frac{PS}{v_e})}{s^2 + s(\frac{F_p}{v_p} + \frac{PS}{v_p} + \frac{PS}{v_e}) + \frac{F_p}{v_p}\frac{PS}{v_e}}. \tag{3.17}$$

Similarly,

$$\tilde{C}_e(s) = F_p \cdot \tilde{C}_{AIF}(s) \frac{\frac{PS}{v_p v_e}}{s^2 + s(\frac{F_p}{v_p} + \frac{PS}{v_p} + \frac{PS}{v_e}) + \frac{F_p}{v_p}\frac{PS}{v_e}}. \tag{3.18}$$

Hence, the total tissue concentration in the myocardium can be written in Laplace space as:

$$\tilde{C}_{myo}(s) = v_p \tilde{C}_p(s) + v_e \tilde{C}_e(s) \tag{3.19}$$

$$= F_p \cdot \tilde{C}_{AIF}(s) \frac{s + \frac{PS}{v_p} + \frac{PS}{v_e}}{s^2 + s(\frac{F_p}{v_p} + \frac{PS}{v_p} + \frac{PS}{v_e}) + \frac{F_p}{v_p}\frac{PS}{v_e}}. \tag{3.20}$$

It is observed that the denominator of equation 3.20 is a quadratic function of s and that its roots are given by:

$$\begin{pmatrix} \alpha \\ \beta \end{pmatrix} = \left[-\frac{1}{2}\left(\frac{F_p}{v_p} + \frac{PS}{v_p} + \frac{PS}{v_e}\right) \pm \sqrt{\left(\frac{F_p}{v_p} + \frac{PS}{v_p} + \frac{PS}{v_e}\right)^2 - 4\frac{PS}{v_e}\frac{F_p}{v_p}} \right] \tag{3.21}$$

and so by the use of partial fractions equation 3.20 can be rewritten as:

$$\tilde{C}_{myo}(s) = F_p \cdot \tilde{C}_{AIF}(s)\left(\frac{A}{s-\alpha} + \frac{1-A}{s-\beta}\right) \tag{3.22}$$

with $A = \frac{\alpha + \frac{PS}{v_p} + \frac{PS}{v_e}}{\alpha - \beta}$. The inverse Laplace transform then yields the time domain solution:

$$C_{myo}(t) = F_p \cdot R(t) * C_{AIF}(t) \tag{3.23}$$

with:

$$R(t) = A\exp(\alpha t) + (1-A)\exp(\beta t) \tag{3.24}$$

being the residue function which can also be written as $R(t;\theta)$ to emphasise its dependence on the kinetic parameters $\theta = (F_p, v_p, v_e, PS)$. The solution given by Equation 3.23 is shown in terms of the concentration curves in Figure 3.4.

The model, as derived, considers the plasma compartment and hence the plasma flow and plasma volume parameters. Since the convention is to report blood flow and blood volume parameters a conversion can be made using the blood haematocrit value $F_b = F_p/(1-\text{Hct})$ and $v_b = v_p/(1-\text{Hct})$. The AIF, which is sampled from the LV cavity, is converted from arterial blood concentration to arterial plasma concentration by substituting $C_{AIF}(t)/(1-\text{Hct})$ for

$C_{AIF}(t)$. Patient specific haematocrit values could be used but they are not typically available and a literature reference of Hct $= 0.45$ is used [37]. Flow values are converted from units of ml/ min /ml to its mass equivalent ml/ min /g by multiplying by the specific density of the myocardium, taken as 1.05 g ml^{-1}. Note that F_b is often referred to as myocardial blood flow and will be used interchangeably with the acronym MBF.

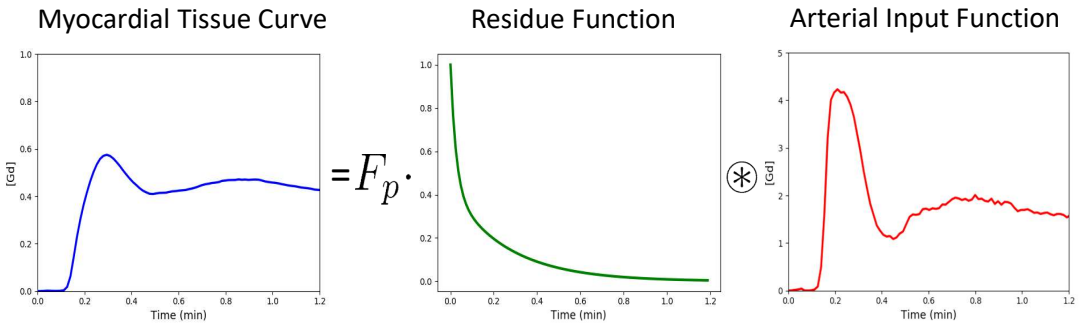

Fig. 3.4 The myocardial tissue curves is shown as the result of a convolution of the AIF with a residue curve.

Kinetic parameter estimation

The most common approach to the estimation of the model parameters from observed myocardial and arterial concentration curves is using non-linear least squares fitting [52] with the most popular choice of fitting algorithm being the Levenberg–Marquardt approach [53]. That is to say, the sum of squared errors between the analytic solution for C_{myo} and the observed myocardial tissue concentration curves is minimised with respect to θ. The parameters $\hat{\theta}$ giving the optimal sum of squared errors are taken as an estimate of the true parameters, this is:

$$\hat{\theta} = \arg\min_{\theta} \|C_{myo}(t) - F_p \cdot R(t;\theta) * C_{AIF}(t)\|_2^2. \tag{3.25}$$

This process is sometimes (incorrectly) referred to as a deconvolution.

The ability to accurately estimate θ can depend on the quality of the data. The data quality can be limited by the signal-to-noise ratio (SNR), the acquisition time, the temporal resolution, and artefacts, such as motion [52]. These introduce local optima in the cost function. This means that there are distinct sets of parameters that are indistinguishable at the noise level present in the data [6]. The result of this is that the parameter estimates obtained from the non-linear least squares fitting algorithm are highly dependent on the initial starting point of the optimisation. Ahearn et al. [52] reported that repeating the optimisation with multiple different starting points can improve the reliability but still is far from perfect even using simulated data

without noise. Buckley [6] found an array of local minima in which different combinations of parameters give very similar solutions, while Jerosch-Herold et al. [54] were unable to get unique estimate for F_p.

The reliability of the estimated parameters can also be improved by reducing the complexity of the model used [6]. As mentioned, other choices of model are possible. Examples of models commonly employed for myocardial perfusion quantification are the Kety-Tofts model [55] and the Fermi model [54]. These models have fewer parameters to estimate, making the fitting problem more stable. However, they have limitations in that the Kety-Tofts model does not resolve directly for F_p and the Fermi model is not physiologically motivated. Alternatively, approaches for improving the parameter estimates with the 2CXM include fitting to a concentration curve averaged over a whole segment of myocardium. This sacrifices resolution in order to increase contrast-to-noise (CNR). However, it is well known that high resolution maps are needed for detecting subtle ischaemia [56].

This motivates the need for more robust fitting approaches, as will be discussed in Chapter 6.

Arterial input function

The accurate estimation of the AIF is one of the key challenges of myocardial perfusion quantification. In theory, the AIF should be sampled from the inlet of the system. In the case of myocardial perfusion CMR this would be the root of the aorta. However, this is not typically imaged in a standard perfusion CMR acquisition and those the AIF is sampled from the LV. An example image with the sampling locations of is shown in Figure 3.5. The effect of sampling in the aorta rather than the LV would be a delay and dispersion in the AIF [57]. The delay can be accounted for by replacing $C_{AIF}(t)$ with $C_{AIF}(t-\tau)$ where τ is the delay and can either be fit as an extra model parameter or estimated separately. The dispersion could also be modelled and accounted for [57], though this is not done in perfusion CMR and leads to a systematic under-estimation of perfusion.

Since the whole bolus of contrast passes through the LV cavity more-or-less simultaneously, very high concentrations of contrast agent are recorded at the peak of the AIF. As a result, the relationship between the signal intensity and contrast concentration in the AIF is non-linear [58]. Conversely, as only a small fraction of the total amount of the contrast inject perfuses a particular area of myocardium, the concentration remains low and a linear relationship between signal intensity and contrast concentration is assumed to hold.

As discussed, the contrast concentration can be estimated from the AIF SI using Equation 3.8. However, this fitting suffers from the same difficulties that were discussed in Section 3.3.2 and it would beneficial if a linear relationship could be assumed so that the

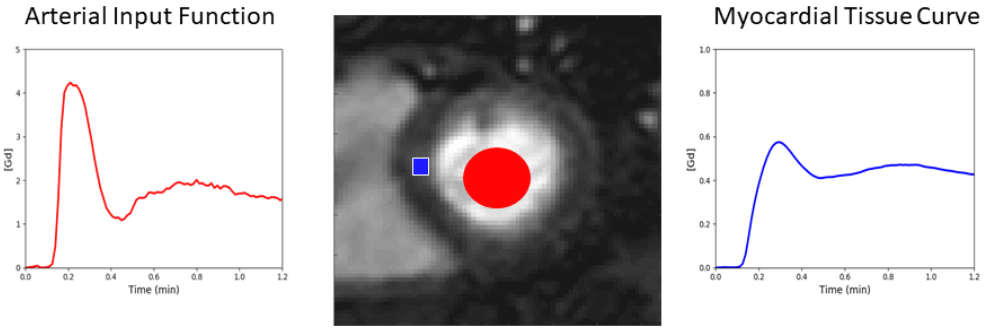

Fig. 3.5 The AIF (red, left) and myocardial tissue curve (blue, right) shown with their corresponding sampling locations overlaid on the MR image (centre).

tracer-kinetic modelling could be performed directly using the relative signal enhancement approximation to the contrast concentration [59]:

$$C(t) \approx \frac{R_{10}}{r_1} \cdot \frac{S(t) - S(0)}{S(0)}. \tag{3.26}$$

For this reason, a significant amount of effort and research in methods for myocardial perfusion quantification is focused on approaches for approximating a linear relationship between signal intensity and contrast concentration in the LV cavity. There are currently two approaches for doing this: the dual-bolus approach and the dual-sequence approach.

The dual-bolus approach uses a low-dose bolus (the pre-bolus) of contrast agent (typically $1/10^{\text{th}}$ of the full dose) in attempt to avoid the signal saturation at high contrast concentrations [48]. This low dose, for AIF estimation, does not yield enough signal to assess the myocardium so it is then followed by a full dose (the main bolus). For the tracer-kinetic modelling, the AIF from the pre-bolus is scaled up (by 10) to approximate the main bolus without signal saturation and used with the myocardial curves from the main bolus. The dual-bolus method is well validated and has proven to give accurate estimates of perfusion [60–62]. However, its clinical adoption has been limited due to the complexity added to the scan and the extra work involved in the two injections.

The dual-sequence method acquires an extra low resolution image slice with a short saturation-recovery time to minimise the saturation of the AIF signal [63]. The benefit of the dual-sequence is that perfusion can be quantified accurately with a single bolus of contrast. The clinical adoption has been slow as the sequence has yet to be commercialised and made available on all scanners. However, recent implementations of research prototypes are making the sequence more widely available [58, 64]. The limitation is that the extra image slice adds additional time to the acquisition, at high heart-rates it, therefore, may not be possible to

acquire all slices in one cardiac phase and the spatial resolution may have to be compromised. Furthermore, while the short saturation time minimises the signal saturation, it may not completely prevent it.

Recent work has demonstrated that since there is an extra image required for the dual-sequence approach that it is feasible to not collocate this with the myocardial slices [65]. Mendes et al. chose to place the AIF slice in the ascending aorta which should be more accurate in theory, though further research is required to fully explore this direction.

3.4 Literature review

There is a wealth of literature on methods, evaluation, and validation of quantitative perfusion CMR. A lot of the early work focused on the use of semi-quantitative metrics where, in lieu of the full tracer-kinetic modelling, the ratio of the up-slope in the myocardial tissue curves to the up-slope in the AIF is used as a surrogate for flow. This has been validated versus coronary angiography [66–68] and FFR [69] with favourable accuracy as compare to visual assessment. It has been further compared to the non-invasive reference standard for perfusion quantification, PET, showing a good correlation between the methods [70, 71]. Al-Saadi et al. [72] used a training set to derive a cutoff for ischaemia and applied the threshold obtained prospectively to a new cohort and found a diagnostic accuracy of 87% for the detection of a significant stenosis on the coronary angiogram.

The limitation of the semi-quantitative measures is that they are not physiological and as such are subject to variations across patients, scanners, and implementations. The wide variations in absolute values motivated the use of the myocardial perfusion reserve (MPR) instead of the absolute values. The MPR is the ratio of flow at stress to flow at rest and the idea is that the variations may cancel themselves out in the ratio. This is not really the case and, indeed, Mordini et al. [73] showed superior diagnostic performance for fully-quantitative perfusion over the semi-quantitative measures. Furthermore, there is a recent trend towards stress only imaging to reduce scan time and thus MPR is no longer possible and absolute quantification of stress perfusion is desired.

Other semi-quantitative measure have also been developed. Hautvast et al. [74] computed gradients in the signal-intensity curves in the transmural direction, across the myocardial wall. This built on the knowledge that perfusion defects appear earlier and more severely in the sub-endocardial wall. Chiribiri et al. [75]. used the temporal dyssynchrony of flow in the myocardium. This is effective at detecting CAD as a coronary artery stenosis causes temporal delays and dyssynchrony in the contrast flow, while contrast flow is temporally uniform in the

absence of a stenosis. While both approaches showed promising performance, neither has seen widespread adoption.

More recently, much of the focus in the field has been towards fully-quantitative perfusion CMR. This has again been compared extensively to PET perfusion estimates [76–78]. All of these studies found a strong linear correlation even if the absolute values do not agree perfectly due to the differences in the quantification methods. Similarly, two studies have found a high correlation between perfusion quantified by CMR and by fluorescent microspheres in dogs [60] and pigs [62]. This indicates that quantitative perfusion CMR is indeed accurately estimating flow and paves the way for its use in the clinic.

There has been further validation versus invasive measurements in patients with CAD. Lockie et al. [79] reported an area under the curve (AUC) of 0.89 on the receiver operating characteristic (ROC) analysis versus FFR. This matched the accuracy of the expert visual assessment. Similar accuracy in comparision to invasive measurements was reported in a series of further studies [59, 80–82]. Out of these, importantly, Papanastasiou et al. [80] reported superior diagnostic accuracy using a full tracer-kinetic model rather than the Fermi function approximation and they also, along with Biglands et al. [81], found no benefit of including the rest results in addition to the stress perfusion values. Sammut et al. [32] took all of this a step further and showed the prognostic value and in particular that the ischaemic burden computed by quantitative perfusion CMR predicts adverse cardiac events.

The focus on quantitative perfusion may seem disproportionate considering that none of the aforementioned studies show that it outperforms the visual assessment. However, it should be noted that all of the studies were conducted at very experienced research hospitals. Villa et al. [5] showed that the performance of the visual assessment drops off quickly for less experienced operators. The hypothesis is that quantitative perfusion is less user-dependent than the visual assessment that it could more easily generalise to less experienced centres.

The drawback of all the studies is that the quantification still involved tedious manual interaction for the selection of the AIF, segmentation of the myocardium, motion correction, and time delay estimation. For example, Biglands et al. [81] reported that it took one hour per patient to manually correct the myocardial segmentation to fit the motion in the data which is not feasible in clinical routine. This motivates the aim of this thesis, to build and validate a fully-automatic pipeline including robust motion compensation and more reliable estimates of the kinetic parameters, negating some of the problems discussed in Section 3.3.2.

There has been other work developed concurrently or after the work presented in this thesis. Xue et al. [83] presented an automated pipeline using their dual sequence implementation [64]. This was compared to PET in a semi-automated approach which automatically generated pixel-wise flow maps but required manual segmentation of myocardium and its sub-segmentation

[84]. Finally, they also demonstrated the prognostic value of quantitative perfusion CMR in a study which included automatic segmentation [33].

Chapter 4

Robust non-rigid motion compensation of free-breathing myocardial perfusion MRI data

4.1 Preface

The reliable quantification of myocardial perfusion on a pixel-wise level assumes that the myocardium remains stationary over time. This is of course not realistic as the heart is contracting and the patient is breathing. Cardiac motion is well accounted for in perfusion CMR as the acquisition are ECG-triggered so that a slice is always imaged in the same cardiac phase. However, respiratory motion can cause inter-frame misalignment. The effect of this inter-frame misalignment on the myocardial tissue curves is shown in Fig 4.1 which can lead to errors in the tracer-kinetic modelling.

The most common way to minimise respiratory motion is breath-holding but since typical scans are longer than a minute, the breath-hold cannot cover the full scan. This is especially true for patients with heart disease who have trouble breathing and breath-holding. Long breath-holds also induce changes in heart rate and, thus, cause images to be acquired at different cardiac phases [85]. For visual assessment, a short breath-hold around the time of the first-pass of the contrast bolus through the myocardium is sufficient. However, this is not the case for tracer-kinetic model fitting, particular for accurately identifying the microvascular kinetics which play out at longer time scales.

Motion compensation techniques are based on using image registration to correct the inter-frame misalignment. Mathematically, this is to define a cost function C describing how dissimilar an image I_i is from a reference image R_i and to find the transformation T_i from the

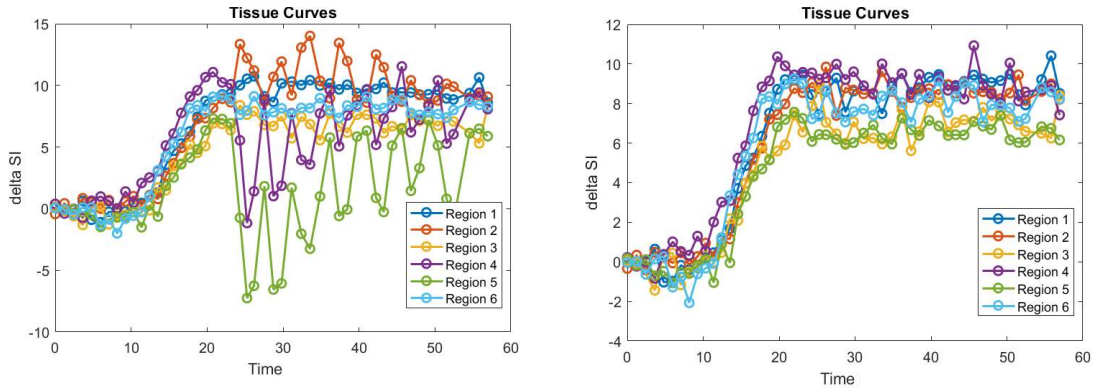

Fig. 4.1 The motion profile of myocardial tissue curves before and after motion compensation taken as the average signal from each of the 6 AHA segments of one myocardial slice.

set of possible transformations Ω that minimises this cost:

$$\hat{T}_i = \underset{T_i \in \Omega}{\arg\min} \left[C\big(T_i(I_i), R_i\big) + \kappa E(T_i) \right] \quad \forall\, i = 1, 2, \ldots, N \tag{4.1}$$

where N is the total number of images and E is a regularisation term, to enforce smooth transformations, controlled by the parameter κ.

The difficulty of applying image registration to perfusion CMR images is the dynamic contrast-enhancement. The typical cost functions cannot disentangle whether the dissimilarity in two images is cause by inter-frame misalignment or just by the contrast agent being in a different location. This work uses robust principal component analysis, which decomposes a corrupt matrix $\mathbf{M}$ into its constituent low-rank $\mathbf{L}$ and sparse $\mathbf{S}$ components such that $\mathbf{M} = \mathbf{L} + \mathbf{S}$, to separate the dynamic contrast-enhancement from the baseline signal. An example RPCA decomposition for a toy example from [86] is shown in Figure 4.2. A more interesting example is seen in Figure 4.3 (from [86]) where RPCA is applied to video surveillance data, it is seen that it well decomposes the video into background (this is low-rank as it remains constant over time) and foreground (this is sparse as it is constantly changing).

It is perhaps somewhat surprising but such a separation can be easily computed [87] and it can be formulated as the solution to:

$$\hat{\mathbf{L}}, \hat{\mathbf{S}} = \underset{\mathbf{L},\mathbf{S}}{\arg\min} \;\; \text{rank}(\mathbf{L}) + \lambda \|\mathbf{S}\|_0 \;\; \text{s.t} \;\; \mathbf{L} + \mathbf{S} = \mathbf{M}. \tag{4.2}$$

Since the l_0 norm, which counts nonzero entries, cannot be easily minimised, it is replaced by

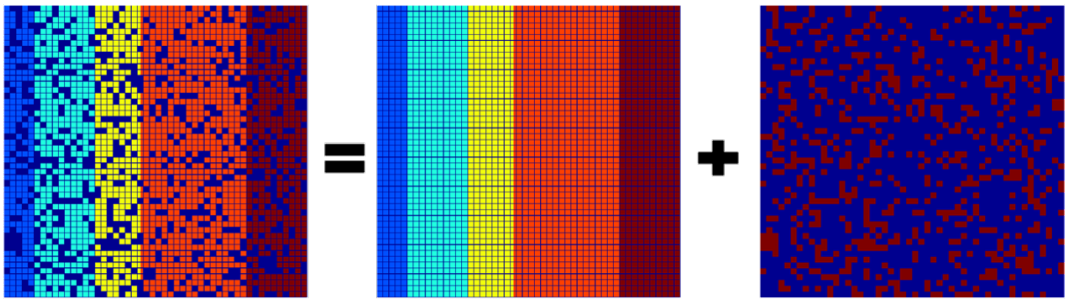

Fig. 4.2 An example of a RPCA decomposition applied to a toy problem, where it is seen to decompose a noise corrupted matrix into its constituent low-rank (structure) and sparse (noise) components [86].

Fig. 4.3 RPCA applied to video surveillance data, where it is seen that the low-rank component well models the background and the sparse component models the foreground [86].

the l_1 norm, which also encourages sparseness [88], leading to:

$$\hat{\mathbf{L}}, \hat{\mathbf{S}} = \underset{\mathbf{L},\mathbf{S}}{\arg\min} \ \|\mathbf{L}\|_* + \lambda \|\mathbf{S}\|_1 \ \text{ s.t } \ \mathbf{L} + \mathbf{S} = \mathbf{M}. \tag{4.3}$$

where $\|\cdot\|_*$ is the sum of the singular values of the matrix and is known as the nuclear norm. The optimisation is solved using augmented Lagrangian multipliers, in an alternating directions manner [89]. That is that we iteratively solve the problem for $\mathbf{L}$ and $\mathbf{S}$ rather than for both simultaneously. This, intuitively, alternates between soft-thresholding the singular values of $\mathbf{L}$ to encourage low-rankness and soft-thresholding the entries of $\mathbf{S}$ to encourage sparseness. With the soft-thresholding operator defined as:

$$\left(\mathscr{S}_\varepsilon[\mathbf{X}]\right)_{ij} := \begin{cases} X_{ij} - \varepsilon & \text{if } \ X_{ij} \geq \varepsilon \\ X_{ij} + \varepsilon & \text{if } \ X_{ij} < \varepsilon \end{cases} \tag{4.4}$$

this yields the alternating direction method of multipliers (ADMM) for RPCA in Algorithm 1.

Algorithm 1: RPCA via ADMM

Input : $\mathbf{M}$, $\lambda > 0$

Initialise : $k = 0$, $\mathbf{S}_0 = \mathbf{Y}_0 = 0$, $\mu > 0$

while *not converged* **do**

$(\mathbf{U}, \Sigma, \mathbf{V}) \leftarrow \text{svd}(\mathbf{M} - \mathbf{S}_k + \mu^{-1}\mathbf{Y}_k)$;

$\mathbf{L}_{k+1} \leftarrow \mathbf{U}\mathscr{S}_{\mu^{-1}}[\Sigma]\mathbf{V}^T$;

$\mathbf{S}_{k+1} \leftarrow \mathscr{S}_{\lambda\cdot\mu^{-1}}[\mathbf{M} - \mathbf{L}_{k+1} + \mu^{-1}\mathbf{Y}_k]$;

$\mathbf{Y}_{k+1} \leftarrow \mathbf{Y}_k + \mu(\mathbf{M} - \mathbf{L}_{k+1} - \mathbf{S}_{k+1})$;

end

Output : $\hat{\mathbf{L}} = \mathbf{L}_k$, $\hat{\mathbf{S}} = \mathbf{S}_k$

where svd is the singular value decomposition.

There has been a wide variety of approaches published in the literature in attempt to solve this problem, as described in part II B of Section 4.2 and in the recent benchmark paper by Pontre et al. [85]. However, none have gained widespread adoption or are used in clinical practice, possibly due to a lack of validation and robustness, motivating the need for our reliable motion compensation scheme.

4.2 Journal article

The following text is reproduced as published [90]:

***Scannell, C.M.**, Villa, A.D.M., Lee, J., Breeuwer, M. & Chiribiri, A. Robust Non-Rigid Motion Compensation of Free-Breathing Myocardial Perfusion MRI Data. IEEE Trans. Med. Imaging 38, 1812–1820 (2019).* :

This is the author's version of an article that has been published in this journal. Changes were made to this version by the publisher prior to publication.
The final version of record is available at http://dx.doi.org/10.1109/TMI.2019.2897044

Robust non-rigid motion compensation of free-breathing myocardial perfusion MRI data

Cian M. Scannell*, *Student Member, IEEE,* Adriana D.M. Villa, Jack Lee, Marcel Breeuwer and Amedeo Chiribiri

***Abstract*— Kinetic parameter values, such as myocardial perfusion, can be quantified from dynamic contrast enhanced (DCE-) magnetic resonance imaging (MRI) data using tracer-kinetic modelling. However, respiratory motion affects the accuracy of this process. Motion compensation of the image series is difficult due to the rapid local signal enhancement caused by the passing of the gadolinium-based contrast agent. This contrast enhancement invalidates the assumptions of the (global) cost functions traditionally used in intensity-based registrations. The algorithms are unable to distinguish whether the differences in signal intensity between frames are caused by spatial motion artefacts or the local contrast enhancement. In order to address this problem, a fully-automated motion compensation scheme is proposed which consists of two stages. The first of which uses robust principal component analysis (RPCA) to separate the local signal enhancement from the baseline signal, before a refinement stage which uses traditional PCA to construct a synthetic reference series that is free from motion but preserves the signal enhancement. Validation is performed on 18 subjects acquired in free-breathing and 5 clinical subjects acquired with a breath-hold. The validation assesses visual quality, temporal smoothness of tissue curves and the clinically relevant quantitative perfusion values. The expert observers score of visual quality increased by a mean of 1.58/5 after motion compensation and improvement over previously published methods. The proposed motion compensation scheme also leads to the improved quantitative performance of motion compensated free-breathing image series (30% reduction in the coefficient of variation across quantitative perfusion maps, 53% reduction in temporal variations (p<0.001)).**

***Index Terms*— Image registration, Myocardial perfusion MRI, Respiratory motion compensation, RPCA, Tracer-kinetic modelling**

I. INTRODUCTION

FIRST-pass myocardial stress perfusion cardiovascular magnetic resonance (CMR) has become one of the tools of choice for the non-invasive diagnosis of myocardial ischaemia [1]–[3]. In current clinical practice, stress perfusion CMR is assessed visually; however, this requires extensive training and the diagnostic accuracy depends strongly on the operator [4]. As was first suggested more than 20 years ago, it is possible to quantitatively analyse myocardial perfusion in units of $ml \cdot min^{-1} \cdot g^{-1}$ using CMR [5], [6] through the application of the indicator-dilution theory [7], [8]. As yet, quantitative analysis of perfusion CMR remains primarily a research tool but its clinical translation would be advantageous as it can be automated [9], [10], enabling accurate and user-independent assessment of myocardial perfusion [6]. Our group has also recently demonstrated the independent prognostic value of quantitative stress perfusion CMR [11].

The fully automated compensation of respiratory motion is a key milestone in the process of the clinical translation of the quantitative analysis as the inter-frame misalignment caused by this respiratory motion can hamper the accuracy of the analysis. In particular, voxel-wise quantification of perfusion is desirable in order to take advantage of the high spatial resolution of MRI and to enable the accurate detection of sub-endocardial perfusion defects [12]. Such an approach assumes that a voxel represents the same anatomical location in each frame of the image series - i.e. that there is no inter-frame misalignment. When voxel-wise quantification is used, even misalignments as small as one voxel can result in significant errors in the quantitative values.

Current clinical protocols involve acquiring dynamic image series which last 50-90 seconds [13]. Breath-holds can only effectively prevent respiratory motion during a limited time frame of 15-25 seconds, usually during the first-pass of the bolus of contrast agent across the left ventricle (LV) cavity and the LV myocardium. Hence, even when breath-holds are performed, it frequently leads to poor image quality due to the residual motion [14]. This can be worsened by incorrect timing of the breath-hold, resulting in it not coinciding with the passage of the contrast agent in the LV cavity and by the fact that patients with coronary artery disease often struggle to hold their breath properly, especially under the effects of the vasodilator drug.

More recently, some authors [10], [15], [16] have proposed to acquire perfusion images in free-breathing and to apply retrospective motion compensation. This approach has the advantage of being more tolerable for patients and, with good motion compensation, to enable automatically generating accurate voxel-wise perfusion maps without requiring manual segmentation and manual correction of the position of the heart. Furthermore, acquisitions in free-breathing (FB) are more robust when compared to breath-hold (BH) acquisitions when a motion compensation algorithm is used. Shallow free-breathing encourages smooth in-plane motion that aides motion

The authors acknowledge financial support from the King's College London & Imperial College London EPSRC Centre for Doctoral Training in Medical Imaging (EP/L015226/1); Philips Healthcare; The Department of Health via the National Institute for Health Research (NIHR) comprehensive Biomedical Research Centre award to Guy's & St Thomas' NHS Foundation Trust in partnership with King's College London and King's College Hospital NHS Foundation Trust; The Centre of Excellence in Medical Engineering funded by the Wellcome Trust and EPSRC under grant number WT 088641/Z/09/Z.

C. M. Scannell, A. D. M. Villa, J. Lee and A. Chiribiri are with the School of Biomedical Engineering and Imaging Sciences, King's College London.

M. Breeuwer is with Philips Healthcare, Best, The Netherlands and the Department of Biomedical Engineering, Eindhoven University of Technology, The Netherlands.

(Corresponding author: Cian M. Scannell. e-mail: cian.scannell@kcl.ac.uk).

This is the author's version of an article that has been published in this journal. Changes were made to this version by the publisher prior to publication.
The final version of record is available at http://dx.doi.org/10.1109/TMI.2019.2897044

compensation, whereas breath-holds can lead to deep inspiration/expiration and sudden motion both in-plane and through-plane. Additionally, breath-hold scans can also be difficult to retrospectively correct due to the changes in the volumes of the ventricles associated with deep inspiration and expiration [17].

II. BACKGROUND

The problem of motion compensation can be formulated as an image registration problem. The difficulty in the application of image registration to the motion compensation of myocardial perfusion images is due to the rapidly changing signal intensities caused by the arrival and wash-out of the contrast agent in the region of interest. In the case of non-rigid registrations with vastly different signal intensity profiles, it cannot be guaranteed to not introduce unnatural anatomical deformations [18], [19]. The cost functions that are optimised in the image registrations are global measures [20], they assume that the mapping between tissue and image intensity is constant. This underlying assumption is violated by the local intensity changes. As a result, the cost functions cannot distinguish between the intensity variations that are due to spatial motion artefacts and those that are due to the contrast enhancement. For example, when trying to register a frame with contrast enhancement only in the right ventricle to a frame with contrast enhancement only in the left ventricle, the algorithm will likely try to match the left ventricle to the right ventricle. One possible solution to this problem is to only register successive frames in the image series so that the contrast enhancement should be relatively similar. However, this has the effect of propagating the errors from each registration to every subsequent registration. Also, particularly during the passage of contrast agent from the right ventricle to the left ventricle, the intensity change is fast relative to the temporal sampling rate of the image series, leading to vastly differing contrast between successive frames and the potential for failed registrations.

A. State-of-the-art

Several methods to compensate for motion in myocardial perfusion MRI data already exist. Adluru et al. [21], [22] proposed the use of tracer-kinetic models to create synthetic reference images. However, this work only considered rigid registration with breath-hold acquisitions and the more general applicability of the method is unclear. In particular, the model-fitting is likely to be difficult with free-breathing acquisitions. The method of Melbourne et al. [23] proposed to progressively remove motion in the sequence using principal component analysis (PCA). The original sequence can hence be motion compensated by progressively registering to a motionless synthetic image series reconstructed from only early PCs. This is equivalent to an iterative spatio-temporal denoising. However, this theory breaks down if the acquisition is free-breathing or there is large amounts of motion, such as a deep inspiration, present. This is because the non-random effects of the structured motion biases the PCA decomposition. This results in the motion manifesting itself in the early PCs. Hence, registration to the synthetic PCA-based reference image cannot remove the motion. Wollny et al. [15], [24] built on the work of Milles et al. [25] and proposed to use independent component analysis (ICA) to separate the motion from the image series to create synthetic reference images. However, differentiating between the independent components and hence removing the motion is difficult.

More recently, Benovoy et al. and Xue et al. proposed methods, based on optical flow, that are now components of larger software packages for automated quantitative perfusion analysis [16], [26]. These methods however do not explicitly account for the locally-varying contrast enhancement. As demonstrated in Fig. 1, there can be vastly differing contrast profiles between frames. Lingala et al. [27] proposed deformation corrected compressed sensing (DC-CS) which embeds the motion compensation within an iterative reconstruction scheme. The algorithm iterates a reconstruction step with registration to a spatio-temporal denoised reference. However, it is not clear if it is always possible to create a denoised version with no motion but the same contrast profile as the original image series in this way. The technique also requires many iterations of these steps, the main limitations of doing so are the unwanted smoothing of the images caused by iterative registrations and the time complexity of such an approach. This work will be compared extensively to the method proposed in this paper. The review paper of Pontre et al. [28] compared many of the aforementioned techniques but no clear conclusion was reached.

B. Our Contribution

In this study, we propose a robust fully-automated, image-based approach to the motion compensation of free-breathing perfusion MRI image series using a matrix decomposition technique, robust principal component analysis (RPCA) [29] and non-rigid image registration. This approach is based on the observation that RPCA allows the separation of the dynamic contrast enhancement from the baseline signal in a myocardial perfusion CMR images series. Hence, the deformation fields required to eradicate the respiratory motion can be computed in the absence of the locally-varying contrast enhancement and then applied to the original image series to render it motionless. Hamy et al. [30] demonstrated that RPCA allowed motion compensation of data from liver, small bowel and prostate DCE-MRI. In this work, it is shown that RPCA also facilitates the motion compensation of myocardial perfusion MRI data.

This extension is non-trivial due to the fact the images do not just have one enhancing tissue but rather the enhancing tissue is surrounded by the two more intensely enhancing blood pools. Furthermore, the use of a group-wise registration scheme negates the difficulty of choosing a reference frame. The motion compensation is conducted in a two-stage approach, the first stage uses RPCA, as described above, to account for the bulk motion and the second stage is a refinement stage in which the image series is registered to a separate motionless synthetic image series created using PCA [23] (analogous to the spatio-temporal denoising used in DC-CS). The idea is that such a denoising will be much more efficient after the first bulk motion

This is the author's version of an article that has been published in this journal. Changes were made to this version by the publisher prior to publication.
The final version of record is available at http://dx.doi.org/10.1109/TMI.2019.2897044

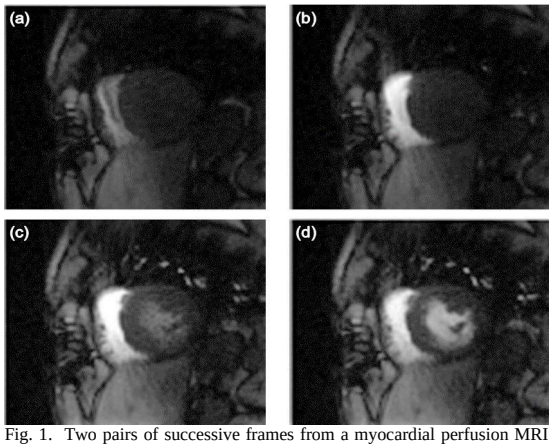

Fig. 1. Two pairs of successive frames from a myocardial perfusion MRI image series. The first pair ((a) and (b)) are during the arrival of contrast agent in the right ventricle and the second pair ((c) and (d)) are during the arrival of contrast agent in the left ventricle. This serves to show that the contrast profile is not necessary similar between two successive frames.

compensation step. The validation is conducted with its clinical applicability in mind, which is achieved through an assessment of the accuracy of myocardial blood flow quantification and by the scoring of expert readers.

III. Theory

A. RPCA

RPCA is a generalisation of traditional principal component analysis which, as its name suggests, attempts to make the algorithm more robust to corrupt data points [29]. It takes advantage of the fact that, in many applications, the data (M) can be modelled as a combination of a low-rank component (L_0) and a sparse component (S_0) such that: $M = L_0 + S_0$. Mathematically this can be formulated as the solution of:

$$\text{argmin}_{L,S} \, ||L||_* + \lambda \, ||S||_1 \;\; \text{s.t.} \;\; L + S = M \qquad (1)$$

where $||\cdot||_*$ is the nuclear norm and is defined as the sum of the singular values of the matrix. $\lambda > 0$ is a trade-off parameter that balances the constraint on the rank of L and the sparsity of S. Large values of λ lead to L having higher rank and S being more sparse ($\lambda \to \infty$ gives $L = M$ and $S = 0$) and conversely smaller values of λ lead to L having lower rank and S being less sparse ($\lambda \to 0$ gives $L = 0$ and $S = M$). The solution of (1) can be obtained through an augmented Lagrangian multiplier method using an alternating directions approach [31].

B. Motion Compensation

Motion compensation was conducted in two stages, this scheme followed from the observation that it is difficult to optimise the parameters of the image registration algorithms to correct for both large and small deformations simultaneously. In stage 1, it is attempted to correct for the bulk motion caused by the respiration and stage 2 is a refinement step which attempts to account for any remaining fine misalignments. The analysis is performed on image series that have been cropped around the region of interest [32], which vastly reduces the time taken for all processing steps. The full scheme is illustrated in Fig. 2.

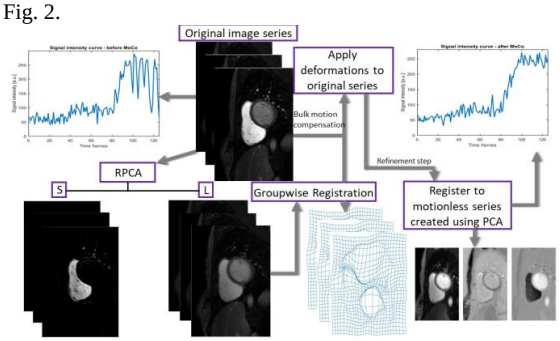

Fig. 2. A flow chart of the proposed motion compensation scheme.

C. Stage 1: bulk motion compensation

As was shown by Hamy et al. [30], when RPCA is applied to a DCE-MRI image series the low-rank component L well models the baseline signal and the sparse component S captures the contrast enhancement. This decomposition is shown for two example frames in Fig. 3, with videos provided in the supplementary material. With a suitable choice of λ, typically taken to be $\lambda = 1/\sqrt{N_p}$ where N_p is the number of pixels in an image [29], it is therefore possible to obtain a low-rank image series L which has a similar motion profile as the original image series but without dynamic contrast enhancement. Traditional image registration techniques can be easily applied to this low-rank series as the contrast is similar in each frame. Thereafter, the deformation fields which are computed from L can then be applied to the original image series to eliminate motion.

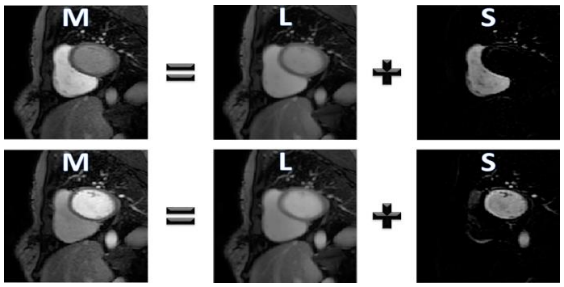

Fig. 3. The RPCA based separation of the example images from the original image series (M) into its low-rank (L) and sparse components (S). As discussed, the local signal enhancement is represented in S with no dynamically changing contrast present in L.

Bulk motion is corrected for using a rigid registration scheme which optimises the mutual information cost function [33]. The registration is applied in a group-wise manner, where all frames are registered to the mean frame in an iterative framework, with the mean frame being updated on each iteration (for a total of 3 iterations). This approach performs well as it uses all information at each stage of the registration as opposed to considering only two frames at a time. It also avoids the uncertainties and errors caused by either developing an algorithm to choose a reference frame or doing so in a random manner. The iterative refinement of the reference frame also avoids the complication of registering two frames which

This is the author's version of an article that has been published in this journal. Changes were made to this version by the publisher prior to publication.
The final version of record is available at http://dx.doi.org/10.1109/TMI.2019.2897044

are far apart; this could lead to unwanted deformations of the anatomy.

D. Stage 2: refinement

After this first bulk motion compensation, it is observed that the remaining motion appears to be jittery and noise-like. Hence, in the second stage, the frames are registered to a synthetic image series which is created using a PCA decomposition to remove the noise-like motion, as was first proposed by Melbourne et al. [23]. Fig. 4 shows an example frame expressed as a linear combination of the three principal eigen-images, a video of such an example series is provided in the supplementary material. Each frame from the image series resulting from stage one is hence registered to the corresponding frame from the motionless PCA-based synthetic image series. The motion profile for this synthetic image series is shown in Fig. 5. The registrations are performed using free-form deformations [34] which optimises the residual complexity cost function [35] and is performed using a Gaussian image pyramid scheme [36]. This step refines the original motion compensation, and as such is performed on a fine grid of control points (grid spacing (h) of 4 pixels) with relatively weak regularisation ($\kappa = 5$). These parameters are similar to the optimal combination for this application found by Wollny et al. [20] ($h = 5, \kappa = 15$). As compared to these values, this method uses a finer grid as it is only being used in the second stage and thus only correcting fine misalignments. This work also uses less regularisation as after the first stage the images are already close to being aligned and thus required less protection against local optima. All processing steps were implemented in Matlab (The MathWorks, Natick, MA, USA) using the Medical Image Registration Toolbox for Matlab [37].

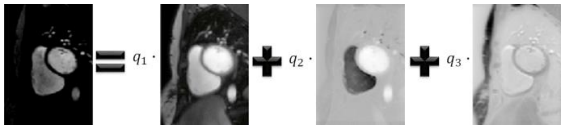

Fig. 4. An example image from the image series which can be expressed as a linear combination of its 3 principal eigen-images.

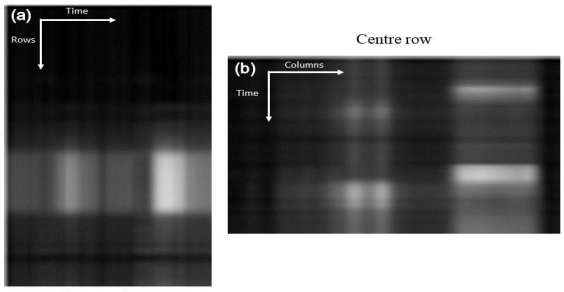

Fig. 5. The motion profile of the synthetic reference. This is constructed by taking the centre column (a) and row (b) from each image in the series and stacking them left to right (a) and top to bottom (b). (a) shows the vertical motion (anterior to inferior) and (b) shows the horizontal motion (septal to lateral). This figure indicates a complete absence of motion.

IV. METHODS

A. Study population and image acquisition

Dynamic perfusion series were prospectively acquired in patients referred for cardiac MRI at the School of Biomedical Engineering and Imaging Sciences, King's College London. Image acquisition was carried out at 3.0T (Philips Achieva-TX, Philips Medical Systems) using standard acquisition protocols [13]. Datasets were acquired either in free-breathing or during breath-holds. There was 16 free-breathing rest acquisitions, 2 free-breathing stress acquisitions and 5 breath-hold stress acquisitions in total. Images were acquired in 3 short axis views using a turbo field echo gradient echo pulse sequence (typical acquisition parameters TR/TE/flip angle/saturation prepulse delay were 2.5 ms/1.25 ms/15° /100 ms) with a typical spatial resolution of 1.34 x 1.34 x 10 mm. The acquisition of the images was synchronised to the cardiac cycle using a vector electrocardiogram trace. The dynamic image series were acquired during first-pass injection of 0.075 mmol/kg Gadobutrol (Gadovist, Schering, Germany) at 4 ml/s followed by a 20 ml saline flush. A dual bolus contrast agent scheme was used to correct for signal saturation of the AIF, as previously described [38]. All patients consented to the CMR scan and to the inclusion in the study (ethics approval number 15/NS/0030). The study was conducted in accordance with the Declaration of Helsinki.

Image series acquired during a breath-hold can contain significant and sudden motion, whereas images acquired in free-breathing contain a smooth, almost periodic breathing pattern [15] due to the encouraged shallow breathing. The motion profile is visualised for an example free-breathing image series in Fig. 6 which shows the vertical (Fig. 6 (a)) and horizontal (Fig. 6 (b)) motion.

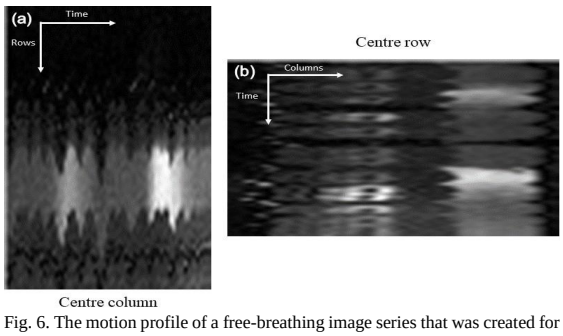

Fig. 6. The motion profile of a free-breathing image series that was created for the same image series as shown in Fig. 5. The motion is represented as the oscillating pattern and is quite severe in this case. As expected, there is strong vertical motion. There is less horizontal motion but it is still present.

B. Evaluation

The method was evaluated in both a qualitative and quantitative manner. All metrics were computed for 48 individual free-breathing rest image series (16 subjects with 3 slices each), 15 breath-hold stress image series and 6 free-breathing stress image series. All subjects were free from ischaemia and scar. Although quantification of myocardial perfusion is routinely done in research settings, it is likely that

This is the author's version of an article that has been published in this journal. Changes were made to this version by the publisher prior to publication.
The final version of record is available at http://dx.doi.org/10.1109/TMI.2019.2897044

visual assessment will remain a part of clinical protocol for the near future. With this in mind, the qualitative facet of the evaluation involved the grading by expert observers. This qualitative assessment compares the original image series to the equivalent image series compensated with both the proposed framework and the DC-CS method [27]. The quantitative assessment involved assessing the temporal smoothness of time-intensity curves while also focusing on the spatial smoothness of the clinically relevant myocardial perfusion values. In the absence of motion, the time-intensity curves should be smooth and the quantitative perfusion maps should be relatively uniform. The quantitative assessment again compares the original image series with the two equivalent motion corrected image series. This follows the recent validation paper of Jansen et al. [39].

The quality of the motion compensation was assessed by two expert observers, blinded to the motion compensation status of the image series, with level III CMR accreditation according to the guidelines of the Society for Cardiovascular Magnetic Resonance (SCMR). The observers (AC and ADMV) viewed the image series and graded each of them on a five point scale. 1=Poor Quality; unnatural deformations, 2=Mediocre Quality; significant motion, 3=Acceptable Quality; some motion, 4=Good Quality; only some unimportant motion, 5=Excellent Quality; no visible motion. The grades from the two observers were deemed to be in agreement if they differed by less than two, otherwise, a consensus grade was reached. The average score from the two observers was then used for assessment.

In the absence of motion, the only change in voxel-intensity is the contrast enhancement. These changes should be smooth and slowly-varying. This assumption is violated in the presence of motion as voxels can represent different anatomical features in consecutive frames. To analyse this temporal smoothness, the standard deviation (SD) of the second derivative of the voxel-wise time-intensity curves was computed and the mean value of this was recorded for each slice. Time-intensity curves were smoothed using a Gaussian filter with $\sigma = 1$ (time frame) in order to reduce the effect of noise. This smoothing was performed in all cases to ensure fair comparison. Only the part of the curve relating to the first-pass of the contrast agent is assessed.

Myocardial perfusion is quantified through the relationship: $C_{myo}(t) = R_F(t) * C_{AIF}(t)$ where R_F, the residue function, is constrained by the Fermi function [5], [6]:

$$R_F(t) = F \cdot \left[\frac{1}{1+\exp[(t-\tau_0-\tau_d)\cdot k]}\right] \cdot \theta(t-\tau_d) \qquad (2)$$

$C_{AIF}(t)$ is the arterial input function and $C_{myo}(t)$ is the concentration of contrast agent in the tissue. An estimate of myocardial blood flow F can hence be obtained by deconvolving the observed tissue curve with the AIF.

The fitting is done with a Levenberg-Marquardt nonlinear least square fitting algorithm. $\theta(t)$ is the unit step function. The algorithm fits for the variables F, k and τ_0 and uses a pre-defined τ_d. The fitted value of F is taken as the estimate of myocardial blood flow, whereas k and τ_0 define the shape of the residue function. Signal-intensity curves are converted to concentration of gadolinium by assuming a linear relationship (this can be assumed due to the dual-bolus acquisition) [40].

Since the image series were acquired from healthy patients, relatively uniform perfusion would be expected through-out the myocardium as there is no stress-induced ischaemia and no scarred tissue, based on the late gadolinium enhancement images. However, this will not be the case in the free-breathing acquisitions due to motion artefacts in the time intensity curves, demonstrated in Fig. 7. Image series were therefore quantified with a previously validated in-house software [41], with the aim of showing that it is possible to obtain more homogenous perfusion maps after motion compensation. In order to make this assessment, the SD of each perfusion map was recorded.

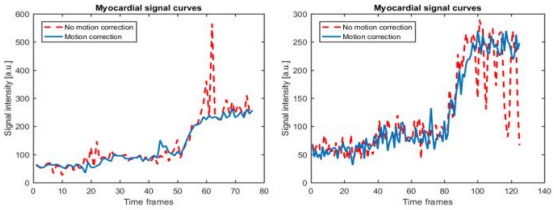

Fig. 7. Voxel-wise time-intensity curves which were extracted from the myocardial segmentation, before and after motion compensation. On the left the motion causes the segmentation of the myocardium to be contaminated by the left ventricle during the upslope of myocardial signal. After motion compensation (right) this effect is corrected and the curves look as expected.

V. RESULTS

A. *Qualitative Assessment*

The expert observers scored the 69 image series with three different motion compensation statuses (no motion compensation, the DC-CS method and the RPCA-based method proposed in this work), leading to 207 individual scores. The two expert observers assigned identical scores to the image series in 63% of the cases. A difference of more than one point was only observed in 4/207 cases and in all of these cases a consensus score was agreed on. This corresponds to an inter-observer Spearman's rank correlation coefficient of 0.80.

The mean grades (SD) after averaging the grades from each observer for the rest image series were 2.1 (0.3), 3.71 (0.64), and 4.10 (0.62) for the original free-breathing image series, the DC-CS corrected image series, and the RPCA corrected image series. The equivalent scores for the stress image series were 2.76 (0.53), 3.19 (0.66) and 3.57 (0.66). The Wilcoxon signed rank test showed that there is a significant (Bonferroni-corrected) difference between all pairs of populations except the stress DC-CS and stress RPCA corrected images (p=0.07). Although in this case the trend suggests that the RPCA correction works better. This shows that not only does motion compensation improve the image quality of free-breathing image series, but also that our proposed two-step approach gives better results than the previously published method [27]. There are no cases in which the non-motion compensated image series scored higher than an equivalent motion compensated image series. There was a positive difference in the score between the RPCA and DC-CS methods in 48% of the image series with a mean improvement of 0.39. Both observers confirmed that they would be satisfied to report on the free-breathing image series in 100% of the cases. Before and after

This is the author's version of an article that has been published in this journal. Changes were made to this version by the publisher prior to publication.
The final version of record is available at http://dx.doi.org/10.1109/TMI.2019.2897044

motion compensation videos are provided in the supplementary materials.

B. *Quantitative Assessment*

In order to assess the temporal smoothness of the time-intensity curves, the second derivatives of the voxel-wise time-intensity curves are examined. The SD of this is then computed for each curve and the mean value is computed over all curves from an individual slice. The median (interquartile range) values were 0.28 (0.14), 0.16 (0.06) and 0.13 (0.06) at rest and 0.14 (0.14), 0.11 (0.09), and 0.09 (0.08) at stress for the non-motion compensated, DC-CS, and RPCA data respectively. Lower values indicate that the change in intensity between two successive images in the series is smooth and hence indicates a likely reduction in the amount of motion. Fig. 8 shows the distribution of these values. The Wilcoxon signed rank test shows that the values for the RPCA-based method differ significantly from the DC-CS method both at rest ($p = 0.013$) and at stress ($p = 0.024$). The two motion compensation schemes are significantly better than no motion compensation both at rest and at stress.

The mean (SD) quantitative perfusion values for the original image series the DC-CS corrected image series, and the RPCA corrected image series are $0.93\ (0.33)$, $0.94(0.40)$, and $0.83\ (0.26)\ ml \cdot min^{-1} \cdot g^{-1}$ at rest and 4.02 (0.91), 4.15 (0.84), and 3.21 (0.73) $ml \cdot min^{-1} \cdot g^{-1}$ at stress respectively. As expected the means are very similar and in line with what we would expect to see [42], the reduction in perfusion after motion compensation is due to the lack of artefacts in the intensity curves. However, what is more telling is that at rest the SD accounts for 73%, 53% and 43% of the mean respectively. Due to motion artefacts both the non-motion compensated free-breathing have a higher SD than the motion compensated image series. The median values of the SD of quantitative perfusion value in each slice for the original, DC-CS corrected and RPCA corrected image series are 0.16, 0.13, and 0.14 at rest and 0.61, 0.69 and 0.45 at stress, respectively. The distribution of these values is visualised, in Fig. 9.

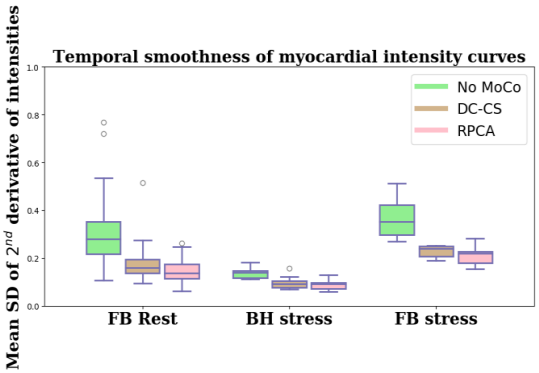

Fig. 8. The values for the mean standard deviation of the 2nd derivative of myocardial time-intensity curves. This indicates the temporal smoothness of the image series. The smoother the transition between successive images in the series the less motion that is present.

The Wilcoxon signed rank test shows that the values for the image series do not differ significantly to those of the two motion compensation schemes, though the trend is clearly visible. The homogeneity of the perfusion maps is improved particularly with the RPCA based method. Furthermore, the homogeneity of the maps at stress for the RPCA corrected image series is significantly improved over the DC-CS corrected image series for both the free-breathing ($p=0.001$) and breath-hold ($p=0.009$) image series.

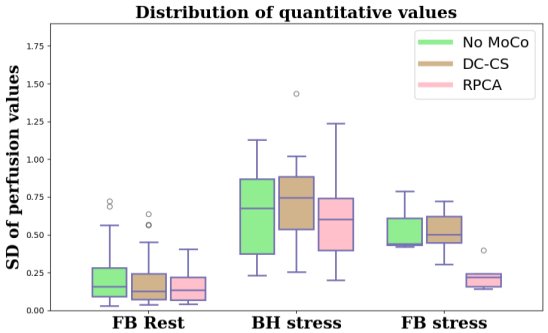

Fig. 9. The values for the standard deviation of perfusion values in each map. Lower standard deviations indicate more homogenous perfusion maps and hence less motion.

VI. Discussion

In this study, we introduced a novel method for robust and fully-automated, image-based motion compensation of free-breathing perfusion CMR image series. This method was validated both qualitatively and quantitatively. The quality of the motion compensation of both rest and stress free-breathing and stress breath-hold image series was graded by two expert observers in comparison with a previously established method. The quantitative assessment compared free-breathing image series that had subsequently been motion compensated to the original image series and also image series acquired with a breath-hold before and after motion compensation. This evaluation focused on the clinically relevant quantitative perfusion values. The results show an improvement in all metrics for the free-breathing image series that have been motion compensated using the proposed method as compared to the original image series (30% reduction in the coefficient of variation across quantitative perfusion maps, 55% reduction in temporal variations ($p<0.001$)). The uniformity of the motion compensated free-breathing stress maps is comparable with the breath-hold stress maps. It follows that it may be possible to omit the breath-hold from the clinical protocol, making the procedure easier for both the patient and the scan operator, encouraging smoother respiratory motion which is easier to correct and reducing the potential for large gasps and through-plane motion.

A. *Qualitative Assessment*

There was a reasonable agreement between observers, with both observers consistently scoring the image series that had been corrected with the RPCA-based method higher than those corrected with DC-CS and those with no motion compensation. Fig. 10 shows the tMIP of each of the three slices for one patient (stress free-breathing) for the three different motion compensation statuses, the increased sharpness of the image

This is the author's version of an article that has been published in this journal. Changes were made to this version by the publisher prior to publication.
The final version of record is available at http://dx.doi.org/10.1109/TMI.2019.2897044

series corrected with and the RPCA based approach (column 3) indicates that there is little residual motion remaining.

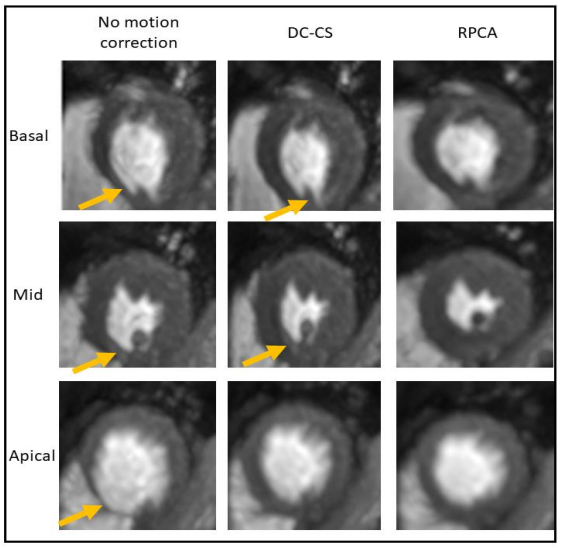

Fig. 10. The temporal maximum intensity projection of the three slices from a free-breathing stress acquisition. The increase in sharpness in the RPCA corrected series indicates a lack of motion. The blurring artefacts as a result of motion are shown with yellow arrows.

B. Quantitative Assessment

The temporal variations of the free-breathing (both rest and stress) image series were significantly reduced (by 55%) compared to that of the original image series. This indicates that the motion compensation is indeed enforcing smooth changes between successive images in the series which in turn indicates the eradication of motion. The temporal smoothness of an example free-breathing image series is visualised through its motion profile in Fig. 11. This is the equivalent image series to Fig. 6. In Fig. 12, the deep inspiration and expiration caused by the breath-hold are obvious. After the breath-hold, large amounts of motion can occur due to the subject being out of breath and gasping for air. However, in general, this motion in the BH image series does not significantly affect the clinically relevant quantitative perfusion values. The Fermi deconvolution only uses the part of the time intensity curves that relate to the first-pass of the contrast agent and this is when the breath-hold takes place. However, the BH image series can still produce less uniform perfusion maps in the case of mistiming or failure of the breath-hold.

This leads naturally to a comparison of the quantitative perfusion values obtained in each case. As previously remarked, due to the patients' status there will be no stress-induced ischaemia and therefore relatively uniform perfusion would be expected throughout the myocardium. In the presence of motion this will not be the case due to the motion artefacts in the time intensity curves, which impacts the deconvolution. As such, the mean standard deviation of the quantitative maps is lower after motion compensation with a reduced variability. This effect is more pronounced under stressed conditions. Breath-hold acquisitions are not robust, mistakes by the operator, failed breath-holds by the patient or differences in cardiac output between individuals can adversely impact on the synchronisation of the acquisition. Hence, there can still be significant motion and mistiming during the first-pass of the contrast across the left ventricle and the left ventricular myocardium in the BH image series. At stress, the quantitative maps computed with the motion corrected FB image series are more homogenous than the maps computed with the BH image series.

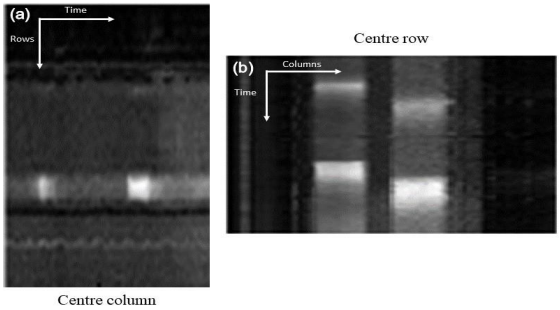

Fig. 11. The equivalent motion profile for the same image series as shown in Fig. 6 after motion compensation. The smooth transition between frames indicates the near-total eradication of motion.

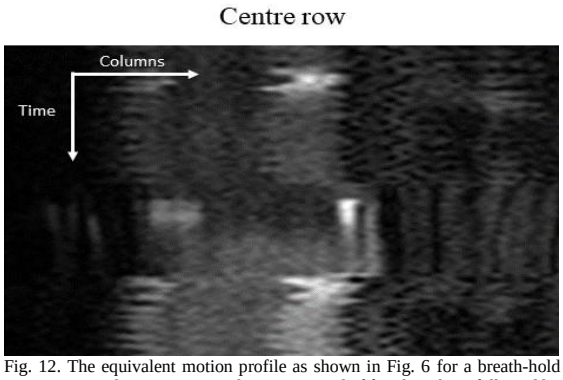

Fig. 12. The equivalent motion profile as shown in Fig. 6 for a breath-hold acquisition. In this image series there is a period of free-breathing followed by a breath-hold during the passage of the main bolus and then another period of free-breathing. The breath-hold is short relative to the passage of the contrast agent, this will impact the tissue curves from the myocardium and subsequently the quantitative perfusion values.

A further consideration that contributes to the improved uniformity of the motion corrected perfusion maps as compared to the BH perfusion maps is the through-plane motion. The "gasp" or period of deep breathing following a breath-hold can cause significant through-plane motion and cannot be retrospectively compensated for using 2D registrations.

The reported results improve on those obtained with previously established methods [27]. Further to the improved results, the proposed method is beneficial as it is faster (3.5 minutes versus 12 minutes on average). From the point of view of timing, it is potentially advantageous that the motion compensation is achieved in two steps rather than in the many iterations of an iterative procedure.

The bulk compensation step can also deal with structured motion (such as periodic motion and large inspiration) better

This is the author's version of an article that has been published in this journal. Changes were made to this version by the publisher prior to publication.
The final version of record is available at http://dx.doi.org/10.1109/TMI.2019.2897044

than the iterative denoising. When compared to directly using the PCA-based approach [23], this approach is deemed to be more applicable to myocardial perfusion imaging. This is because the bulk motion compensation step removes the non-random effects in the data which then allows the successful application of PCA. This leads to better results with both free-breathing and breath-hold data (the clinical standard). Videos which demonstrate the effect of the non-random motion in free-breathing acquisitions on the PCA-based approach are provided in the supplementary material.

The benefits of the proposed approach are that there is no assumptions made on the acquisition system and parameters or even the imaging modality. The resulting motion compensated image series were of higher visual quality. The quantitative information was shown to be preserved after motion compensation, with more robust estimate of myocardial blood flow due to reduced motion artefacts in the signal intensity curves.

C. Limitations

There is a lack of a ground-truth to validate this method. We have attempted to account for this by conducting the evaluation in a multitude of different manners.

To date, the method has only been validated with one set of acquisition parameters. Although we believe there is no reason the acquisition parameters should influence this method, it would be desirable to demonstrate this on further datasets.

Despite the fact this is a 2D compensation for the 3D motion of the heart, image series acquired in the short-axis view with shallow breathing will have predominantly in-plane motion. In our datasets, it is not possible to correct through-plane motion in due to the large slice thickness, large distance between slices and the limited sampling of the left ventricular myocardium.

VII. Conclusion

We have demonstrated the feasibility of a robust fully-automated, image-based approach to the motion compensation of free-breathing perfusion CMR images using the matrix decomposition technique, robust principal component analysis (RPCA) and non-rigid image registration and shown its efficacy using clinical data. With the use of motion compensation algorithms, the evidence presented in this study suggests that a breath-hold protocol for the acquisition of first-pass myocardial perfusion MRI data may be no longer necessary. Motion compensated free-breathing acquisitions led to significantly more uniform quantitative perfusion maps than the original images. The variation of motion corrected free-breathing perfusion maps is equivalent to breath-hold clinical acquisitions. Our method performs well in comparison with the established methods in the literature. Additionally, both expert observers noted that the motion compensated free-breathing image series were all of satisfactory quality for visual assessment. In summary, in addition to the increased convenience of free-breathing acquisition, our motion compensation scheme produces image series of high visual quality and allows the robust quantification of myocardial perfusion.

References

[1] E. Nagel, C. Klein, I. Paetsch, S. Hettwer, B. Schnackenburg, K. Wegscheider, and E. Fleck, "Magnetic resonance perfusion measurements for the noninvasive detection of coronary artery disease," *Circulation*, vol. 108, no. 4, pp. 432–437, 2003.

[2] A. Chiribiri, N. Bettencourt, and E. Nagel, "Cardiac Magnetic Resonance Stress Testing: Results and Prognosis," *Curr. Cardiol. Rep.*, vol. 11, no. 1, pp. 54–60, 2009.

[3] C. Jaarsma, T. Leiner, S. C. Bekkers, H. J. Crijns, J. E. Wildberger, E. Nagel, P. J. Nelemans, and S. Schalla, "Diagnostic performance of noninvasive myocardial perfusion imaging using single-photon emission computed tomography, cardiac magnetic resonance, and positron emission tomography imaging for the detection of obstructive coronary artery disease: A meta-anal," *J. Am. Coll. Cardiol.*, vol. 59, no. 19, pp. 1719–1728, 2012.

[4] A. Villa, L. Corsinovi, I. Ntalas, X. Milidonis, C. M. Scannell, G. Di Giovine, N. J. A. Child, C. Ferreira, M. S. Nazir, J. Karády, E. Eshja, V. De Francesco, N. Bettencourt, A. Schuster, T. F. Ismail, R. Razavi, and A. Chiribiri, "Importance of operator training and rest perfusion on the accuracy of stress perfusion cardiovascular magnetic resonance," *J. Cardiovasc. Magn. Reson.*, 2018.

[5] N. Wilke, M. Jerosch-Herold, Y. Wang, Y. Huang, B. V Christensen, A. E. Stillman, K. Ugurbil, K. McDonald, and R. F. Wilson, "Myocardial perfusion reserve: assessment with multisection, quantitative, first-pass MR imaging.," *Radiology*, vol. 204, no. 2, pp. 373–84, Aug. 1997.

[6] M. Jerosch-Herold, a E. Stillman, and N. Wilke, "Magnetic resonance quantification of the myocardial perfusion reserve with a Fermi function model for constrained deconvolution.," *Med. Phys.*, vol. 25, no. 1, pp. 73–84, 1998.

[7] K. L. Zierler, "Theoretical Basis of Indicator-Dilution Methods For Measuring Flow and Volume," *Circ. Res.*, vol. 10, no. 3, pp. 393–407, 1962.

[8] S. P. Sourbron and D. L. Buckley, "Tracer kinetic modelling in MRI: estimating perfusion and capillary permeability," *Phys. Med. Biol.*, vol. 57, no. 2, pp. R1–R33, 2011.

[9] L.-Y. Hsu, M. Jacobs, M. Benovoy, A. D. Ta, H. M. Conn, S. Winkler, A. M. Greve, M. Y. Chen, S. M. Shanbhag, W. P. Bandettini, and A. E. Arai, "Diagnostic Performance of Fully Automated Pixel-Wise Quantitative Myocardial Perfusion Imaging by Cardiovascular Magnetic Resonance," *JACC Cardiovasc. Imaging*, pp. 1–11, 2018.

[10] P. Kellman, M. S. Hansen, S. Nielles-Vallespin, J. Nickander, R. Themudo, M. Ugander, and H. Xue, "Myocardial perfusion cardiovascular magnetic resonance: optimized dual sequence and reconstruction for quantification," *J. Cardiovasc. Magn. Reson.*, vol. 19, no. 1, p. 43, 2017.

[11] E. C. Sammut, A. D. M. Villa, G. Di Giovine, L. Dancy, F. Bosio, T. Gibbs, S. Jeyabraba, S. Schwenke, S. E. Williams, M. Marber, K. Alfakih, T. F. Ismail, R. Razavi, and A. Chiribiri, "Prognostic Value of Quantitative Stress Perfusion Cardiac Magnetic Resonance," *JACC Cardiovasc. Imaging*, 2017.

[12] N. Zarinabad, A. Chiribiri, G. L. T. F. Hautvast, M. Breeuwer, and E. Nagel, "Influence of spatial resolution on the accuracy of quantitative myocardial perfusion in first pass stress perfusion CMR," *Magn. Reson. Med.*, vol. 73, no. 4, pp. 1623–1631, 2015.

[13] C. M. Kramer, J. Barkhausen, S. D. Flamm, R. J. Kim, and E. Nagel, "Standardized cardiovascular magnetic resonance (CMR) protocols 2013 update," *J. Cardiovasc. Magn. Reson.*, vol. 15, no. 1, pp. 1–10, 2013.

[14] E. Sammut, N. Zarinabad, R. Wesolowski, G. Morton, Z. Chen, M. Sohal, G. Carr-White, R. Razavi, and A. Chiribiri, "Feasibility of high-resolution quantitative perfusion analysis in patients with heart failure.," *J. Cardiovasc. Magn. Reson.*, vol. 17, p. 13, 2015.

[15] G. Wollny, P. Kellman, A. Santos, and M. J. Ledesma, "Nonrigid motion compensation of free breathing acquired myocardial perfusion data," *Med. Image Anal.*, vol. 16, no. 5, pp. 84–88, 2012.

[16] M. Benovoy, M. Jacobs, F. Cheriet, N. Dahdah, A. E. Arai, and L. Y. Hsu, "Robust universal nonrigid motion correction framework for first-pass cardiac MR perfusion imaging," *J. Magn. Reson. Imaging*, vol. 46, no. 4, pp. 1060–1072, 2017.

[17] J. R. Levick, *An introduction to cardiovascular physiology*. Butterworths, 1991.

[18] C. Tanner, J. A. Schnabel, D. L. G. Hill, D. J. Hawkes, A.

Degenhard, M. O. Leach, D. R. Hose, M. A. Hall-Craggs, and S. I. Usiskin, "Quantitative evaluation of free-form deformation registration for dynamic contrast-enhanced MR mammography," *Med. Phys.*, vol. 34, no. 4, pp. 1221–1233, Mar. 2007.

[19] T. Rohlfing, C. R. Maurer, D. A. Bluemke, and M. A. Jacobs, "Volume-preserving nonrigid registration of MR breast images using free-form deformation with an incompressibility constraint," *IEEE Trans. Med. Imaging*, vol. 22, no. 6, pp. 730–741, Jun. 2003.

[20] G. Wollny, M. J. Ledesma-Carbayo, P. Kellman, and A. Santos, "Exploiting Quasiperiodicity in Motion Correction of Free-Breathing Myocardial Perfusion MRI," *IEEE Trans. Med. Imaging*, vol. 29, no. 8, pp. 1516–1527, 2010.

[21] G. Adluru, E. V. R. DiBella, and M. C. Schabel, "Model-based registration for dynamic cardiac perfusion MRI," *J. Magn. Reson. Imaging*, vol. 24, no. 5, pp. 1062–1070, 2006.

[22] D. Likhite, G. Adluru, and E. DiBella, "Deformable and Rigid Model-Based Image Registration for Quantitative Cardiac Perfusion," Springer, Cham, 2015, pp. 41–50.

[23] A. Melbourne, D. Atkinson, M. White, D. Collins, M. Leach, and D. Hawkes, "Registration of dynamic contrast-enhanced MRI using a progressive principal component registration (PPCR)," *Phys. Med. Biol.*, vol. 52, p. 5147–5156 PHYSICS, 2007.

[24] G. Wollny and M.-J. Ledesma-Carbayo, "Comparison of Linear and Non-linear 2D+T Registration Methods for DE-MRI Cardiac Perfusion Studies," Springer, Cham, 2015, pp. 21–31.

[25] J. Milles, R. J. Van Der Geest, M. Jerosch-herold, J. H. C. Reiber, and B. P. F. Lelieveldt, "Fully Automated Motion Correction in First-Pass Myocardial Perfusion MR Image Sequences," *IEEE Trans. Med. Imaging*, vol. 27, no. 11, pp. 1611–1621, 2008.

[26] H. Xue, S. Zuehlsdorff, P. Kellman, A. Arai, S. Nielles-Vallespin, C. Chefd'hotel, C. H. Lorenz, and J. Guehring, "Unsupervised Inline Analysis of Cardiac Perfusion MRI," *Proc. Med. Image Comput. Comput. Interv. (MICCAI).*, 2009.

[27] S. G. Lingala, E. DiBella, and M. Jacob, "(DC-CS): A Novel Framework for Accelerated Dynamic MRI," *IEEE Trans Med Imaging*, vol. 34, no. 1, pp. 72–85, 2015.

[28] B. Pontre, B. R. Cowan, E. DiBella, S. Kulaseharan, D. Likhite, N. Noorman, L. Tautz, N. Tustison, G. Wollny, A. A. Young, and A. Suinesiaputra, "An Open Benchmark Challenge for Motion Correction of Myocardial Perfusion MRI," *IEEE J. Biomed. Heal. Informatics*, vol. 2194, no. c, pp. 1–1, 2016.

[29] E. . Candes, X. Li, Y. Mia, and J. Wright, "Robust principal component analysis?," *Neural Comput.*, vol. 21, no. 11, pp. 3179–3213, 2009.

[30] V. Hamy, N. Dikaios, S. Punwani, A. Melbourne, A. Latifoltojar, J. Makanyanga, M. Chouhan, E. Helbren, A. Menys, S. Taylor, and D. Atkinson, "Respiratory motion correction in dynamic MRI using robust data decomposition registration - Application to DCE-MRI," *Med. Image Anal.*, vol. 18, no. 2, pp. 301–313, 2014.

[31] Z. Lin, R. Liu, and Z. Su, "Linearized Alternating Direction Method with Adaptive Penalty for Low-Rank Representation," in *NIPS*, 2011.

[32] L. Tautz, O. Friman, A. Hennemuth, A. Seeger, and H. O. Peitgen, "Automatic detection of a heart ROI in perfusion MRI images," *Inform. aktuell*, pp. 259–263, 2011.

[33] P. Viola and W. M. Wells, "Alignment by maximization of mutual information," *Proc. IEEE Int. Conf. Comput. Vis.*, vol. 24, no. 2, pp. 16–23, 1997.

[34] D. Rueckert and L. I. Sonoda, "Nonrigid registration using free-form deformations: Application to breast MR images," *IEEE Trans. Med. Imaging*, vol. 18, no. 8, pp. 712–21, 1999.

[35] A. Myronenko and X. Song, "Intensity-based image registration by minimizing residual complexity," *IEEE Trans. Med. Imaging*, vol. 29, no. 11, pp. 1882–1891, 2010.

[36] P. Burt and E. Adelson, "The Laplacian pyramid as a compact image code," *IEEE Trans. Commun.*, vol. 31(4), no. 4, pp. 532–540, 1983.

[37] A. Myronenko, "Medical Image Registration Toolbox," 2009. [Online]. Available: https://sites.google.com/site/myronenko/research/mirt. [Accessed: 14-Aug-2017].

[38] M. Ishida, A. Schuster, G. Morton, A. Chiribiri, S. Hussain, M. Paul, N. Merkle, H. Steen, D. Lossnitzer, B. Schnackenburg, K. Alfakih, S. Plein, and E. Nagel, "Development of a universal dual-bolus injection scheme for the quantitative assessment of myocardial perfusion cardiovascular magnetic resonance.," *J. Cardiovasc. Magn. Reson.*, vol. 13, p. 28, 2011.

[39] M. J. A. Jansen, W. B. Veldhuis, M. S. van Leeuwen, and J. P. W. Pluim, "Evaluation of motion correction of dynamic contrast enhanced MRI of the liver," p. 101331T, 2017.

[40] N. Dikaios, D. Atkinson, C. Tudisca, P. Purpura, M. Forster, H. Ahmed, T. Beale, M. Emberton, and S. Punwani, "A comparison of Bayesian and non-linear regression methods for robust estimation of pharmacokinetics in DCE-MRI and how it affects cancer diagnosis," *Comput. Med. Imaging Graph.*, vol. 56, pp. 1–10, 2017.

[41] N. Zarinabad, A. Chiribiri, G. L. T. F. Hautvast, M. Ishida, A. Schuster, Z. Cvetkovic, P. G. Batchelor, and E. Nagel, "Voxel-wise quantification of myocardial perfusion by cardiac magnetic resonance. Feasibility and methods comparison," *Magn. Reson. Med.*, vol. 68, no. 6, pp. 1994–2004, 2012.

[42] D. A. Broadbent, J. D. Biglands, A. Larghat, S. P. Sourbron, A. Radjenovic, J. P. Greenwood, S. Plein, and D. L. Buckley, "Myocardial blood flow at rest and stress measured with dynamic contrast-enhanced MRI: Comparison of a distributed parameter model with a fermi function model," *Magn. Reson. Med.*, vol. 70, no. 6, pp. 1591–1597, 2013.

Chapter 5

Deep learning-based preprocessing for quantitative myocardial perfusion MRI

5.1 Preface

The field of image processing was revolutionised when a deep convolutional neural network, AlexNet [91], won the ImageNet Large Scale Visual Recognition Challenge by a large margin in 2012 [92]. This was the first demonstration that modern computer hardware, such as graphics processing units (GPUs), could be combined with large databases to train deep neural networks to successfully perform computer vision tasks.

Since this, deep learning has been widely adopted in the field of medical imaging and has become the de facto standard for many processing tasks [93]. Trends in cardiac MRI image analysis have followed a similar route where deep learning is now used for everything from reconstruction to detection and segmentation tasks to automating diagnostics and prognostics [94].

The main advantage of deep learning is that the networks learn the features to be used to complete the task from the data rather than these being hand-engineered. Such hand-crafted features are biased by preconceived ideas of the programmer and thus tend to be brittle. An example of this, in the context of perfusion CMR, is the problem of bounding box detection which is a common first step in processing pipelines. Before the advent of deep learning, a popular approach for this task was based on thresholding temporal variances. The logic behind this was that the contrast flowing causes the areas of highest temporal variance to be the RV and LV cavity. However, this approach was shown to fail in 4/44 case [95] and we found similarly high rates of failure in our implementation. An example of this algorithm with some of the common failure modes is shown in Figure 5.1. For this reason, deep learning is used in this

work for the image processing required to turn the raw image series into concentration curves for tracer-kinetic modelling.

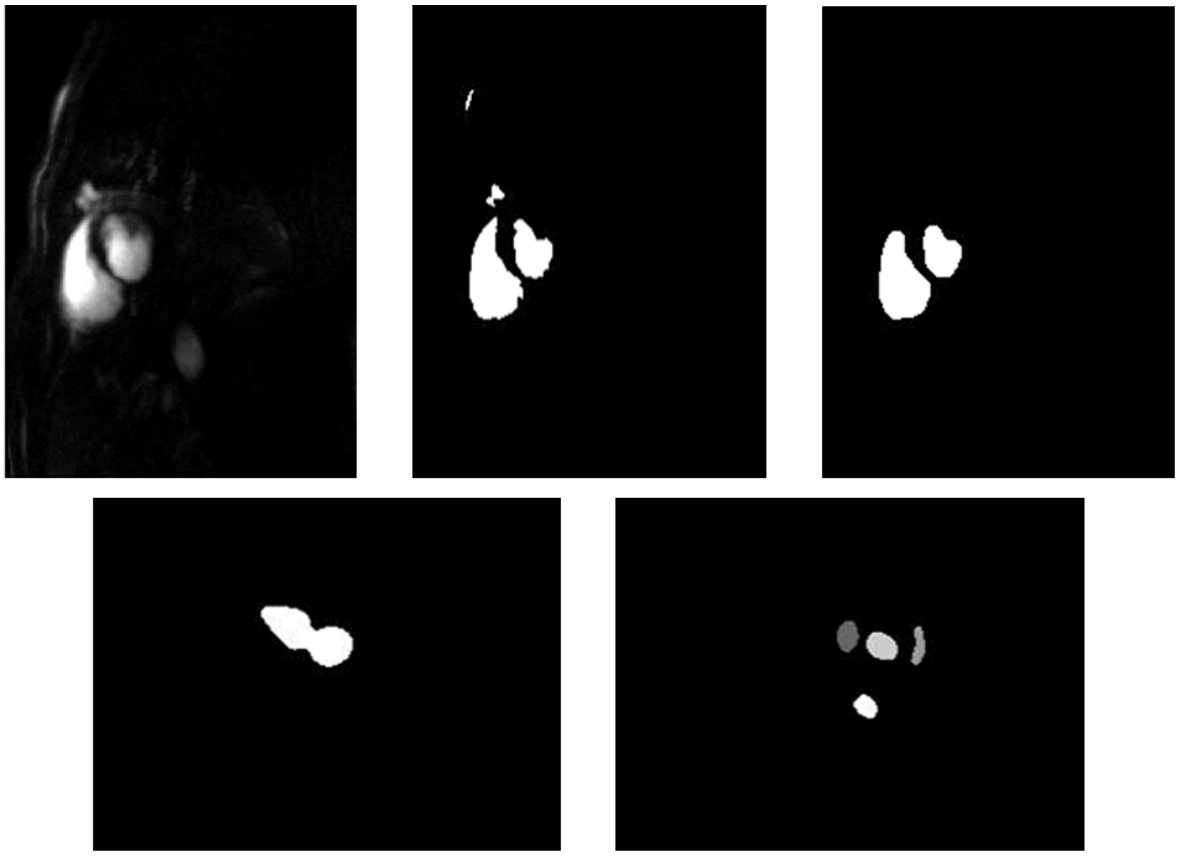

Fig. 5.1 The top row shows the temporal standard deviation image, the thresholded standard deviations, and the result of the connected component analysis to identify the RV and LV (from left to right). The bottom row shows two failed cases. On the left, there only one component (a joint LV and RV) is identified and on the right four similar components are identified.

5.1.1 Supervised deep learning for image processing

Supervised learning

Supervised learning attempts to learn a model that takes input data and outputs labels [96]. That is, to learn the function f which depends on parameters θ that best maps the input space X to the output space Y:

$$f_\theta : X \to Y. \tag{5.1}$$

A training set of matched data and labels is required to find the best set of model parameters to map the input data to labels. The trained models can subsequently be applied to unseen test data to obtain a prediction of its label. This is opposed to unsupervised learning which attempts to learn structure in the data [96].

Deep learning

Deep learning is the sub-field of machine learning based primarily on the use of neural networks [96]. Artificial neural networks are functions made up of layers of units or neurons. Each unit in a layer takes, as input, the output of the units in the previous layer. It then computes a weighted combination of these inputs and applies a non-linear activation function. The weights needed for the weighted combination are the parameters of the neural network and are optimised in order to solve the task at hand. The typical neural networks composes many internal layers and are thus described as deep. A simple neural network, with two hidden layers (layers in addition to the input and output layers), is illustrated in Figure 5.2 As previously discussed, the early layers can be thought of as extracting features from the input data, while the later layers learn to combine these features to meet the objective. This yields a model function in the form:

$$f_\theta(x) = f^L_{\theta_L}(f^{L-1}_{\theta_{L-1}}(\cdots f^0_{\theta_0}(x)\cdots)) \tag{5.2}$$

where $f^i_{\theta_i}$ is the i^{th} layer with parameters θ_i.

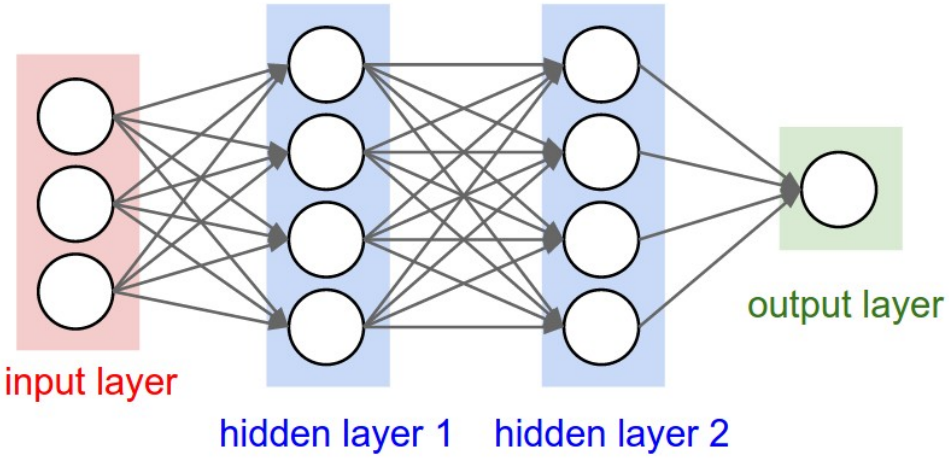

Fig. 5.2 A fully-connected neural network with two hidden layers, image taken from https://cs231n.github.io/.

Convolutional neural networks

A network where all units are connected to all units in the previous layer is said to be fully-connected. This design is inefficient or infeasible for image processing because of the high dimensionality of the inputs (the dimensionality is equal to the number of pixels or voxels in the image). An alternative network design, more suitable for image processing, is the convolutional neural network (CNN), as visualised in Figure 5.3. A CNN combines inputs from only a small region of the previous layer (commonly referred to as the receptive field and designed to loosely resemble the visual cortex). This is implemented as a learnable kernel being convolved with the output of the previous layer to generate the input for the current layer. The convolutional kernel is designed to be significantly smaller than the size of the activation it is being convolved with. This enforces sparse interactions between layers and allows the extraction of low level features, such as edges, without considering the whole image. Parameter sharing is also used such that the same kernel is applied to all inputs to a layer. This aids the training process by greatly reducing the number of parameters to be learned. CNNs also encourage translational invariance in the predictions. Since a kernel slides over the whole input it will detect the same features regardless of their position. This is useful, for example in classification tasks, when it only matters if an object is in an image and not where it is [96].

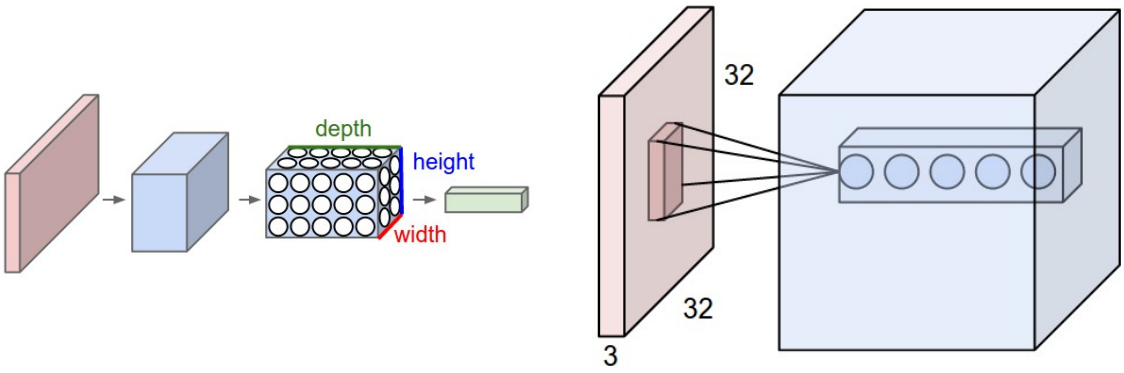

Fig. 5.3 A convolutional neural network. This shows the layers of the CNN downsampling the input image and producing a 3D volume of activation (left), and a unit connected to a small receptive field in the previous layer (right), image taken from https://cs231n.github.io/

U-Net

The most commonly used network architecture for medical image processing is the U-Net [97]. This is a fully-convolutional network in that it only uses convolutional layers, and is illustrated in Figure 5.4. The architecture has an encoder-decoder structure. The encoder downsamples the input image, using max-pooling, to create a low-dimensional embedding.

The multi-step downsampling allows the learning of feature representations at different image scales. The decoder, takes the low-dimensional embedding and upsamples it to try predict the desired output, typically a segmentation map. The network also utilises skip connections that concatenate the activations of the encoder to the corresponding resolution level of the decoder. This is thought to better allow the recovery of the fine-grained details in the prediction.

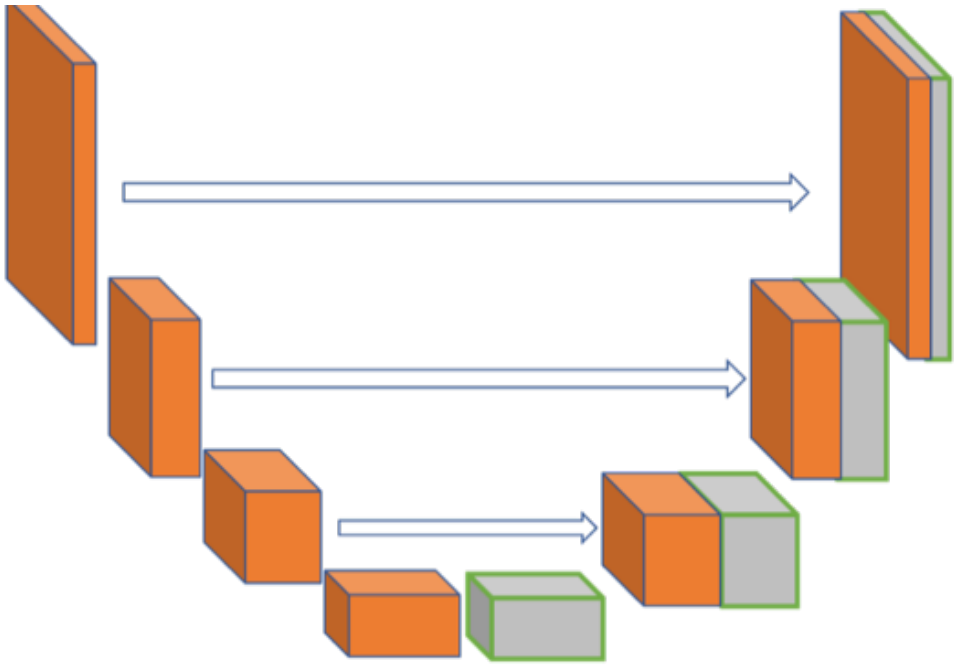

Fig. 5.4 The U-Net model architecture, image adapted from https://www.nist.gov/.

Training neural networks

Neural networks can be trained (the optimal parameters estimated) using first-order stochastic optimisation algorithms to minimise a loss function $\mathscr{L}$ between the estimated network output $\hat{y}$ and the training labels y. The most simple approach to this is stochastic gradient descent:

$$\theta \leftarrow \theta - \alpha \nabla_{\theta} \mathscr{L}(y, \hat{y}) \tag{5.3}$$

where α is the learning rate that controls the size of the parameter updates made in the optimisation. The algorithm is referred to as stochastic as it does not consider the whole dataset at each iteration, for computational efficiency. Parameter updates are instead made using the gradients computed on a small sub-sample of the training data, known as a mini-batch. Due to the layer-wise nature of neural networks, as seen in Equation 5.2, the gradient of the loss

with respect to the parameters of a layer can be computed using the chain rule, in a process is known as backpropagation.

A more advanced (and recently more popular) gradient descent update rule is the ADAM optimiser [98] which uses adaptive learning rates and momentum to achieve better convergence properties [96].

5.2 Journal article

The following text is reproduced as published [99]:

***Scannell, C.M.**, Veta, M., Villa, A.D.M., Sammut, E., Lee, J., Breeuwer, M. & Chiribiri, A. Deep-Learning-Based Preprocessing for Quantitative Myocardial Perfusion MRI. J. Magn. Reson. Imaging 51, 1689–1696 (2020).*

ORIGINAL RESEARCH

Deep-Learning-Based Preprocessing for Quantitative Myocardial Perfusion MRI

Cian M. Scannell, MRes,[1,2] Mitko Veta, PhD,[3] Adriana D.M. Villa, MD, PhD,[1] Eva C. Sammut, MD, PhD,[1,4] Jack Lee, DPhil,[1] Marcel Breeuwer, PhD,[3,5] and Amedeo Chiribiri, MD, PhD[1]*

Background: Quantitative myocardial perfusion cardiac MRI can provide a fast and robust assessment of myocardial perfusion status for the noninvasive diagnosis of myocardial ischemia while being more objective than visual assessment. However, it currently has limited use in clinical practice due to the challenging postprocessing required, particularly the segmentation.
Purpose: To evaluate the efficacy of an automated deep learning (DL) pipeline for image processing prior to quantitative analysis.
Study Type: Retrospective.
Population: In all, 175 (350 MRI scans; 1050 image series) clinical patients under both rest and stress conditions (135/10/30 training/validation/test).
Field Strength/Sequence: 3.0T/2D multislice saturation recovery T_1-weighted gradient echo sequence.
Assessment: Accuracy was assessed, as compared to the manual operator, through the mean square error of the distance between landmarks and the Dice similarity coefficient of the segmentation and bounding box detection. Quantitative perfusion maps obtained using the automated DL-based processing were compared to the results obtained with the manually processed images.
Statistical Tests: Bland–Altman plots and intraclass correlation coefficient (ICC) were used to assess the myocardial blood flow (MBF) obtained using the automated DL pipeline, as compared to values obtained by a manual operator.
Results: The mean (SD) error in the detection of the time of peak signal enhancement in the left ventricle was 1.49 (1.4) timeframes. The mean (SD) Dice similarity coefficients for the bounding box and myocardial segmentation were 0.93 (0.03) and 0.80 (0.06), respectively. The mean (SD) error in the RV insertion point was 2.8 (1.8) mm. The Bland–Altman plots showed a bias of 2.6% of the mean MBF between the automated and manually processed MBF values on a per-myocardial segment basis. The ICC was 0.89, 95% confidence interval = [0.87, 0.90].
Data Conclusion: We showed high accuracy, compared to manual processing, for the DL-based processing of myocardial perfusion data leading to quantitative values that are similar to those achieved with manual processing.
Level of Evidence: 3
Technical Efficacy Stage: 1

J. MAGN. RESON. IMAGING 2019.

FIRST-PASS MYOCARDIAL PERFUSION IMAGING with cardiac magnetic resonance imaging (MRI) has been shown to be highly accurate for the detection of coronary artery disease (CAD)[1,2] and suitable for guiding the management of patients with an intermediate risk of CAD.[3,4] Visual interpretation of the images, however, is complex, time-consuming, and

View this article online at wileyonlinelibrary.com. DOI: 10.1002/jmri.26983

Received Apr 15, 2019, Accepted for publication Oct 16, 2019.

*Address reprint requests to: A.C., School of Biomedical Engineering and Imaging Sciences, King's College London 4th Floor Lambeth Wing, St Thomas' Hospital, Westminster Bridge Road, London SW1 7EH 9, UK. E-mail: amedeo.chiribiri@kcl.ac.uk

Contract grant sponsor: King's College London & Imperial College London EPSRC Centre for Doctoral Training in Medical Imaging; Contract grant number: EP/L015226/1; Contract grant sponsor: Philips Healthcare; Contract grant sponsor: Alan Turing Institute; Contract grant number: EPSRC EP/N510129/1; Contract grant sponsor: Department of Health via the National Institute for Health Research (NIHR) comprehensive Biomedical Research Centre award to Guy's & St Thomas' NHS Foundation Trust in partnership with King's College London and King's College Hospital NHS Foundation Trust and via the NIHR Cardiovascular MedTech Co-operative at Guy's and St Thomas' NHS Foundation Trust; Contract grant sponsor: Centre of Excellence in Medical Engineering funded by the Wellcome Trust; Contract grant number: EPSRC WT 088641/Z/09/Z.

From the [1]School of Biomedical Engineering and Imaging Sciences, King's College London, UK; [2]Alan Turing Institute London, UK; [3]Department of Biomedical Engineering, Medical Image Analysis group, Eindhoven University of Technology, Eindhoven, The Netherlands; [4]Bristol Heart Institute and Translational Biomedical Research Centre, Faculty of Health Science, University of Bristol, UK; and [5]Philips Healthcare, Best, The Netherlands

Additional supporting information may be found in the online version of this article

Journal of Magnetic Resonance Imaging

the accuracy of the results is dependent on the level of training and experience of the operator, thereby limiting the adoption of these techniques outside highly experienced centers.[5]

An alternative to the visual assessment is quantitative perfusion analysis, which is made possible by the use of tracer-kinetic modeling.[6] Quantitative perfusion analysis can be automated[7,8] leading to fast, robust, and reproducible estimates of myocardial perfusion.[9] Quantitative analysis has been validated against positron emission tomography (PET),[10–12] fractional flow reserve,[13] and microspheres.[14,15] Sammut et al have also recently demonstrated the independent prognostic value of quantitative stress perfusion MRI in patients with suspected CAD.[16] The availability of automated and standardized methods for quantitative analysis could facilitate the wider adoption of first-pass myocardial perfusion imaging.

The quantitative analysis requires challenging image processing.[17] It is required to identify the left ventricular blood pool to extract an arterial input function (AIF) to use along with the myocardial tissue curves in the model fitting. The segmentation of the myocardium is also desirable, as it allows the analysis of values specifically in the region of interest (ROI) and the computation of the myocardial perfusion reserve (MPR), which is the ratio of perfusion values at stress to the values at rest. The use of a segmentation also requires fewer voxels to be fit to the model, which is more time-efficient and allows the use of more advanced fitting algorithms that take advantage of spatial information.[18,19] Further advanced analysis techniques involve the assessment of the transmural gradient in contrast uptake across the myocardium[20] or the assessment of the temporal dyssynchrony of first-pass perfusion,[21] for which an ROI is necessary. The identification of the right ventricular (RV) insertion points would also be beneficial in order to divide the myocardial segmentation into the standard American Heart Association (AHA) segments[22] and to relate perfusion abnormalities to coronary territories.

Myocardial perfusion image series present unique challenges to automated segmentation approaches due to the dynamic contrast-enhancement and the relatively low signal-to-noise ratio (SNR). We propose that the automation of these processing steps can be achieved by leveraging the power of machine learning. In particular, deep learning has produced impressive results in many computer vision tasks such as image detection and recognition. Recently, deep learning has also seen more attention in the field of medical image analysis[23] and specifically in cardiac MR image analysis with fully convolutional neural networks (FCNs) being applied to the segmentation of anatomical structures in a variety of different applications.[24,25]

In this work, we developed deep-learning models in order to achieve the requisite preprocessing steps prior to quantitative modeling. These steps were tested individually and as part of the fully-automated pipeline.

Materials and Methods

Subjects

The dataset consisted of 175 subjects (64.3 ± 10.3 years old; 136 male) with suspected CAD referred on a clinical basis to King's College London Cardiac MR Service at St Thomas' Hospital (Guy's and St Thomas' NHS Trust). The dataset was randomly split into three sets of 135/10/30 for training/validation/testing. The full demographic and clinical characteristics of the patients is reported in the Supplementary Material, Table S1. The study was conducted in accordance with the Declaration of Helsinki (2000) and was approved by the National Research Ethics Service (15/NS/0030). All patients provided written informed consent.

Imaging

All examinations were performed with a 3T system (Achieva TX, Philips Healthcare, Best, The Netherlands) using a 32-channel cardiac phased array receiver coil. Perfusion images were acquired in three left ventricle (LV) short-axis slices (apical, mid-cavity, and basal) at mid-expiration with a saturation-recovery gradient echo method (repetition time / echo time 3.0/1.0 msec, flip angle 15°, saturation-recovery delay 120 msec, 5-fold *k-t* sensitivity encoding [*k-t* SENSE] acceleration with 11 training profiles, giving a net acceleration of 3.8-fold, spatial resolution $1.2 \times 1.2 \times 10$ mm^3). Stress images were acquired during adenosine-induced hyperemia (140 μg/kg/min); 0.075 mmol/kg of bodyweight gadolinium (Gd) extracellular contrast agent (gadobutrol, Gadovist, Bayer, Germany) was injected at 4 mL/s followed by a 20-mL saline flush for each perfusion acquisition. Each bolus of gadobutrol was preceded by a diluted prebolus with 10% of the dose to allow quantification of perfusion, according to published methods.[26]

Processing Pipeline

As shown in Fig. 1, the first step of the pipeline is to detect the timeframe from the image series that corresponds to peak signal enhancement in the LV. Using this image, a bounding box is detected that encompasses the LV cavity and LV myocardium. The cropped image series are then passed to the motion correction scheme that we have described in detail in previous work.[27] The next step involves segmenting the motion-corrected and cropped peak LV contrast-enhancement timeframe to generate a myocardial mask and then the RV insertion points are detected. The AIF is extracted from a region identified using a region-growing algorithm starting from the position of highest signal inside the endocardial boundary, as defined by the automated segmentation. The AIF along with the voxelwise concentration curves extracted from the myocardium are then used for perfusion quantification using tracer-kinetic modeling. The RV insertion points are used to relate the quantitative perfusion values to AHA 16-segment model. The full pipeline proposed in this section is summarized in Fig. 1.

Each constituent component of the pipeline was evaluated using a suitable metric. Furthermore, the quantitative perfusion values achieved with the fully automated pipeline were then compared to those achieved using the manual analysis from an expert operator. This allows the assessment of the effectiveness of the whole pipeline and demonstrates the feasibility of its unsupervised deployment in the clinic.

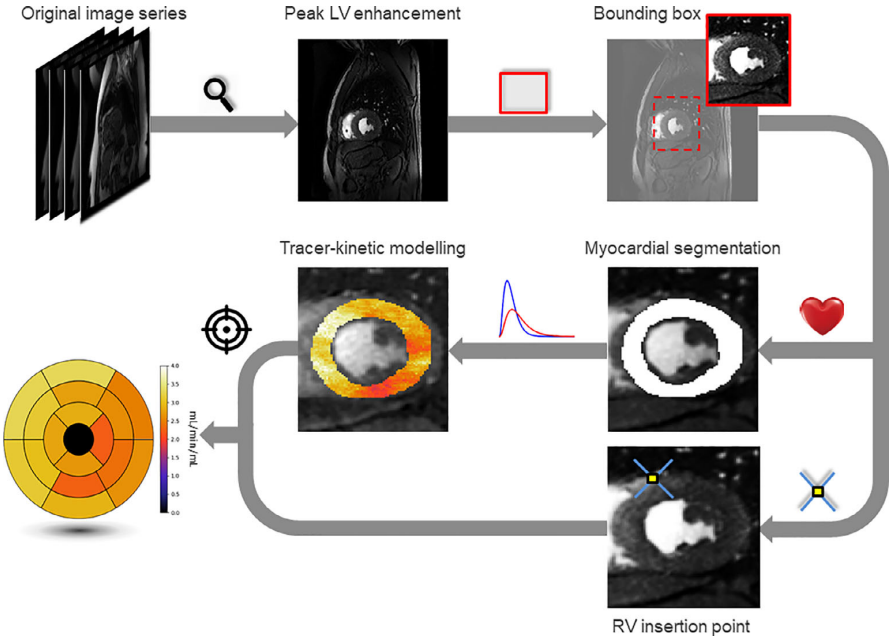

FIGURE 1: The flow chart representing the pipeline for automated myocardial perfusion quantification. The peak LV enhancement frame in the image series is first identified. This timeframe is then cropped (motion correction is then applied), the myocardium segmented, and RV insertion point determined. Perfusion is quantified using tracer-kinetic modeling in the myocardium and this is combined with the RV insertion point to generate the bullseye plot.

Training Labels

The epicardial and endocardial borders were manually traced at the time of peak LV enhancement using cvi[42] software (Circle Cardiovascular Imaging, Calgary, Alberta, Canada) by an experienced operator (E.S., level 3 competency accreditation,[28] with more than 5 years of experience in cardiac MRI). The RV insertion points were subsequently marked. The timepoint was found by scrolling through the timeframes in the viewer until a satisfactory frame was reached and this timepoint was used for training the LV peak enhancement classifier. The training labels for the bounding box were obtained from the segmentation by computing the smallest box that fits the entire myocardium and expanding it by 20 voxels in each dimension. This analysis was repeated by a second experienced operator (A.V., level 3 accredited[28] with more than 5 years of experience in cardiac MRI) for the test set to assess the inter-observer variability rate.

Training Details

Each of the 175 patients in the dataset underwent perfusion imaging under both rest and stress conditions in which three LV short-axis slices were acquired yielding a total of 1050 (three imaging planes at both rest and stress for each patient) individual image series. The networks were trained individually for each of the four steps. Prior to training, the images were interpolated to the required dimension, as described in the individual sections, using bicubic interpolation. All images were normalized to have intensity values in the range of [0,1]. On-the-fly data augmentation was applied to the training images, which consists of applying random amounts of translation, rotation, scaling, intensity variation, and noise to the images. A batch size of 32 was used in the training of all networks. L2 regularization on the parameters of the convolution kernels was used with a weight of 0.001. The respective cost functions were optimized using the Adam optimizer[29] with a learning rate of 0.0001 until convergence. Early stopping with a patience of 3000 iterations, assessed using the validation accuracy, was used to determine convergence.

Peak LV Enhancement Detection

A convolutional neural network (CNN) was used to identify the timeframe corresponding to peak contrast-enhancement in the LV. The CNN takes each timeframe in the image series (256 × 256 voxels) along with the two preceding and two subsequent timeframes as input and outputs as a single number that represents the probability that that timeframe corresponds to the peak LV enhancement in the series. The CNN consists of four convolutional layers followed by two fully-connected layers and is similar to those previously shown to be successful for image recognition tasks.[30] Each convolutional layer uses 3 × 3 kernels and is followed by a 2 × 2 max-pooling layer. It uses batch normalization and rectified linear unit (ReLU) activations except for the output layer, which uses a softmax activation, as shown in the Supplementary Material, Table S2. Dropout is used with probability 0.5 in the fully-connected layers. The model was trained by minimizing the cross-entropy loss function.

In order to identify the time of peak LV enhancement in a new image series, the trained classifier was applied individually to each timeframe in the image series. This approach gives a probability for each timeframe to be the peak LV enhancement image. The timeframe with the highest probability is taken as the estimate. A plot of the probability over time for an image series is shown in the Supplementary Material, Fig. S1.

Journal of Magnetic Resonance Imaging

Bounding Box Detection

The architecture used to detect the bounding box is the same as that used in the previous step except that the output is now four continuous values rather than the class probabilities (a linear activation is used for the four output units). The network takes the frame of peak LV enhancement as input (256×256 voxels) and outputs the parameters that define the bounding box. It is, however, known to be challenging to train a network to directly detect the coordinates of the corners of the bounding box.[31] A solution to this problem was inspired by the idea of region proposals used by the Faster R-CNN architecture.[32] That is, it first assumes that the object, which in this case is the LV cavity and LV myocardium, is within a 75×75 voxel ROI centered around the center of the image. The CNN then outputs how much to adjust this ROI so that it better fits the area of interest. The output of the CNN is the displacement of the center of the proposed ROI and scaling factors for the width and height of the proposed ROI. An example image is shown in Fig. 2, with the original proposed ROI and the identified deformation. The mean squared error between the computed transformation of the proposed ROI and the true transformation required was optimized. The CNN was trained using only the peak LV enhancement timeframe from the basal slice and during testing is only applied to the basal slice. Due to the shape of the LV and the planning of the short axis, the bounding box computed on the basal LV slice also applies to the mid-ventricular and apical slices.

Myocardial Segmentation

The myocardial segmentation utilizes the U-Net architecture,[33] which is a fully convolutional network. The input to the network is an image of size 96×96 voxels (the cropped and motion-corrected peak LV enhancement frame) and the output is an image of the same size which corresponds to the voxelwise classifications of the myocardium. The architecture is summarized in the Supplementary Material, Table S3. The cost function that was optimized was the Dice similarity coefficient (DSC)[34] between the detected segmentation and the human operator segmentation.

The final segmentation is taken as the largest connected component of the binary mask. Failed segmentations are detected automatically by assessing whether the segmentation achieves the expected "closed-loop" shape of the myocardium. In the case of a failed segmentation, a correction is attempted in a similar manner to Fahmy et al.[25] As previously described, the nearby timeframes have very similar appearances. Therefore, in the case of a failed segmentation, the segmentation network is applied to all images within two timeframes of the detected peak LV enhancement. The segmentation from the closest timeframe that achieves the expected shape is taken as the segmentation.

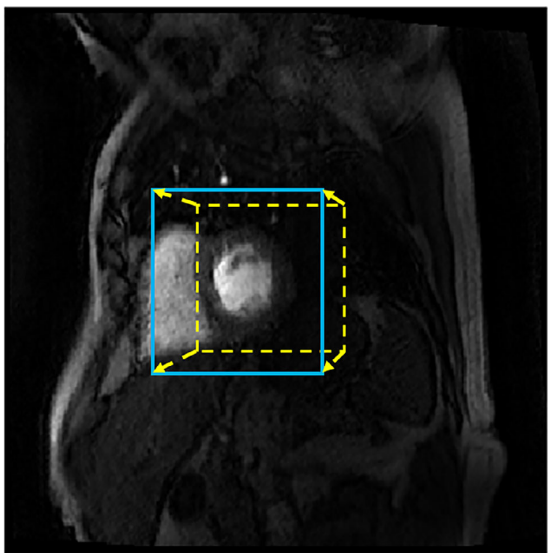

FIGURE 2: The original proposed ROI (dotted line yellow bounding box) for an example patient. The arrows indicate the deformation output by the CNN to give the ROI for this patient with the detected bounding box shown as the blue continuous line bounding box.

Insertion Point Detection

The problem of detecting landmarks in medical images is known to be challenging.[35] This is due to the high noise levels, large variation in the location of the landmark across subjects, and differences due to subjective positioning of the landmarks by different operators. This makes it extremely difficult to train a regression model to output the coordinates of the landmark. An image-to-image approach such as U-Net can be used to output a segmentation that contains just the one voxel of the landmark location. However, such an approach suffers from the class imbalance problem.

Our approach builds on the idea of supervised action classifiers, as proposed by Xu et al.[31] For each case, an action map is created that represents for each voxel in the image the direction (left, right, up, or down) towards the landmark. An example activation map is shown in Fig. 3 (right). An FCN was then trained to detect which one of these four partitions each voxel belongs to. The U-Net architecture is used here and is the same as was used for the myocardial segmentation except for the output activation, which is a softmax rather than a sigmoid to reflect the fact that this is now a multiclass classification problem. The cross-entropy loss function was optimized. From the computed activation maps, regression lines were fit to the boundaries of the partitions and the estimate of the RV insertion point was taken as the intersection of these lines, as shown in Fig. 3 (left).

Evaluation

Each step of the pipeline was evaluated individually by computing a relevant metric for each patient in the test set. For the peak LV enhancement frame detection, the mean difference (in number of timeframes) between the visually chosen timeframe and the detected timeframe was used to evaluate the performance. For both the bounding box detection and the myocardial segmentation steps, the DSC between the outputs and those that were manually acquired is reported. For the segmentation, the metric is compared to the inter-observer variability rate found from repeated segmentations by different operators. For the RV insertion points, the Euclidean distances in terms of mm was used to measure the performance.

Perfusion Quantification

Quantitative perfusion analysis was performed on the test cases using both the manually obtained labels and the deep-learning outputs. The perfusion quantification used a two-compartment exchange model[6] for which the kinetic parameters were inferred using

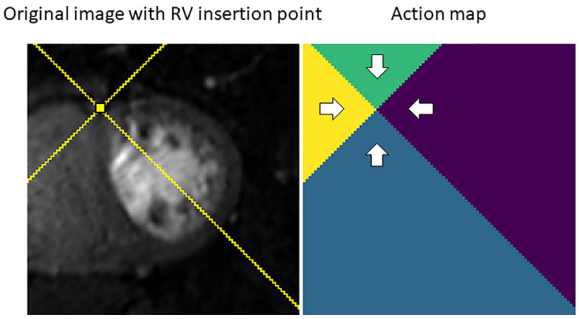

FIGURE 3: Left: the RV insertion point marked on an example patient with the lines of slope ± 1 that separate the regions of the action map overlaid. Right: The resulting action map, with the direction towards the landmark point shown for each pixel.

hierarchical Bayesian inference, as previously described.[19] Bland–Altman analysis was used to analyze the bias and limits of agreement between the manual and automated analysis and the linear relationship and intraclass correlation (ICC) between the obtained quantitative values was assessed.

Results

Representative example cases, with a comparison between manual and automated processing, are shown in Supplemental Figs. S3–S7.

Peak LV Enhancement Detection

The accuracy of the classifier when applied individually to images in the test set was 97.6%. When the peak LV enhancement frame was chosen, as described in the Methods section, the mean (standard deviation [SD]) difference in terms of timeframes (n = 60, 30 patients rest and stress) was 1.48 (1.4). The maximum error was three timeframes. It can be noted that even in this case the detected timeframe is very similar to the manual choice and is a reasonable choice for the peak LV enhancement frame, shown in Supplementary Material Fig. S2.

Bounding Box Detection

The mean (SD) DSC between the detected and manually selected bounding box for the test set (n = 60, 30 patients rest and stress) was 0.93 (0.03).

Myocardial Segmentation

The mean (SD) DSC between the automated and manual segmentations (n = 180, 30 patients with three imaging slices rest and stress) was 0.80 (0.06). The lowest DSC recorded on the test set was 0.69; this image with its corresponding manual and automated segmentation is shown in Fig. S5d. The segmentation of 5 out of 180 test images failed and they were replaced with a successful segmentation computed using a nearby timeframe. The mean (SD) DSC between the segmentations of observer 1 and observer 2 was 0.83 (0.05). Some example images from the different observers are shown in Supplementary Material Fig. S8.

RV Insertion Point Detection

The mean (SD) Euclidean distance (in mm) between the automated and manually chosen RV insertion points (n = 360, 180 imaging slices × 2 insertion points) was 2.8 (1.8).

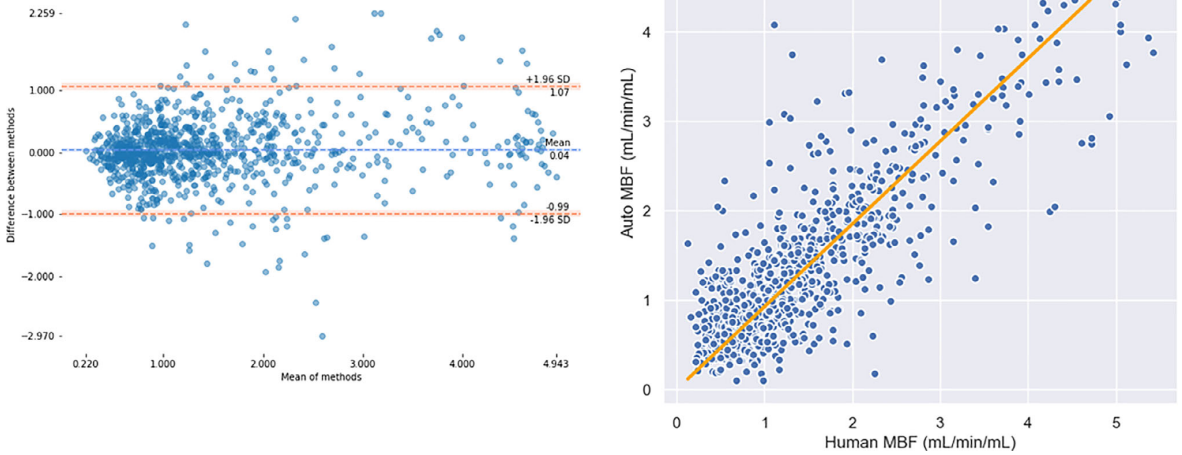

FIGURE 4: Left: Bland–Altman plots of the automatically processed vs. manually processed quantitative perfusion values averaged over each of the 16 AHA segments. Blue and orange lines represent the bias and ± 1.96 SD limits, respectively, with the shaded regions being the 95% confidence intervals. Right: A scatterplot of the manually processed vs. the automatically processed quantitative perfusion values averaged over each segment of the myocardium. The plotted line is the computed line of best fit with no intercept (slope = 0.93).

Perfusion Quantification

The automatically and manually processed test image series resulted in a mean (SD) myocardial blood flow (MBF) of 0.93 (0.37) and 0.91 (0.39) mL/min/mL at rest (n = 90) and 2.04 (0.89) and 2.09 (1.26) under stress (n = 90), respectively. These values are in line with the ranges previously reported in the literature.[7,8,36] The use of the RV insertion points further allows the division of the myocardium from the three acquisition slices into the AHA 16-segment model. The Bland–Altman analysis showed a good agreement between the automated and manual MBF values on a per-segment basis (n = 960, 30 patients with rest and stress × 16 AHA segments) (Fig. 4, left) with the bias being 2.6% of the mean MBF value. There was a strong correlation between the MBF values automatically and manually processed with a slope (with no intercept) on a per-segment basis of 0.93 with an R^2 of 0.76 (Fig. 4, right). The ICC was 0.89, 95% confidence interval [0.87, 0.90].

Discussion

In this work we introduced an automated, deep-learning-based preprocessing pipeline for the quantification of myocardial perfusion MRI. The deep learning pipeline processes an image series in a few seconds, compared to roughly 5 minutes for a manual operator, allowing the full quantitative analysis to be performed automatically in just a few minutes. Each step of the pipeline was validated independently, with good results reported. The accuracy of the segmentation was comparable to the interobserver agreement and the quantitative analysis performed with the fully automated pipeline yielded MBF values that were in line with those computed with the manual interaction at each step. The fully automated pipeline was also successful in each image series (180/180) in our test set, indicating the robustness of this approach. As demonstrated by the similarity of the quantitative perfusion values obtained with both the automated and manual pipelines, the pipeline is not sensitive to the errors seen in detecting the peak LV enhancement frame, bounding box, and RV insertion points or segmenting the myocardium.

Despite the increased challenges posed by first-pass perfusion images, the average (SD) DSC reported is in a similar range to that reported for the segmentation in a comparable automated pipeline for T_1 mapping (0.80 [0.06] vs. 0.85 [0.07]).[25] It is also similar to the performance of the model Bai et al[24] developed when applied to a clinical dataset including diseased patients.

There has been previous work reporting fully-automated solutions for myocardial perfusion quantification.[7,8] However, neither of these solutions at present provide a myocardial segmentation, which is the most time-consuming manual task for the operator. The benefits of automatically segmenting the myocardium include reduced processing time in the quantification step, more interpretable parameter maps, and direct statistics for the ROI. The use of a myocardial segmentation has the potential to give a more objective diagnosis; for example, it allows the computation of the extent of perfusion defect as a percentage, which is a strong indicator of future events. Furthermore, fitting the model parameters in only the myocardium allows the use of spatial regularization[18,19] and the computation of the differences in perfusion between the endocardial and epicardial layers of the myocardium and perfusion dyssynchrony measures.[20,21]

A possible alternative pipeline could have involved the individual segmentation of each timeframe in the image series. In theory, this approach would not require an explicit motion correction step, as the segmentations for each timeframe could be matched to each other. It is the success of our recently validated motion correction scheme[27] that allows us to process just one timeframe. The benefits of this approach include that it is not necessary to design a scheme for matching points in different segmentations across different timeframes to extract voxelwise concentration curves. Moreover, it was significantly easier to gather high-quality training data, as an observer was only asked to segment the single frame at peak LV enhancement from each slice, reducing the manual work by a factor of 100. This is likely to be important for groups that want to reproduce the pipeline. It is also a significant consideration when acquiring more data to use transfer learning to adapt the pipeline to different acquisition parameters in the future. Our approach is also likely to be more robust, as we have chosen only the timeframe with the highest SNR and contrast to process. The segmentation of all timeframes would also include precontrast frames where there is very little signal in the myocardium to guide the segmentation.

A further strength of this work is that it used a representative clinical dataset for training, including a significant proportion of diseased patients, so by default should be applicable in the clinic on data acquired using similar methods. Transfer learning techniques have already been shown to be able to account for differences in the input domain and we envisage a future application to extend the pipeline to data acquired from different types of scanners at different centers.[24,25]

In our study, the size of the dataset available was limited. In order to negate this problem, data augmentation was employed. Online data augmentation was used with random transformations added to the data before each iteration of training. This helps the network to generalize better and to learn a more robust representation of the myocardium. However, this only addresses the lack of training data; it would be beneficial to further test the method on a larger dataset. A further limitation is that the primary endpoint of the analysis,

the quantitative perfusion values, does not have a ground-truth available for validation and that we have only shown that the quantitative values that are similar to those achieved manually by an expert operator. This does not investigate the diagnostic accuracy of these quantitative values, and thus further work to establish the diagnostic accuracy of the automated pipeline is warranted.

In conclusion, we proposed a fast and automated method for processing myocardial perfusion MR images prior to quantitative analysis. This automates the time-consuming and subjective processing tasks, such as myocardial segmentation, and performs on a par with the manual experts. We anticipate that this will lead to increased adoption of quantitative perfusion analysis in the clinic as well as opening up new possibilities for research in the field.

Conflict of Interest

M.B. is an employee of Philips Healthcare.

References

1. Schwitter J, Wacker CM, Wilke N, et al. Superior diagnostic performance of perfusion-cardiovascular magnetic resonance versus SPECT to detect coronary artery disease: The secondary endpoints of the multicenter multivendor MR-IMPACT II (Magnetic Resonance Imaging for Myocardial Perfusion Assessment). J Cardiovasc Magn Reson 2012; 14:1–10.
2. Nagel E, Greenwood JP, McCann GP, et al. Magnetic resonance perfusion or fractional flow reserve in coronary disease. N Engl J Med 2019 [Epub ahead of print].
3. Montalescot G, Sechtem U, Achenbach S, et al. 2013 ESC guidelines on the management of stable coronary artery disease. Eur Heart J 2013;34:2949–3003.
4. Windecker S, Kolh P, Alfonso F, et al. 2014 ESC/EACTS guidelines on myocardial revascularization. Eur Heart J 2014;35:2541–2619.
5. Villa ADM, Corsinovi L, Ntalas I, et al. Importance of operator training and rest perfusion on the diagnostic accuracy of stress perfusion cardiovascular magnetic resonance. J Cardiovasc Magn Reson 2018; 20:74.
6. Jerosch-herold M. Quantification of myocardial perfusion by cardiovascular magnetic resonance. J Cardiovasc Magn Reson 2010; 12:1–16.
7. Hsu L-Y, Jacobs M, Benovoy M, et al. Diagnostic performance of fully automated pixel-wise quantitative myocardial perfusion imaging by cardiovascular magnetic resonance. JACC Cardiovasc Imaging 2018:1–11.
8. Kellman P, Hansen MS, Nielles-Vallespin S, et al. Myocardial perfusion cardiovascular magnetic resonance: optimized dual sequence and reconstruction for quantification. J Cardiovasc Magn Reson 2017;19:43.
9. Jerosch-Herold M, Wilke N, Stillman AE, Wilson RF. Magnetic resonance quantification of the myocardial perfusion reserve with a Fermi function model for constrained deconvolution. Med Phys 1998;25: 73–84.
10. Morton G, Chiribiri A, Ishida M, et al. Quantification of absolute myocardial perfusion in patients with coronary artery disease. J Am Coll Cardiol 2012;60:1546–1555.
11. Miller CA, Naish JH, Ainslie MP, et al. Voxel-wise quantification of myocardial blood flow with cardiovascular magnetic resonance: Effect of variations in methodology and validation with positron emission tomography. J Cardiovasc Magn Reson 2014;16:1–15.
12. Engblom H, Xue H, Akil S, et al. Fully quantitative cardiovascular magnetic resonance myocardial perfusion ready for clinical use: A comparison between cardiovascular magnetic resonance imaging and positron emission tomography. J Cardiovasc Magn Reson 2017;19:1–9.
13. Bettencourt N, Chiribiri A, Schuster A, et al. Cardiac magnetic resonance myocardial perfusion imaging for detection of functionally significant obstructive coronary artery disease: A prospective study. Int J Cardiol 2013;168:765–773.
14. Hsu LY, Groves DW, Aletras AH, Kellman P, Arai AE. A quantitative pixel-wise measurement of myocardial blood flow by contrast-enhanced first-pass CMR perfusion imaging: Microsphere validation in dogs and feasibility study in humans. JACC Cardiovasc Imaging 2012; 5:154–166.
15. Schuster A, Sinclair M, Zarinabad N, et al. A quantitative high resolution voxel-wise assessment of myocardial blood flow from contrast-enhanced first-pass magnetic resonance perfusion imaging: Microsphere validation in a magnetic resonance compatible free beating explanted pig heart model. Eur Heart J Cardiovasc Imaging 2015;16:1082–1092.
16. Sammut EC, Villa ADM, Di Giovine G, et al. Prognostic value of quantitative stress perfusion cardiac magnetic resonance. JACC Cardiovasc Imaging 2017.
17. Sammut E, Zarinabad N, Vianello PF, Chiribiri A. Quantitative assessment of perfusion — Where are we now? Curr Cardiovasc Imaging Rep 2014;7:1–11.
18. Lehnert J, Wübbeler G, Kolbitsch C, et al. Pixel-wise quantification of myocardial perfusion using spatial Tikhonov regularization. Phys. Med. Biol. 2018;63:215017.
19. Scannell CM, Chiribiri A, Villa ADM, Breeuwer M, Lee J. Hierarchical Bayesian myocardial perfusion quantification. arXiv Prepr arXiv1906.02540 2019.
20. Hautvast GLTF, Chiribiri A, Lockie T, Breeuwer M, Nagel E, Plein S. Quantitative analysis of transmural gradients in myocardial perfusion magnetic resonance images. Magn Reson Med 2011;66:1477–1487.
21. Chiribiri A, Villa ADM, Sammut E, Breeuwer M, Nagel E. Perfusion dyssynchrony analysis. Eur Heart J Cardiovasc Imaging 2016;17: 1414–1423.
22. Cerqueira MD, Weissman NJ, Dilsizian V, et al. Standardized myocardial segmentation and nomenclature for tomographic imaging of the heart. A statement for healthcare professionals from the Cardiac Imaging Committee of the Council on Clinical Cardiology of the American Heart Association. Circulation 2002;105:539–542.
23. Litjens G, Kooi T, Bejnordi BE, et al. A survey on deep learning in medical image analysis. Med Image Anal 2017;42:60–88.
24. Bai W, Sinclair M, Tarroni G, et al. Automated cardiovascular magnetic resonance image analysis with fully convolutional networks. J Cardiovasc Magn Reson 2018;20:1–12.
25. Fahmy AS, El-Rewaidy H, Nezafat M, Nakamori S, Nezafat R. Automated analysis of cardiovascular magnetic resonance myocardial native T1 mapping images using fully convolutional neural networks. J Cardiovasc Magn Reson 2018;in-press:1–12.
26. Ishida M, Schuster A, Morton G, et al. Development of a universal dual-bolus injection scheme for the quantitative assessment of myocardial perfusion cardiovascular magnetic resonance. J Cardiovasc Magn Reson 2011;13:28.
27. Scannell CM, Villa ADM, Lee J, Breeuwer M, Chiribiri A. Robust nonrigid motion compensation of free-breathing myocardial perfusion MRI data. IEEE Trans Med Imaging 2019;38:1812–1820.
28. Plein S, Schulz-Menger J, Almeida A, et al. Training and accreditation in cardiovascular magnetic resonance in Europe: A position statement of the working group on cardiovascular magnetic resonance of the European Society of Cardiology. Eur Heart J 2011;32:793–798.
29. Kingma DP, Ba J. Adam: A method for stochastic optimization. In: *Proc 3rd Int Conf Learn Represent*; 2014.
30. Krizhevsky A, Sutskever I, Hinton GE. ImageNet classification with deep convolutional neural networks. In: *Proc 25th Int Conf Neural*

Inform Process Syst, Vol. 1. NIPS'12. USA: Curran Associates; 2012. p 1097–1105.

31. Xu Z, Huang Q, Park J, et al. *Supervised action classifier: Approaching landmark detection as image partitioning. Cham*, Switzerland: Springer; 2017. p 338–346.

32. Ren S, He K, Girshick R, Sun J. Faster R-CNN: Towards real-time object detection with region proposal networks. arXiv Prepr arXiv1506.01497 2015.

33. Ronneberger O, Fischer P, Brox T. U-Net: Convolutional networks for biomedical image segmentation. In: *Medical Image Computing and Computer-Assisted Intervention*. Munich: Elsevier; 2015. p. 234–241.

34. Zou KH, Warfield SK, Bharatha A, et al. Statistical validation of image segmentation quality based on a spatial overlap index. Acad Radiol 2004;11:178–189.

35. Noothout JMH, de Vos BD, Wolterink JM, Leiner T, Išgum I. CNN-based landmark detection in cardiac CTA scans. arXiv Prepr arXiv1804.04963 2018:1–11.

36. Broadbent DA, Biglands JD, Larghat A, et al. Myocardial blood flow at rest and stress measured with dynamic contrast-enhanced MRI: Comparison of a distributed parameter model with a fermi function model. Magn Reson Med 2013;70:1591–1597.

5.3 Supplementary material

	N = 175
Male gender	136 (78%)
Age (years)	64.3 $\pm$ 10.3
Hypertension	86 (49%)
Diabetes	34 (19%)
Hypercholesterolemia	78 (45%)
Current / previous smoker	24 (14%) / 18 (10%)
CAD status (visual assessment)	-
- 1 vessel	43 (25%)
- 2 vessels	28 (16%)
- 3 vessels	31 (18%)

Table 5.1 Demographic characteristics of the population.

Layer	Input size	Convolutional kernel	Number of filters
1	256 x 256	3 x 3	8
2	128 x 128	3 x 3	16
3	64 x 64	3 x 3	32
4	32 x 32	3 x 3	64
FC 1	8192	-	-
FC 2	512	-	-

Table 5.2 The architecture used for the peak LV enhancement frame detection and bounding box detection. FC 1 and FC 2 are the fully connected layers. Each convolutional layer involves convolutional with the filter with a stride length of 2 followed by batch normalisation and ReLU activation. Max-pooling is performed after every convolutional layer.

Layer	Input size	Convolutional kernel	Number of filters
1-3	96 x 96	3 x 3	16
4-6	48 x 48	3 x 3	32
6-9	24 x 24	3 x 3	64
9-12	12 x 12	3 x 3	128
12-15	6 x 6	3 x 3	256
15-18	12 x 12	3 x 3	128
18-21	24 x 24	3 x 3	64
21-24	48 x 48	3 x 3	32
24-27	96 x 96	3 x 3	16

Table 5.3 The U-Net architecture used for the myocardial segmentation and the RV insertion point detection. On the downward trajectory (layers 1-12) each layer involves convolutional with the filter with a stride length of 2 followed by batch normalisation and ReLU activation. Max-pooling is performed after every third convolutional layer to down-sample the image dimensions. On the upward trajectory (layers 16-27), each layer still involves convolutional with the filter with a stride length of 2 followed by batch normalisation and ReLU activation with transposed convolutions being performed before every third layer to up-sample the image dimensions. Features are concatenated across the layers of the same scale, as previously described.

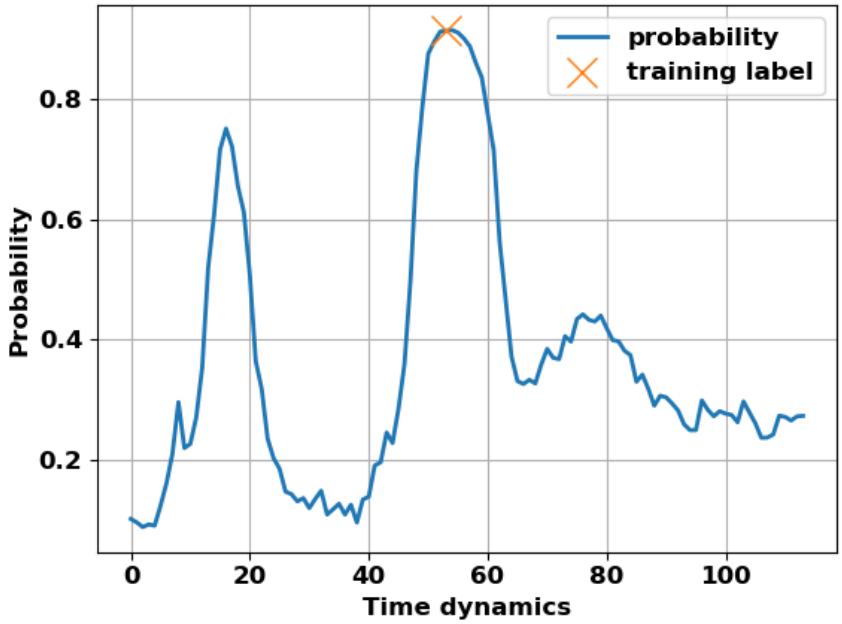

Fig. 5.5 The probability of being the peak LV enhancement frame over time. An increased probability is seen as contrast arrives in the LV, reaching a peak with the peak signal frame (marked with an X) and then reducing as the contrast washes out. The network also assigns relatively high probabilities to the time frames corresponding to the pre-bolus injection.

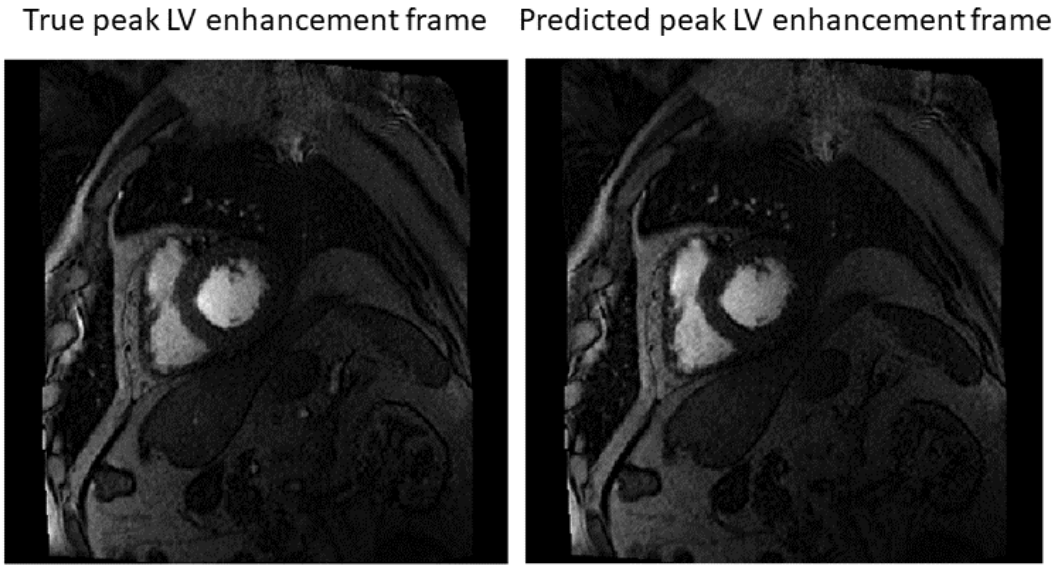

Fig. 5.6 A comparison of the automated and manually chosen peak LV enhancement time frame for the patient with the largest error (3 beats) in the test set. The 2 frames are virtually indistinguishable on visual assessment.

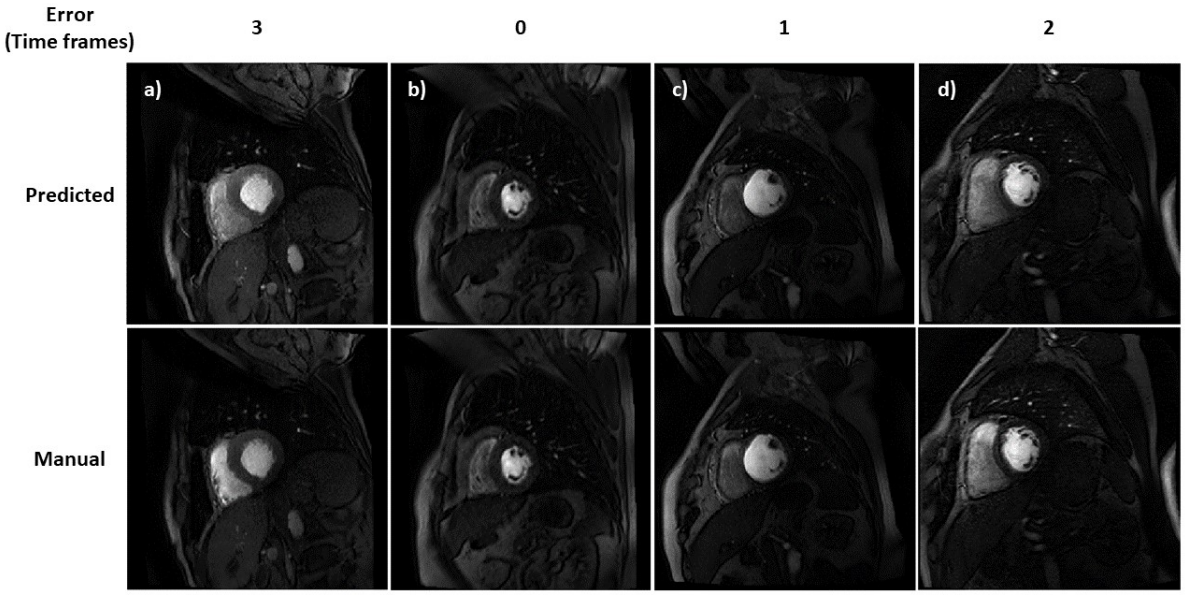

Fig. 5.7 A comparison of the automated and manually chosen peak LV enhancement time frame from a representative set of patients from the test set. The error is in terms of the number of time frames.

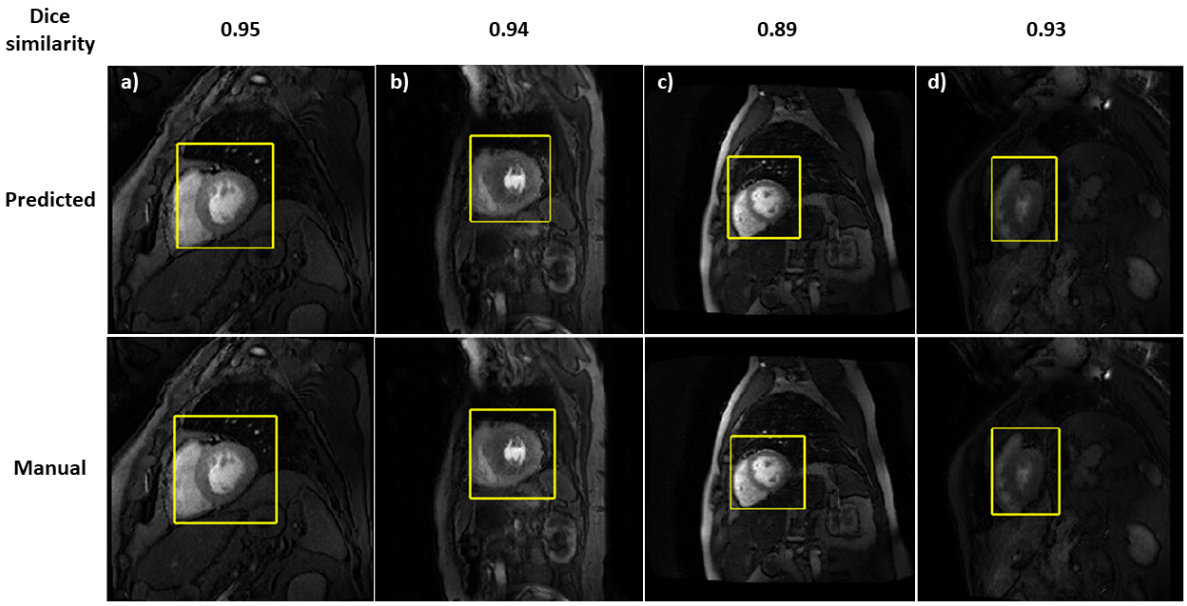

Fig. 5.8 A representative set of patients from the test set with a comparison between the automatically and manually determined bounding boxes.

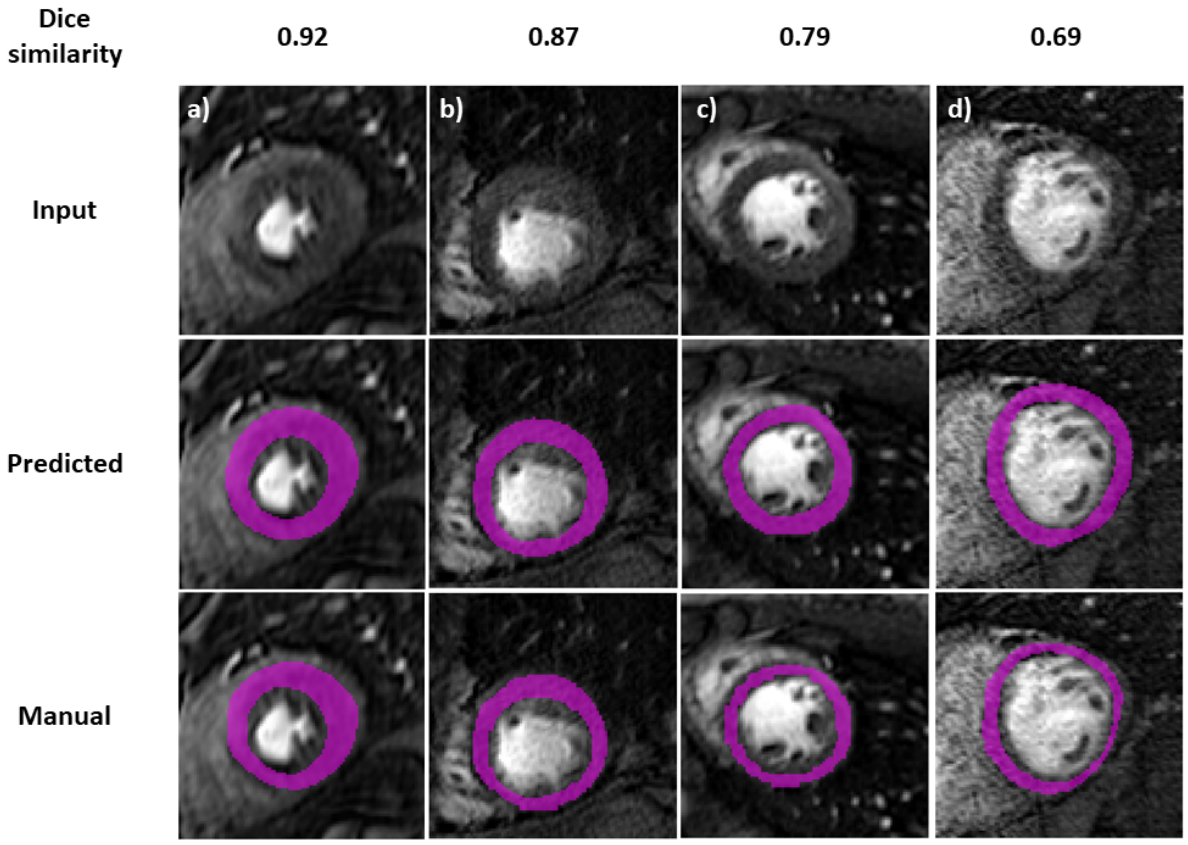

Fig. 5.9 A representative set of patients from the test set with a comparison between the automated segmentation and the manually defined segmentations.

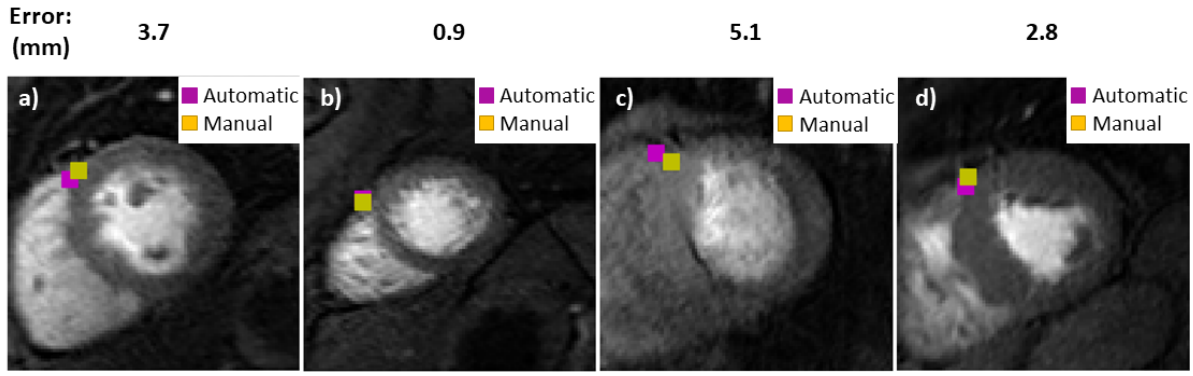

Fig. 5.10 A representative set of patients from the test set with a comparison between the automatically detected RV insertion point and the manually defined RV insertion point (error is in mm).

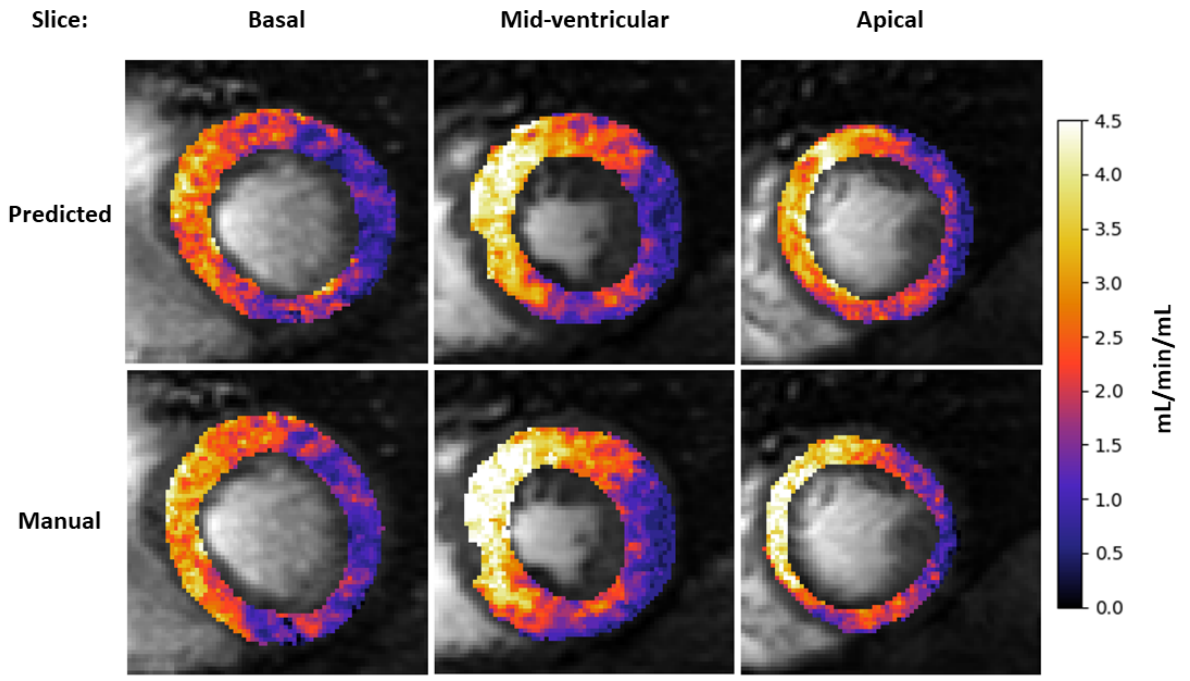

Fig. 5.11 A representative patient from the test set with a comparison between the automatically processed quantitative perfusion maps and the manually processed quantitative perfusion maps. Coronary angiography showed the patient has CAD with a lesion in the proximal left circumflex coronary artery.

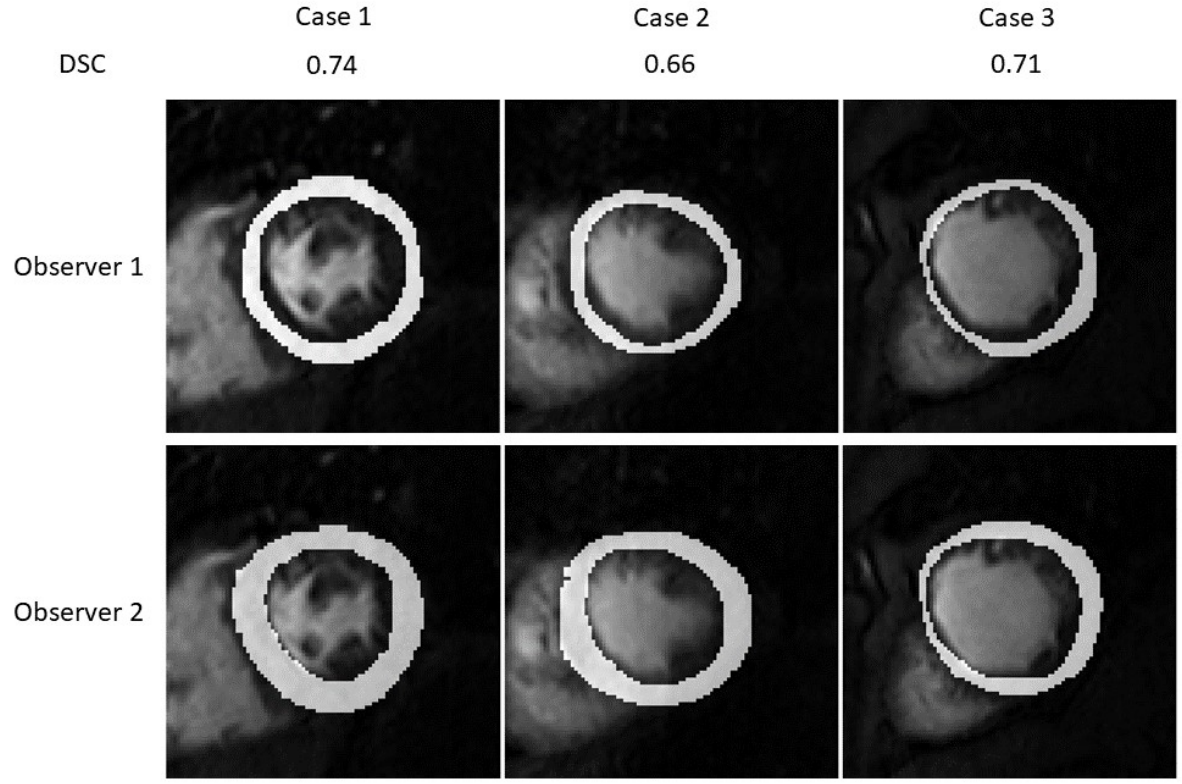

Fig. 5.12 A comparison between the manual segmentations obtained from two different observers.

Chapter 6

Hierarchical Bayesian myocardial perfusion quantification

6.1 Preface

As discussed in Section 3.3.2, the quantification of myocardial perfusion is an inverse problem. Given an observed AIF and myocardial tissue curve, the problem is to find the kinetic parameters such that the model best matches the observed data.

The question of whether or not the parameters are recoverable from the data is known as identifiablity. Romain et al. [100] showed that tracer-kinetic models of the form considered in this thesis are structurally identifiable. This is a strictly theoretical proof that states that the parameters are exactly recoverable in ideal, noise-free, infinite temporal resolution case because the mapping from the parameters to the residue function is a bijection.

The more pressing concern for the use of such models in real-world settings is the practical identifiablity. Practical identifiablity assesses the feasibility of recovering the correct parameters given the limited, imperfect measurements available. This has long been called into question for myocardial perfusion modelling and DCE-MRI in general. In 2002, Buckley [6] reported on the vast amount of possible parameter combinations that are indistinguishable at the noise level present in the data: "the issue of parameter uniqueness is further complicated by the surfeit of possible parameter combinations" and remarked that this introduces significant uncertainty in the estimates. This uncertainty has been similarly noted by an array of other authors [101–103] and specific to myocardial perfusion CMR, Likhite et al. [55] reported the same phenomenon: "A shortcoming with complex pharmacokinetic models is that identical tissue curves can be generated using a single arterial input function and multiple sets of perfusion model parameters".

However, it is of course possible to get the correct parameters, as is evidenced by the many successful studies conducted in the field [37, 80, 32, 81, 33]. It is a question of the trade-off between the amount of information in the data and the complexity of the model to be estimated. For example, the amount of information in the data can be increased by fitting the model on an AHA segment level rather than a pixel-wise level [37, 81]. On the other hand, the complexity of the model can be reduced by considering models with less parameters, for example, the Fermi model [32].

A relatively unexplored approach to increasing the amount of information available in the data is through the use of prior knowledge. This approach is investigated in this thesis, in a Bayesian inference framework.

6.1.1 Bayesian kinetic parameter estimation.

If we define $C_\theta(t) = F_p \cdot R(t;\theta) * C_{AIF}(t)$ to be the output of the tracer-kinetic model for a given set of parameters θ, T to be the total number of time points, and $\mathbf{y} = (y_1, y_2, \ldots, y_T)$ to be the observed myocardial concentrations at times $\mathbf{t} = (t_1, t_2, \ldots, t_T)$, then the standard non-linear least squares (NLLS) parameter estimate is given as:

$$\hat{\theta} = \arg\min_\theta \frac{1}{n} \sum_{i=1}^{T} (y_i - C_\theta(t_i))^2. \tag{6.1}$$

It can be seen that $\arg\min_x x = \arg\max_x \exp(-x)$ and since constant scaling factors do not affect the locations of minima or maxima, Equation 6.4 is equivalent to:

$$\hat{\theta} = \arg\max_\theta \frac{1}{(2\pi)^{n/2}\sigma^n} \exp\left(\frac{-\sum_{i=1}^{T}(y_i - C_\theta(t_i))^2}{2\sigma^2}\right) \tag{6.2}$$

$$= \arg\max_\theta \mathcal{N}(C_\theta(\mathbf{t}), \sigma^2). \tag{6.3}$$

where $\mathcal{N}(\mu, \sigma^2)$ is the Gaussian distribution with mean μ and variance σ^2. The term being maximised is known as the likelihood function, and is also written as $P(\mathbf{y}|\theta)$, this can be interpreted as the likelihood of observing the data that was observed, conditioned on the parameters. It is therefore seen that the NLLS solution is the maximum likelihood parameter estimate, under the assumption of Gaussian noise:

$$\hat{\theta} = \arg\max_\theta P(\mathbf{y}|\theta) \tag{6.4}$$

As previously discussed, the least squares solution can possess local optima and the global minima can be hard to find. This is a limitation as the method returns a single point estimate that must be assumed to be the true value. An alternative approach, Bayesian inference, is to assume that there is a distribution of possible parameter values and to try to compute this distribution. Bayes theorem allows the posterior distribution of the parameters to be written in terms of the likelihood function as:

$$P(\theta|\mathbf{y}) = \frac{P(\mathbf{y}|\theta) \cdot P(\theta)}{P(\mathbf{y})} \tag{6.5}$$

where $P(\theta)$ is the prior probability of the data and $p(\mathbf{y}) = \int_\theta P(\mathbf{y}|\theta) \cdot P(\theta) d\theta$ is the probability of the data. From the posterior distribution, the expected value of the parameters can be computed and also the standard deviation of the distribution gives a measure of the uncertainty of the parameter estimates. The difficultly is that the posterior distribution is not, in general, analytically tractable as it involves integrals which can not be computed and thus, numerical solutions must be considered.

6.1.2 Metropolis-Hastings

The Metropolis-Hastings algorithm is commonly used to numerically approximate posterior distributions. There are some definitions required to introduce the Metropolis-Hastings algorithm: a Markov chain is a random process, with discrete time steps, that has the Markov property. The Markov property states that the conditional probability of a future state of the random process depends only on the current state and not on any of the past states. The limiting distribution of a Markov chain is the distribution that it converges to asymptotically. Finally, a Monte Carlo method is simply a method that uses random samples to solve a problem.

Then, the Metropolis-Hastings algorithm is a Markov chain Monte Carlo (MCMC) method to approximate a distribution by simulating samples from it. It aims to construct a Markov chain with limiting distribution that is the distribution being approximated. It does this by taking a random walk through the distribution space, where the steps are proposed by a proposal distribution. If the posterior probability of the proposed position is greater than the posterior probability of the current position, the proposed step is accepted. If not, the proposed step can also be accepted with a probability proportional to the reduction in posterior probability it would cause. With the notation that samples θ are being sampled using a proposal distribution q from the target distribution $\pi(\cdot)$, the Metropolis-Hastings algorithm is given by Algorithm 2.

Algorithm 2: Metropolis-Hastings

Initialise : θ^0

for *iteration* $i = 1, 2, \ldots, N$ **do**
  $\theta^{cand} \sim q(\theta^i|\theta^{i-1})$;
  $\alpha = \min\{1, \frac{q(\theta^{i-1}|\theta^{cand})\pi(\theta^{cand}))}{q(\theta^{cand}|\theta^{i-1})\pi(\theta^{i-1})}\}$;
  $u \sim \text{Uniform}[0,1]$;
  if $u < \alpha$ **then**
    $\theta^i \leftarrow \theta^{cand}$;
  else
    $\theta^i \leftarrow \theta^{i-1}$;
  end
end

Output : $(\theta^0, \theta^1, \ldots, \theta^N)$

It is common to use a symmetric proposal distribution such that $q(a|b) = q(b|a)$ such that:

$$\frac{q(\theta^{i-1}|\theta^{cand})\pi(\theta^{cand}))}{q(\theta^{cand}|\theta^{i-1})\pi(\theta^{i-1})} = \frac{\pi(\theta^{cand}))}{\pi(\theta^{i-1})}. \tag{6.6}$$

It should also be noted that π is only required up to a constant scaling factor (as this would cancel in the numerator and denominator) so when approximating the posterior distribution for parameter inference, it is sufficient to use $P(\mathbf{y}|\theta) \cdot P(\theta)$ as:

$$P(\theta|\mathbf{y}) \propto P(\mathbf{y}|\theta) \cdot P(\theta). \tag{6.7}$$

Metropolis-Hastings is the approach used for the parameter inference in this thesis. However, there are more efficient sampling approaches being developed, such as Hamiltonian Monte Carlo sampling [104], which use gradient information to inform proposals, rather than random walks. This encourages movement towards areas of high probability and thus more efficient samples.

6.2 Journal article

The following text is reproduced as published [105]:

***Scannell, C.M.**, Chiribiri, A., Villa, A.D.M., Breeuwer, M. & Lee, J. Hierarchical Bayesian myocardial perfusion quantification. Med. Image Anal. 60, 101611 (2020).*

Medical Image Analysis 60 (2020) 101611

Contents lists available at ScienceDirect

Medical Image Analysis

journal homepage: www.elsevier.com/locate/media

Hierarchical Bayesian myocardial perfusion quantification

Cian M. Scannell[a,b,*], Amedeo Chiribiri[a], Adriana D.M. Villa[a], Marcel Breeuwer[c,d], Jack Lee[a]

[a] School of Biomedical Engineering and Imaging Sciences, King's College London, United Kingdom
[b] The Alan Turing Institute London, United Kingdom
[c] Philips Healthcare, Best, the Netherlands
[d] Department of Biomedical Engineering, Medical Image Analysis group, Eindhoven University of Technology, Eindhoven, the Netherlands

ARTICLE INFO

Article history:
Received 20 November 2018
Revised 7 November 2019
Accepted 8 November 2019
Available online 9 November 2019

Keywords:
Bayesian inference
Tracer-kinetic modelling
Myocardial perfusion MRI

ABSTRACT

Myocardial blood flow can be quantified from dynamic contrast-enhanced magnetic resonance (MR) images through the fitting of tracer-kinetic models to the observed imaging data. The use of multi-compartment exchange models is desirable as they are physiologically motivated and resolve directly for both blood flow and microvascular function. However, the parameter estimates obtained with such models can be unreliable. This is due to the complexity of the models relative to the observed data which is limited by the low signal-to-noise ratio, the temporal resolution, the length of the acquisitions and other complex imaging artefacts.

In this work, a Bayesian inference scheme is proposed which allows the reliable estimation of the parameters of the two-compartment exchange model from myocardial perfusion MR data. The Bayesian scheme allows the incorporation of prior knowledge on the physiological ranges of the model parameters and facilitates the use of the additional information that neighbouring voxels are likely to have similar kinetic parameter values. Hierarchical priors are used to avoid making *a priori* assumptions on the health of the patients. We provide both a theoretical introduction to Bayesian inference for tracer-kinetic modelling and specific implementation details for this application.

This approach is validated in both *in silico* and in vivo settings. *In silico*, there was a significant reduction in mean-squared error with the ground-truth parameters using Bayesian inference as compared to using the standard non-linear least squares fitting. When applied to patient data the Bayesian inference scheme returns parameter values that are in-line with those previously reported in the literature, as well as giving parameter maps that match the independant clinical diagnosis of those patients.

1. Introduction

Dynamic contrast-enhanced magnetic resonance imaging (DCE-MRI) can be used for the non-invasive assessment of myocardial perfusion (Chiribiri et al., 2009; Jaarsma et al., 2012; Nagel et al., 2003). According to recent clinical guidelines, it is indicated for the assessment of patients at risk of coronary artery disease (CAD) (Montalescot et al., 2013; Windecker et al., 2014) and has been extensively validated against the reference standard, fractional flow reserve (Li et al., 2014; Nagel et al., 2019). Currently, the clinical evaluation of such images is performed visually. The spatial and temporal distribution of contrast agent in the myocardium can identify myocardial ischaemia and provide insight into the presence and severity of stenoses. Some of the main limitations of this visual assessment are the difficulty of interpreting the images (Villa et al., 2018) and the underestimation of the ischaemic burden in patients with multivessel CAD (Patel et al., 2010). This has led to myocardial perfusion examinations only being routinely performed in highly experienced centres. Quantitative perfusion analysis has been proposed as a more reproducible and user-independant alternative to the visual assessment and has been shown to have a good diagnostic accuracy and prognostic value (Hsu et al., 2018; Knott et al., 2019; Sammut et al., 2017).

The quantification of myocardial perfusion from DCE-MRI data is achieved by applying tracer-kinetic models to track the passage of the contrast agent from the left ventricle (LV) to the myocardium to allow the inference of the kinetic model parameters, such as myocardial blood flow (MBF) (Broadbent et al., 2013;

* Corresponding author: School of Biomedical Engineering and Imaging Sciences, King's College London 4th Floor Lambeth Wing, St Thomas' Hospital, Westminster Bridge Road, London SW1 7EH 9, United Kingdom.
E-mail addresses: cian.scannell@kcl.ac.uk (C.M. Scannell), amedeo.chiribiri@kcl.ac.uk (A. Chiribiri), adriana.villa@kcl.ac.uk (A.D.M. Villa), marcel.breeuwer@philips.com (M. Breeuwer), jack.lee@kcl.ac.uk (J. Lee).

https://doi.org/10.1016/j.media.2019.101611

Hsu et al., 2018; Jerosch-Herold et al., 1998; Kellman et al., 2017; Wilke et al., 1997). However, there have been questions raised on the reliability of the quantitative parameters values that are estimated from DCE-MRI data due to the complexity of the models relative to the observed data (Buckley, 2002). This had led to the use of simplified models, such as the Fermi function (Jerosch-Herold et al., 1998; Wilke et al., 1997) or concentration curves that have been averaged over a region of the myocardium in order to boost the signal-to-noise ratio (SNR). To this end, a recent editorial by Axel (Axel, 2018) calls for improved quantitative methods, in particular more robust quantitative values in order to allow the clinical translation of the technique.

Larsson et al. (1996) showed that they could not reliably fit the five parameters needed for the tracer-kinetic modelling to the observed data, using least-squares fitting. As shown in the comparative study of Schwab et al. (2015), they were able to achieve reliable quantification with relatively simpler models, such as a Fermi-constrained deconvolution, but not with the multi-compartment exchange models. Broadbent et al. (2013) report failed fitting in 10% of cases (despite using concentration curves that have been averaged over a segment of the myocardium) and Likhite et al. (2017) also reported failed fittings to simulated data even though this is simplistic with respect to the patient data.

Some of the reasons behind the reported difficulties in the model fitting include that such parameter estimation, or non-linear regression, problems are known to get stuck in local optima (Dikaios et al., 2017; Kelm et al., 2009). As a result, even though the model-based concentration curves may well match the observed data, the reported parameters may be far from the true values. It has further been shown that the model parameters are correlated (Romain et al., 2017) and thus there are multiple distinct combinations of parameters that give outputs that are indistinguishable at the observed noise level. Also, as is typical with non-linear optimisations, the parameter estimates are highly sensitive to the initial conditions of the optimisation and the specific noise present in the data. A further limitation is that this non-linear least-squares fitting does not explicitly deal with the uncertainty in the estimated kinetic parameters.

In conclusion, there is need for an improved methodology to allow robust and reproducible estimation of the kinetic model parameters including, but not limited to, MBF. In this work, we develop and evaluate a framework to robustly infer the kinetic model parameters from the observed imaging data based on hierarchical Bayesian probabilistic modelling. This approach has been successfully employed in many similar applications, such as population dynamics in ecology (Rosenbaum et al., 2019). The proposed method is validated using simulation phantoms where gold standard kinetic parameters are known and subsequently further testing on clinical data is reported.

2. Background

2.1. Tracer-kinetic models

The tracer-kinetic models as presented in the literature (Ingrisch and Sourbron, 2013; Sourbron and Buckley, 2013) model the perfusion unit (a single voxel or segment) as a system with two interacting compartments - the plasma and the interstitium. These models give a pair of coupled differential equations which describe the evolution of the contrast agent as a non-linear function of physiological parameters, such as MBF. In this work, the tracer-kinetic model analysis was performed by fitting a two-compartment exchange model (2CXM) (Jerosch-herold, 2010; Sourbron and Buckley, 2013) to the observed concentration curves

$$v_p \frac{dC_p(t)}{dt} = \frac{F_b}{1-Hct}(C_{AIF}(t) - C_p(t)) + PS\ (C_e(t) - C_p(t)) \quad (1)$$

$$v_e \frac{dC_e(t)}{dt} = PS\ (C_p(t) - C_e(t)). \quad (2)$$

In (1) and (2), $C_p(t)$ and $C_e(t)$ are the concentration of contrast agent in the plasma and interstitial space at time t, respectively (in units of M). $C_{AIF}(t)$, the arterial input function (AIF), is the assumed input to the system that is being modelled (also in units of M). In myocardial perfusion quantification this is sampled from the LV. F_b is the MBF (mL/min/mL), v_p is the fractional plasma volume (dimensionless), v_e is the fractional interstitial volume (dimensionless) and PS is the permeability-surface area product (mL/min/mL). Hct is the haematocrit value (dimensionless).

This model has the benefit over other simpler models in that it resolves directly for MBF. The simpler models, such as those presented by Tofts and Kermode (1991), only allow the estimation of the K^{trans} parameter which can be influenced by either MBF or the extraction fraction. The Fermi function (Jerosch-Herold et al., 1998; Wilke et al., 1997) does resolve for MBF but not other kinetic parameters and the model is not physiologically motivated.

The solution to this system is then given as:

$$C_{\mathbf{\Theta}}(t) = R_F(t, \mathbf{\Theta}) * C_{AIF}(t - \tau_0) \quad (3)$$

with the analytic form of the residue function R_F presented in the appendix. $\mathbf{\Theta} = (\mathrm{F_p}, \mathrm{v_p}, \mathrm{v_e}, \mathrm{PS})^{\mathrm{T}}$ and τ_0 is the time delay term which accounts for the fact that the contrast agent does not move instantaneously from the left ventricle to the myocardial tissue. This is an unknown parameter that must also be estimated. The concentration that is observed in the MRI experiment is the contribution from both compartments and is given as: $C(t) = v_p \cdot C_p(t) + v_e \cdot C_e(t)$.

2.2. Non-linear regression

The standard technique to estimate the model parameters uses a least-squares method. Given the observed contrast agent concentrations $\boldsymbol{y} = (y(t_0), y(t_1), \ldots, y(t_{N-1}))^T$, it is assumed that: $y(t_j) = C_{\mathbf{\Theta}}(t_j) + \epsilon_j$ where ϵ_j are the error terms and comprise of both noise and other sources of error, such as motion. The estimation of the parameters is then to find the $\mathbf{\Theta}$ which minimises the sum of squared errors cost function χ^2:

$$\hat{\mathbf{\Theta}} = \ argmin_{\mathbf{\Theta}} \chi^2(\mathbf{\Theta}) = \ argmin_{\mathbf{\Theta}} \frac{1}{N} \sum_{j=0}^{N-1} \left(C_{\mathbf{\Theta}}(t_j) - y(t_j)\right)^2 \quad (4)$$

Under the assumption that the error terms come from independant and identically distributed Gaussian distribution this is equivalent to the maximum likelihood estimate as it maximises the likelihood function $p(\mathbf{y}|\mathbf{\Theta})$.

As previously discussed, this technique can break down in the case where the cost function has multiple local minima. That is, there are multiple values of $\mathbf{\Theta}$ that produce similar model output. If this is the case, the values of the parameters estimated may depend strongly on the initial conditions of the optimisation and be far from the true values. Furthermore, in vivo, the time delay parameter τ_0 can introduce further local minima.

An example of such a cost function is shown in Fig. 1. It is seen that when noise is added, two local optima emerge, neither of which corresponds to the true parameter values. The optimisation will converge to one of these depending on its initial conditions. In other cases it is possible for the cost functions to possess long flat valleys where optimisation may stop due to the update being less than the required tolerance leading to unreliable param-

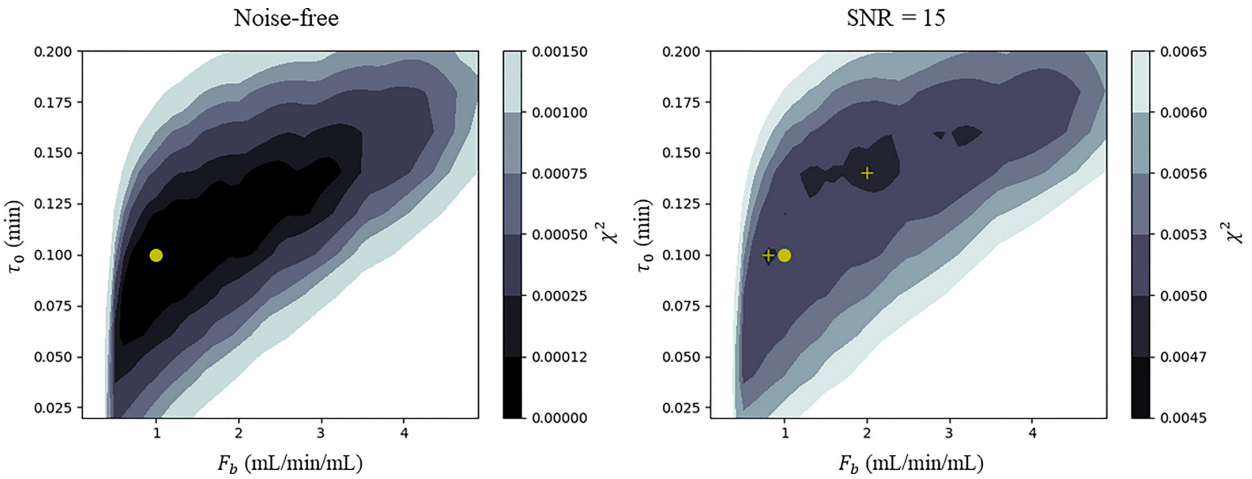

Fig. 1. An example of a cost function created using simulated data, on the left in the noise-free case and on the right with a SNR of 15. This image is constructed by taking the minimum intensity projection over the three parameters v_p, v_e and PS to allow the visualisation of the 5-dimensional surface as a function of F_b and τ_0. The true parameter values used in the forward simulation are $F_b = 1.0$, $v_p = 0.08$, $v_e = 0.16$, $PS = 0.4$, $\tau_0 = 0.1$. In the noise-free (left) case the cost function has a global minimum which corresponds to the true parameter values (yellow dot). In the presence of noise (right) it is seen that there are two local optima, neither of which corresponds to the true parameter values. The optimisation will converge to one of these depending on its initial conditions. The yellow circle is the position of the true minimum of the cost function and the two cross symbols are the positions of the two local minima.

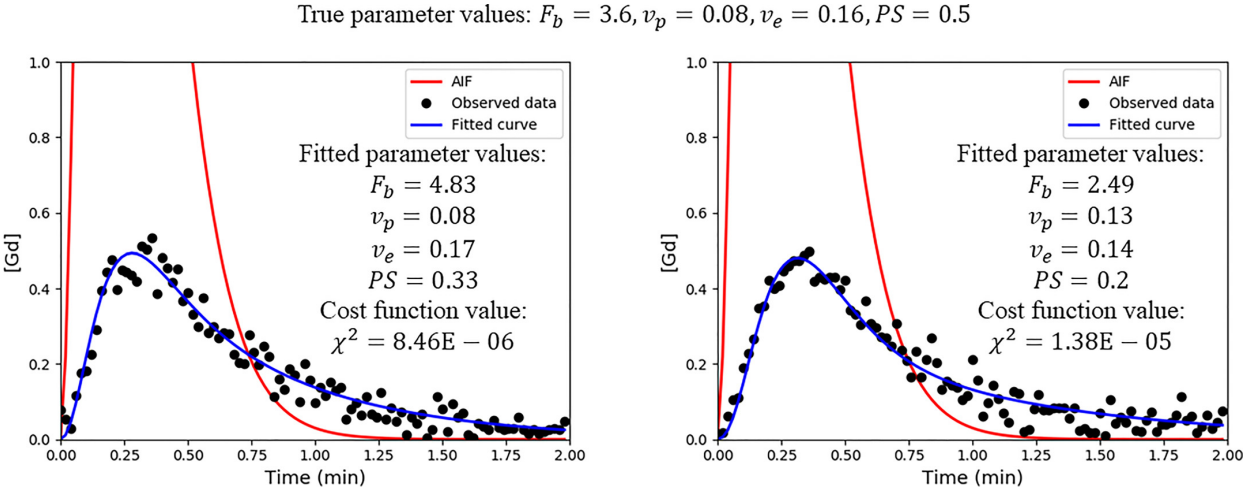

Fig. 2. For the same arterial input function AIF (red curves) and the same ground-truth parameters ($F_b = 3.6$, $v_p = 0.08$, $v_e = 0.16$, $PS = 0.5$) the two blue curves are simulated. Their only difference being the Rician noise realisation. A comparison of the two fits shows a difference of a factor of two in the computed MBF. This could vastly change the patients' diagnosis.

eter estimates. This cost function was constructed using simulated data and can possess further local optima due to the complex errors and physiology seen in patient data. Additionally, as shown by Sommer and Schmid (2014), the analytic form of the residue function R_F, which is the sum of two exponentially decaying components, can lead to an identifiability problem when the two exponents are too similar or when the contribution of one compartment vanishes which can further reduce the reliability of the parameter estimates.

Fig. 2 shows two myocardial tissue curves that have been simulated using the same parameters, with the only difference being the realisation of the Rician noise that is added. This could be interpreted as being two curves from neighbouring voxels with the same underlying physiology. In this example it is seen how the traditional non-linear regression algorithms can yield vastly different fits, with the two fitted MBF values (F_b) being different by a factor of two despite being simulated with the same kinetic parameters.

2.3. Bayesian parameter estimation

The aforementioned maximum-likelihood approach assumes that there is one true value of the parameter and computes a point estimate of this. Conversely, Bayesian estimation treats the parameters as random variables and approximates their posterior distribution. This hence allows computation of the expected value of the parameter. The variance of the distribution also allows an expression of confidence in the value of the parameter estimate.

It is assumed that the observed data $y(t_j)$ at each time point t_j, $j = 0, \ldots, N-1$ comes from the model with some Gaussian error with variance σ_j^2 such that: $y(t_j) \sim \mathcal{N}(C_{\boldsymbol{\Theta}}(t_j), \sigma_j^2)$. To then examine the model parameters given observed data, the posterior distribution $p(\boldsymbol{\Theta}|\boldsymbol{y})$ is required. The posterior distribution can be obtained through the application of Bayes' theorem

$$p(\boldsymbol{\Theta}|\boldsymbol{y}) = \frac{p(\mathbf{y}|\boldsymbol{\Theta}) \cdot p(\boldsymbol{\Theta})}{\int_{\boldsymbol{\Theta}} p(\mathbf{y}|\boldsymbol{\Theta}) \cdot p(\boldsymbol{\Theta}) d\boldsymbol{\Theta}} \propto p(\mathbf{y}|\boldsymbol{\Theta}) \cdot p(\boldsymbol{\Theta}). \quad (5)$$

The term $p(\boldsymbol{\Theta})$ is the prior probability of the parameters. It is common to assume that the parameters θ_i are independant and so $p(\boldsymbol{\Theta})$ is the product of the prior distributions over the individual parameters, θ_i.

In general, the posterior distribution is not analytically tractable and must be approximated using Markov chain Monte Carlo (MCMC) sampling. Through (5), it is possible to compute samples which are proportional to the posterior distribution and MCMC sampling utilises these samples to construct a Markov chain with a stationary distribution equal to the posterior distribution. It does this using a proposal distribution which is used to propose, randomly, how to move in parameter space and an acceptance rule which is used to decide whether to accept the proposed move or not, based on the information from the likelihood and the prior information. An introduction to the use of Bayesian modelling for non-linear regression problems is given in the book of Seber and Wild (1989).

2.3.1. Hierarchical Bayesian modelling

Quantitative myocardial perfusion MRI is a natural application for the use of hierarchical Bayesian modelling. In this modelling approach, the prior probability distribution is not governed by fixed hyperparameters but rather hyperparameters $\boldsymbol{\alpha}$ which are described by a further probability distribution, i.e. a hyperprior $p(\boldsymbol{\alpha})$. Hence, $\boldsymbol{\Theta}$ in (5) is now dependant on these hyperparameters and (5) becomes:

$$p(\boldsymbol{\Theta}, \boldsymbol{\alpha}|\boldsymbol{y}) \propto \; p(\boldsymbol{y}|\boldsymbol{\Theta}, \boldsymbol{\alpha}) \cdot p(\boldsymbol{\Theta}|\boldsymbol{\alpha}) \cdot p(\boldsymbol{\alpha}). \tag{6}$$

This approach is useful when the data is structured into distinct but not entirely unrelated groups. This is referred to as partial pooling, as opposed to complete pooling (use of one fixed prior distribution) or no pooling (use of different priors for each group). For example, in a stress perfusion MRI, these distinct groups could be healthy and diseased tissue. If the same prior knowledge was used for both groups, then it would lead to an averaging effect over these regions. Hierarchical modelling is thus an attractive compromise between treating the groups equivalently and having completely independant models.

2.3.2. Generalised Gaussian Markov random field prior

In addition to prior distributions on the kinetic parameters, it is possible to incorporate spatial prior knowledge. This enforces smoothness in the spatial domain and it motivated by the idea that neighbouring voxels should exhibit similar kinetic properties. In particular, in this application, a generalised Gaussian Markov random field prior is suitable. Mathematically, this is equivalent to putting prior distributions on the differences between parameters in neighbouring voxels that have zero mean:

$$\mathbf{p}(\boldsymbol{\Theta}_i|\boldsymbol{\Theta}_j, \nu_{i,j}) \propto \exp\left(-\frac{\nu_{i,j}}{2}\|\mathbf{W}\;(\boldsymbol{\Theta}_i - \boldsymbol{\Theta}_j)\|_p^p\right)\;, \text{ if } j \sim i \tag{7}$$

where $j \sim i$ if j and i are neighbouring voxels and $1 \leq p \leq 2$. Here, $\nu_{i,j}$ is the rate parameter (inverse of the scale parameter) of the distribution and $\mathbf{W}$ is the weighting coefficients. The use of $p = 1$ corresponds to the Laplace distribution and is known to have edge-preserving properties (Bardsley, 2012).

3. Methods

3.1. Simulation experiments

The proposed method was first tested using simulated image series as the parameter estimates can be compared to ground-truth values. The 6 by 6 voxel image series was created using ground truth tracer-kinetic parameter maps with values as expected in the myocardium under three different realistic conditions mimicking a healthy patient at rest, a healthy patient at stress and a patient with stress-inducible ischaemia (Broadbent et al., 2013). The parameter maps were used to forward simulate the model with a gamma-variate function used to generate a realistic AIF. The kinetic parameter values used in the simulation were $F_b = 3.5,\;\; \nu_p = 0.08, \nu_e = 0.16, PS = 1.0$ in healthy voxels at stress and $F_b = 1.0,\;\; \nu_p = 0.08, \nu_e = 0.16, PS = 1.0$ in healthy voxels at rest. The simulation phantom mimicking a patient with stress-inducible ischaemia was created using $F_b = 3.5,\;\; \nu_p = 0.08, \nu_e = 0.16, PS = 1.0$ with two disconnected regions with reduced MBF ($F_b = 1.0$) added to mimic regions of stress-inducible myocardial ischaemia. Rician noise was added to the image, with the level chosen to achieve a realistic SNR of 15 (Broadbent et al., 2016; Cheng et al., 2007). The SNR here was defined to be the ratio of the standard deviation of the noise realisation to the maximum of the tissue curves. The data curves were simulated with a realistic temporal resolution of $\Delta t = 0.012$ min, corresponding to a heart rate of roughly 83 beats per minute at stress and $\Delta t = 0.017$ min at rest, for a total time $T = 3$ min. The proposed parameter estimation method is compared in a Monte-Carlo study for $n = 20$ distinct noise realisations, for each simulation phantom, with a traditional, gradient-based optimisation scheme in order to assess the accuracy and the reproducibility of the parameter estimates. The normalised mean square error (NMSE) between the true and estimated kinetic parameters is reported and a Mann-Whitney U test is used to compare the distribution of the NMSE values from the Monte-Carlo study. A further assessment is conducted (also using the NMSE values) to compare the proposed hierarchical model to an equivalent non-hierarchical approach.

3.2. In vivo experiments

The technique was tested in eight patients suspected of having CAD referred for stress perfusion cardiac MRI at King's College London. Image acquisition was performed on a 3.0T scanner (Philips Achieva-TX, Philips Medical Systems) using standard acquisition protocols (Kramer et al., 2013). The typical acquisition parameters, TR/TE/flip angle/saturation prepulse delay were 2.5 ms/1.25 ms/15°/100 ms with a typical spatial resolution of $1.34 \times 1.34 \times 10$ mm. The dynamic image series were acquired during first-pass injection of 0.075 mmol/kg Gadobutrol (Gadovist, Schering, Germany) at 4 ml/s followed by a 20 ml saline flush. A dual bolus contrast agent scheme was used to correct for signal saturation of the AIF, as previously described (Ishida et al., 2011). Images were acquired under adenosine-induced stress. The images were acquired with a breath-hold during the passage of the main bolus, as is done clinically, and also retrospectively motion corrected using a previously validated scheme (Scannell et al., 2019).

As aforementioned, a dual-bolus acquisition is performed in order to mitigate the difficulties caused by the non-linear relationship between the concentration of contrast agent and the MRI signal intensities. It is hence assumed there is a linear relationship between the concentration of contrast agent and the signal intensity. The concentration of gadolinium (C(t)) was approximated from the signal intensities (S(t)) using an application specific version of the relative signal enhancement (Biglands et al., 2015; Ingrisch and Sourbron, 2013):

$$C(t) = \frac{1}{r_1 \cdot T_{1b}}\left(\frac{S(t) - S(0)}{S_{LV}(0)}\right) \tag{8}$$

with the T_{1b} of blood taken as 1736 ms and r_1 the contrast agent as 4.5 s^{-1} mmol/L^{-1} (Broadbent et al., 2016). S(0) is the average of the first five acquired images before the injection of contrast agent. Similarly, $S_{LV}(0)$ is the pre-contrast signal in the left ventricular blood pool.

In the case of this patient data, there are no ground-truth parameter values to compare to. Therefore, the purpose of this

study is to test whether the kinetic parameter values that are estimated can identify perfusion defects that match the independant visual assessment found in the clinical reports. This provides insight into the reliability of the fittings and the ability of the proposed method to deal with the more complex curves and error terms that are present in patient data. The number of failed fittings and outlier kinetic parameter estimates are further compared between implementations. All scans were reported blindly by experienced operators with level III CMR accreditation according to the guidelines of the Society for Cardiovascular Magnetic Resonance (SCMR). As per the expert assessment, four patients were classified as being positive for ischaemia and four were classified as not having obstructive coronary artery disease. In this work, stress scans only are considered as rest scans have been shown to not increase diagnostic accuracy (Biglands et al., 2018; Villa et al., 2018). The myocardium was contoured using the cvi[42] software (Circle Cardiovascular Imaging Inc., Calgary, Alberta, Canada) by an experienced operator with level III CMR accreditation (SCMR) and the segmentations were exported using the open-source code of Bai et al. (2018).

3.3. Non-linear regression implementation

All steps are implemented in Python, using the SciPy module for the optimisation (Jones et al., 2001). The nonlinear regression approach uses the L-BFGS (Zhu et al., 1997) nonlinear optimisation scheme with box constraints. Each parameter was constrained to be within conservative physiological limits and to conform with what has been previously found with tracer-kinetic models (Broadbent et al., 2013). The parameters are constrained such that: $0.001 \leq F_b \leq 6.0$, $0.001 \leq v_p \leq 0.3$, $0.001 \leq v_e \leq 0.4$ and $0.001 \leq PS \leq 4.0$. This fitting is repeated several times with different initial conditions randomly chosen from a uniform distribution on each of these ranges. One initialisation and 100 initialisations are used for comparison on the simulated data with 100 initialisations used on the patient data. The reported parameter estimates are then the successful fit which has achieved the lowest cost function value. This is done to reduce the effect of the choice of the initial conditions on the parameter estimate and to minimise the risk of converging to local optima (Dikaios et al., 2017; Romain et al., 2017). A fit is defined as successful if it achieves a tolerance of less than 10^{-8} within 1000 iterations and none of the resulting parameters achieve their upper or lower bounds. The AIF ($C_{AIF}(t)$) is extracted using independant component analysis (Jacobs et al., 2016) and the bolus arrival time is estimated using the method of Cheong et al. (2003).

3.4. Bayesian parameter estimation implementation

The Bayesian parameter estimate was implemented using an in-house software developed in Python. The posterior distribution for the parameters in voxel i is given through the application of Bayes' theorem as:

$$p\left(\boldsymbol{\Theta}^{\mathbf{i}}, \boldsymbol{\alpha}^{\mathbf{i}} | \mathbf{y}^{\boldsymbol{i}}\right) \propto \; p\left(\mathbf{y}^{\mathbf{i}} | \boldsymbol{\Theta}^{\mathbf{i}}, \boldsymbol{\alpha}^{\mathbf{i}}\right) \cdot p\left(\boldsymbol{\Theta}^{\mathbf{i}} | \boldsymbol{\alpha}^{\mathbf{i}}\right) \cdot p\left(\boldsymbol{\alpha}^{\mathbf{i}}\right) \tag{9}$$

It is assumed that the observed data in voxel i at time t_j is Gaussian distributed, i.e. that $y^i(t_j) \; \sim \mathcal{N}(C_{\boldsymbol{\Theta}^{\mathbf{i}}}(t_j), \sigma_i^2)$. This gives rise to the likelihood function:

$$p\left(\mathbf{y}^{\mathbf{i}} | \boldsymbol{\Theta}^{\mathbf{i}}, \boldsymbol{\alpha}^{\mathbf{i}}\right) = \left(2\pi\sigma_i^2\right)^{-\frac{N}{2}} \exp\left(-\frac{1}{2\sigma_i^2} \sum_{j=0}^{N-1} \left(y^i\left(t_j\right) - C_{\boldsymbol{\Theta}^{\mathbf{i}}}\left(t_j\right)\right)^2\right) \tag{10}$$

In this work, F_b (mL/min/mL) is selected to be Gaussian distributed with mean α_b and a fixed variance 0.2. PS (mL/min/mL) is Gaussian distributed with mean α_S and variance $0.1.\alpha_b$ is taken to be uniformly distributed on [0,7] and α_S is taken to be uniformly distributed on [0,5]. v_p (%/100) is assumed to be uniformly distributed on [0,0.4] and v_e (%/100) is assumed to be uniformly distributed on [0,0.5]. These were chosen to be in line with previously reported literature values (Broadbent et al., 2013) and physiological intuition. The priors are chosen to be weakly informative in that they encompass a much larger range of values than the values that have been found previously in the literature. Rather than expressing confidence about the parameters being close to a certain value, it acts as regularisation and restricts the parameter estimates to these ranges. The prior distribution on the observed error (in M) for voxel i (σ_i^2) is taken to be a flat Inverse-Gamma distribution, with shape parameter $c = 0.001$ and scale parameter $d = 0.001$, as is conventional.

A Laplace prior with location 0 and scale 0.1 is chosen on the absolute value of the distance between the kinetic parameter estimates of neighbouring voxels. The Laplace distribution is chosen due to its edge preserving properties. This gives rise to the prior distribution:

$$\begin{aligned}
p\left(\boldsymbol{\Theta}^{\mathbf{i}} | \boldsymbol{\alpha}^{\mathbf{i}}\right) = \; & p\left(F_b^i | \alpha_b^i\right) \cdot p\left(v_p^i\right) \cdot p\left(v_e^i\right) \cdot p\left(PS^i | \alpha_{PS}^i\right) \cdot p\left(\sigma_i^2\right) \\
& \times \; p(\boldsymbol{\Theta}^{\mathbf{i}} | \boldsymbol{\Theta}^{\mathbf{n(i)}}, \boldsymbol{\alpha}^{\mathbf{i}}, \; v_{i,j}) \\
& \propto \; \exp\left(-\frac{1}{2 \cdot 0.1}\left(F_b^i - \alpha_b^i\right)^2\right) \times \mathbb{I}\left(v_p^i \in (0, 0.3]\right) \\
& \times \mathbb{I}\left(v_e^i \in (0, 0.4]\right) \\
& \times \; \exp\left(-\frac{1}{2 \cdot 0.1}\left(PS^i - \alpha_{PS}^i\right)^2\right) \\
& \times \left(\frac{1}{\sigma_i^2}\right)^{c-1} \exp\left(-\frac{d}{\sigma_i^2}\right) \\
& \times \exp\left(-\frac{1}{0.2} \sum_{j \in n(i)} \sum_{k=1}^{4} \left(W_k \cdot \left|\Theta_k^{\mathrm{i}} - \Theta_k^{\mathrm{j}}\right|\right)\right)
\end{aligned} \tag{11}$$

$\mathbb{I}(X)$ is the indicator function on the set X which takes the value 1 on X and 0 otherwise. $n(i)$ is the set of neighbouring voxels of voxel i. A voxel's neighbours are those voxels in its surrounding 4-neighbourhood, above, below, to the left and to the right of it. Due to the shape of the myocardium, it is possible that a voxels neighbours are not in the myocardial segmentation. In such a case, a voxel diagonally above or below is taken or failing that, the closest voxel that is in the myocardium.

The difference between the parameter estimates in neighbouring voxels i and j is computed using a weighted sum. The weights, W_k are used to account for the different scales of the parameters, since otherwise, differences in the higher magnitude parameter values (F_b and PS) would have a dominating effect compared to the lower magnitude parameter values (v_p and v_e). The value of the weight for a given parameter W_k on a given iteration of the MCMC sampling is the inverse of the previous sample of the parameter. For the non-hierarchical model it is taken that $F_b \sim \mathcal{N}(X, 0.2)$ and $PS \sim \mathcal{N}(1.0, 0.2)$, where two values of X (3.5 and 1) have been used for comparison.

The hyperprior distribution is given as:

$$p\left(\boldsymbol{\alpha}^{\mathbf{i}}\right) = \; \mathbb{I}\left(\alpha_b^i \in [0.001, 7]\right) \times \mathbb{I}\left(\alpha_{PS}^i \in [0.001, 5]\right) \tag{12}$$

In this work, the Metropolis-Hasting algorithm with random walk proposals is used to sample from the posterior distribution. In short, the Metropolis-Hasting algorithm moves randomly through parameter space using a proposal distribution. The proposal distribution proposes a move in parameter space that is then accepted with a probability that is related to the change in posterior probability associated with the new sample. This leads to the construction of a Markov chain with a stationary distribution that approximates the posterior distribution.

In the work, the choice of the above distributions and their respective variances was made, empirically, to optimise the trade-off

Table 1
NMSE and Mann-Whitney U test results for the hierarchical Bayesian and non-linear least squares kinetic parameter estimates. The Mann-Whitney U test compares the estimates from the Bayesian inference to those achieved with non-linear least squares (100 initialisations).

Parameter	Bayesian	Non-linear least squares (1 initialisation)	Non-linear least squares (100 initialisations)	p-value (Mann-Whitney U test)
All	0.13 (0.2)	0.72 (0.74)	0.32 (0.55)	$p < 0.0001$
F_b	0.05 (0.09)	0.46 (0.44)	0.1 (0.09)	$p = 0.002$
v_p	0.22 (0.27)	0.27 (0.21)	0.35 (0.31)	$p = 0.02$
v_e	0.12 (0.16)	0.31 (0.19)	0.20 (0.17)	$p = 0.01$
PS	0.11 (0.21)	1.83 (0.5)	0.63 (0.96)	$p < 0.0001$

between thoroughly exploring parameter space and sticking to areas with high posterior probability. They were chosen in order to achieve a rate of acceptance of proposals close to 0.234 which has previously been shown to be optimal (Roberts et al., 1997). Markov chains of 4000 steps were constructed. In order to assess the stationary distribution of the chain, the initial 1000 steps were discarded, referred to as the burn-in phase. The number of steps was chosen to be far in excess of the number needed for convergence according to the $\hat{R}$ statistic (Gelman and Rubin, 1992). In order to create parameter maps, the median value of the posterior distribution are reported and to examine the uncertainty associated with such a parameter estimate, the coefficient of variation of the posterior distribution, the ratio of the standard deviation of the distribution to its mean value, is reported.

4. Results

4.1. Simulations

Table 1 shows the mean (standard deviation) NMSE between the estimated and true kinetic parameters values for both the hierarchical Bayesian and non-linear least squares implementations, with the results of the Mann-Whitney *U test*. The NMSE is significantly lower for the Bayesian method compared to the non-linear least squares. The NMSE is also significantly lower for the non-linear least squares with 100 initialisations as compared to one initialisation ($p < 0.0001$). Example parameter maps from both methods are compared to the true parameter maps in Fig. 3. A significantly higher NMSE was found in the stress simulations with a perfusion defect using the non-hierarchical approach (0.24 (0.15), $p < 0.001$). A comparison of the computed MBF parameter maps for an example noise realisation shown in Fig. 4.

4.2. Patient data

The median computed MBF value (25th percentile, 75th percentile) was 2.35 (1.9, 2.68) mL/min/mL under stress conditions using the proposed Bayesian inference scheme. The equivalent results were 2.37 (1.12, 3.01) mL/min/mL using the non-linear least squares fitting. However, with the least squares fitting approach there is a number of voxels for which the fitting fails completely, which are represented as holes in the parameter maps, as seen in Fig. 5. The proposed Bayesian inference technique has zero voxels with estimates converging to upper or lower bounds or outside

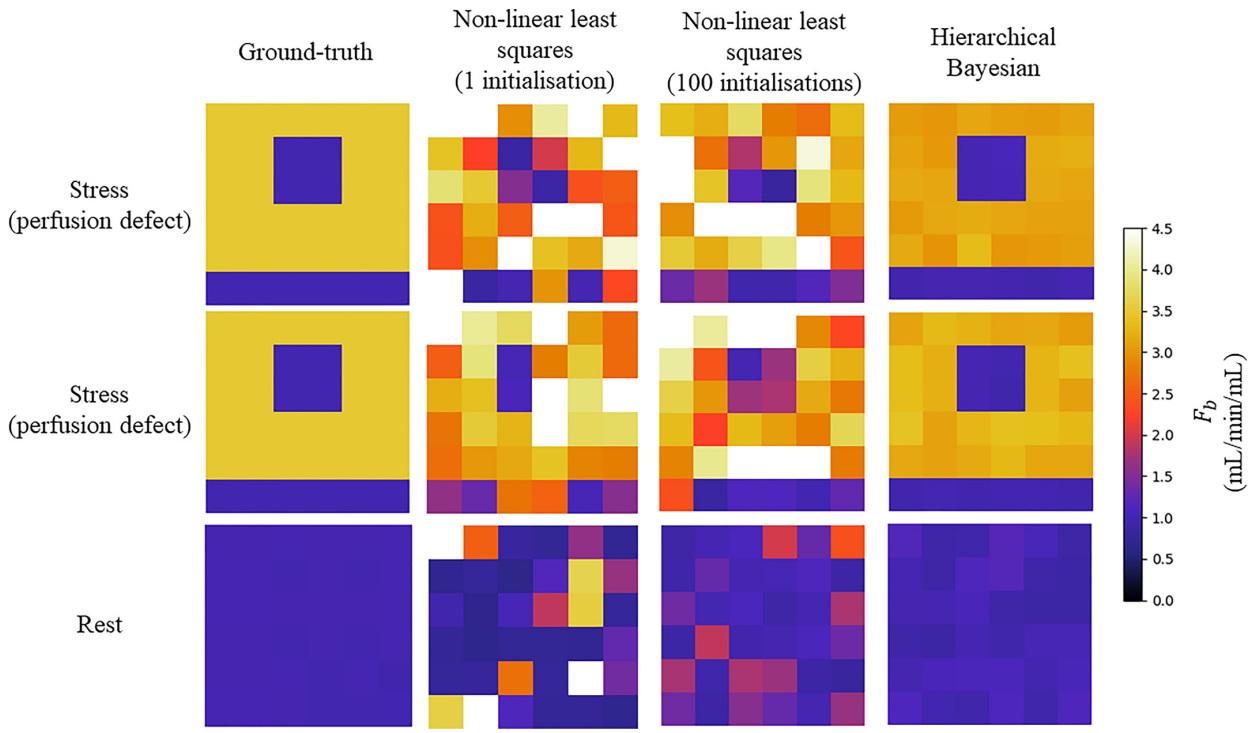

Fig. 3. The ground-truth F_b parameter values (left) are compared to values that are estimated using non-linear least-squares fitting with one initialisation (middle left), 100 initialisations (middle right), and the proposed Bayesian inference method (right) for two random noise realisations of the simulations mimicking stress-inducible ischaemia (top and middle) and one random noise realisation of the rest simulations (bottom). The Bayesian inference is significantly closer to the ground-truth with fewer outliers.

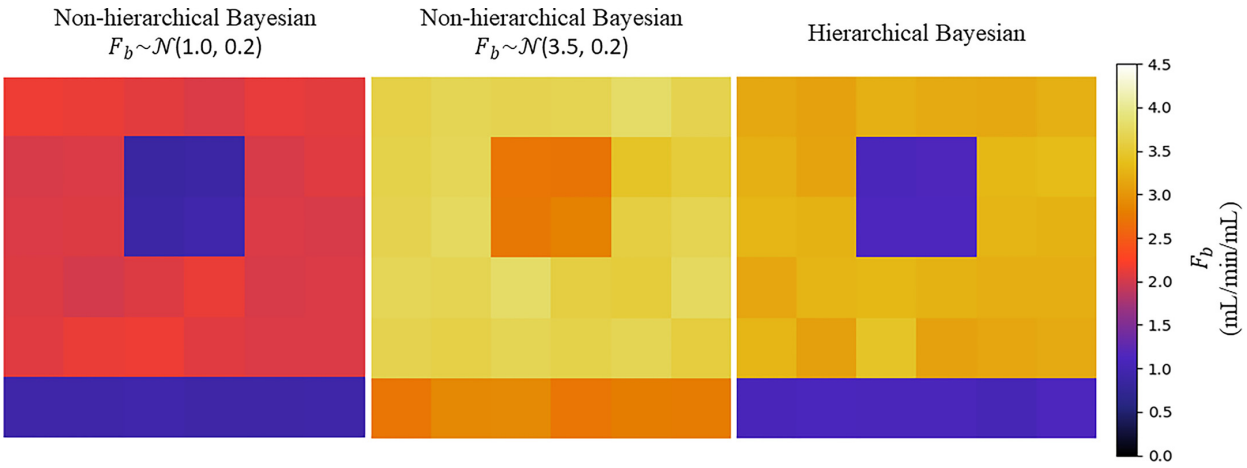

Fig. 4. The comparison between the hierarchical and non-hierarchical approach for an example noise realisation with the same ground-truth MBF maps at stress with a simulated perfusion defect as shown in Fig. 3. For the non-hierarchical approach, two different values for F_b prior have been applied. This shows the effect of using prior distributions with fixed means which influence the information from the data to drive the parameter estimate towards the prior value.

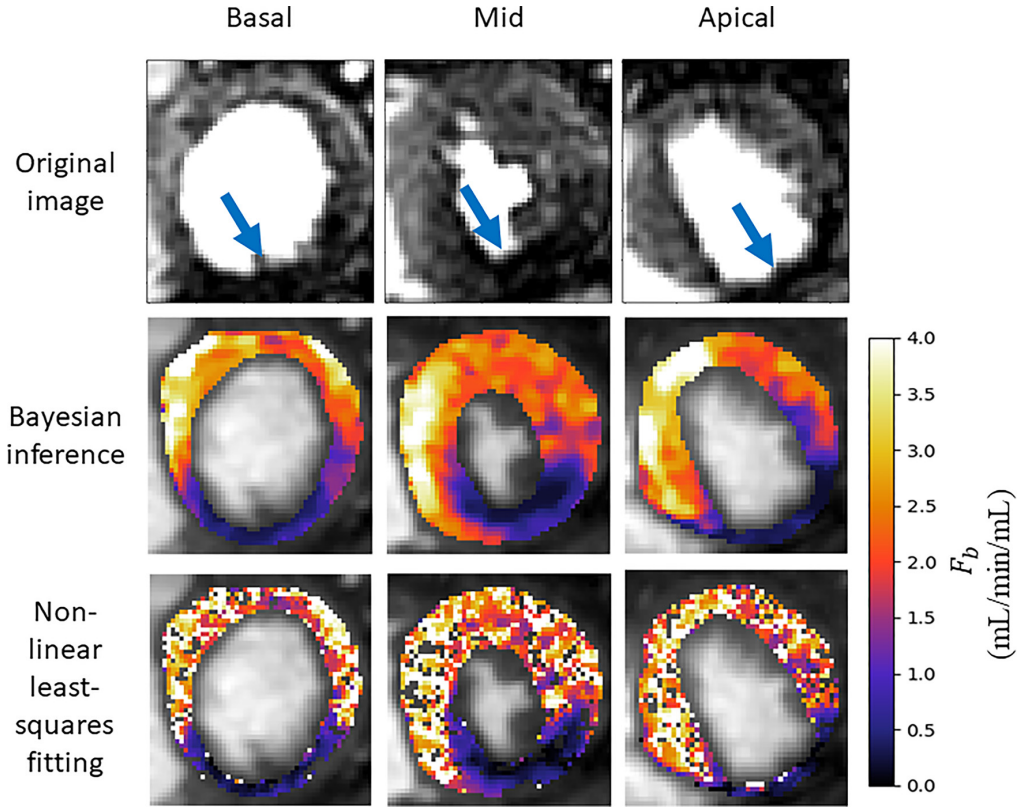

Fig. 5. A comparison of Bayesian inference versus least-squares fitting with 100 random initialisations for the three acquired slices for a patient with an overt perfusion defect (as indicated by the arrows in the first row). While both techniques identify the area of ischaemia the least-squares fittings have severe speckle-like noise and even gaps where the fitting has failed. This makes it more difficult to accurately delineate the boundaries of the ischaemic area and can lead to areas where the ischaemia is missed.

physiological ranges. The least-squares fitting fails for an average (standard deviation) of 12.9% (12.4%) of voxels per slice. Additionally, a MBF value of greater than 5 mL/min/mL (considered to be outliers) was found in 7.5% of voxels using least-squares fitting but never observed with the Bayesian inference. All kinetic parameter values are quoted in Table 2. The median (25th percentile, 75th percentile) coefficient of variation of the Bayesian posterior was 6.6% (3.3%, 11.7%). A maximum value of 87.7% was achieved with 0.8% of voxels having a parameter with a coefficient of variation greater than 50%.

The assessment of the presence of coronary artery disease based purely on the quantitative flow maps obtained using

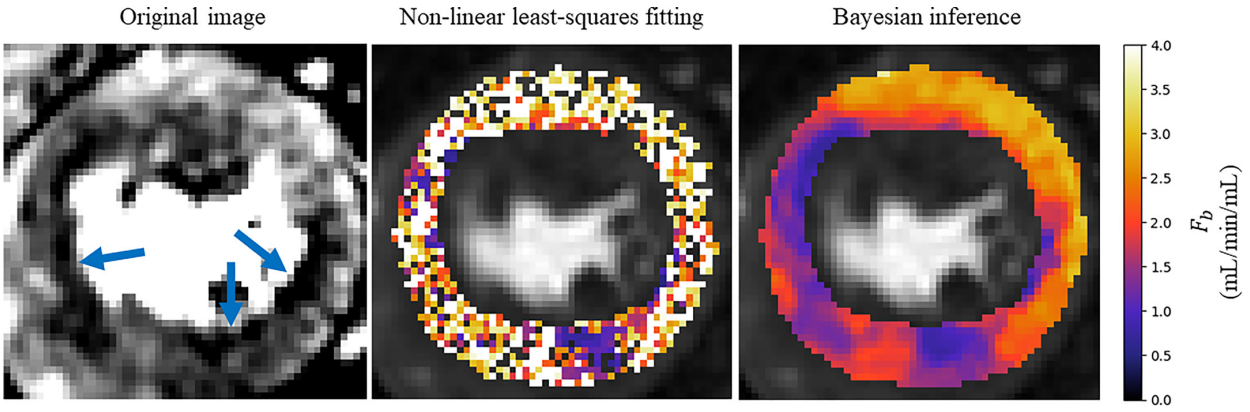

Fig. 6. An example slice where the Bayesian fitting (right) has correctly identified ischaemia but the noisy least squares fitting (middle) makes it difficult to identify the ischaemia, particularly in the infero-septal wall. The identified areas of ischaemia are indicated on the original MR image (left).

Table 2
Median (25th percentile, 75th percentile) kinetic parameter estimates, on the patient data, using the Bayesian inference and non-linear least squares fitting approaches.

Parameter	Bayesian	Non-linear least squares
F_b (mL/min/mL)	2.35 (1.9, 2.68)	2.37 (1.12, 3.01)
v_p (%/100)	0.09 (0.05, 0.13)	0.07 (0.03, 0.13)
v_e (%/100)	0.21 (0.13.0.31)	0.19 (0.12, 0.29)
PS (mL/min/mL)	0.88 (0.59,1.45)	3.3 (0.61, 4.74)

Bayesian inference matches the visual assessment in all 24 slices. When using the maps obtained by the least-squares fitting, a corresponding assessment is achieved in 16/24 slices. The computed flow parameter maps under stress conditions for an example patient with a perfusion defect are shown in Fig. 5. The identified areas of ischaemia are indicated with a blue arrow in the original MR images. An example of a slice where the least-squares fitting fails to correspond to the visual assessment is shown in Fig. 6. The visual assessment concluded that there is reduced uptake of contrast agent in both the inferior and infero-septal segments. This clearly corresponds with the Bayesian inference. The least-squares fitting is extremely noisy and the ischaemic area is under-estimated in the inferior segment and almost completely missed in the infero-septum. Fig. 7. shows all four kinetic parameters (left column) with the coefficient of variation of the MCMC sample of the parameter posterior distribution (right column).

5. Discussion

In this work, the use of Bayesian inference to estimate tracer-kinetic parameters from myocardial perfusion MRI data is investigated. This approach incorporates both spatial prior knowledge and prior knowledge on the kinetic parameter values. It also enables the computation of posterior distributions over the model parameters. It is compared to the more traditional method of parameter estimation, non-linear least squares fitting. This comparison first assesses the accuracy and reproducibility of the parameter estimations in a simulated, but realistic, setting. The two methods are also compared using patient data to assess the success of disease detection using the quantitative flow maps.

As discussed, a possible alternative approach is to use a simpler model for the quantitative modelling such as using a Fermi-constrained deconvolution (Jerosch-Herold et al., 1998; Zarinabad et al., 2012). The model to be fit to the data is simpler and has fewer parameters and thus can be fit more reliably, with less frequent failed fittings. However, such an approach only allows the resolution of MBF and the other parameters have no physiological interpretation. It is hypothesised that the extra physiological parameters that can be resolved using the two-compartment exchange model may allow a more informative assessment of the tissue. Tracer-kinetic models can also be fit more reliably on a segment-wise level due to the reduced noise after the signal averaging. However, it has been shown that the reduction of spatial resolution leads to a loss of diagnostic information (Villa et al., 2016; Zarinabad et al., 2015). It is also likely that increasing the number of time points that are sampled may increase the reliability of the estimates but this may not be possible in a clinical setting.

Lehnert et al. have also recently proposed the use of spatial regularisation (Lehnert et al., 2018). In this work, a Tikhonov (L2-norm) regularisation term is added to the cost function to be used in a gradient-based optimisation process. However, this is known, and seen in this work, to introduce smoothing over physiological borders where a large difference in kinetic parameters occurs. In fact, in Kelm et al. (2009) it was shown that a L1-norm regularisation is more suitable in applications that possess sharp edges between kinetic parameters, such as myocardial perfusion MRI. This motivates the use of a Laplace prior in our work which is equivalent to L1-norm regularisation. The benefits of the Bayesian approach also include the use of the MCMC exploration of parameter space which is less susceptible to local optima than gradient-based optimisations. Bayesian inference also yields an approximation of the posterior distribution of the parameters rather than a point-estimate with no indication of uncertainty.

Bayesian inference of tracer-kinetic parameters using DCE-MRI has been proposed previously (Dikaios et al., 2017; Orton et al., 2007; Schmid et al., 2006) and has in general been shown to be more reliable than non-linear least squares fitting. This work is however the first application to myocardial perfusion data, to our knowledge. The main innovation of this work is the utilisation of hierarchical priors. As discussed, hierarchical models allow model parameters to vary by group. The effect of using fixed priors is shown in Fig. 4. where the parameter estimates cannot adapt to areas that are largely different from the prior information (for example a perfusion defect). In this application, this is desirable in order to avoid the averaging effects between areas of ischaemia and healthy myocardium without having to distinguish between the two groups *a priori*. Hierarchical modelling has been applied to DCE-MRI data by Schmid et al. (2009) in the setting of a clinical trial where two scans were acquired per patient, before and after

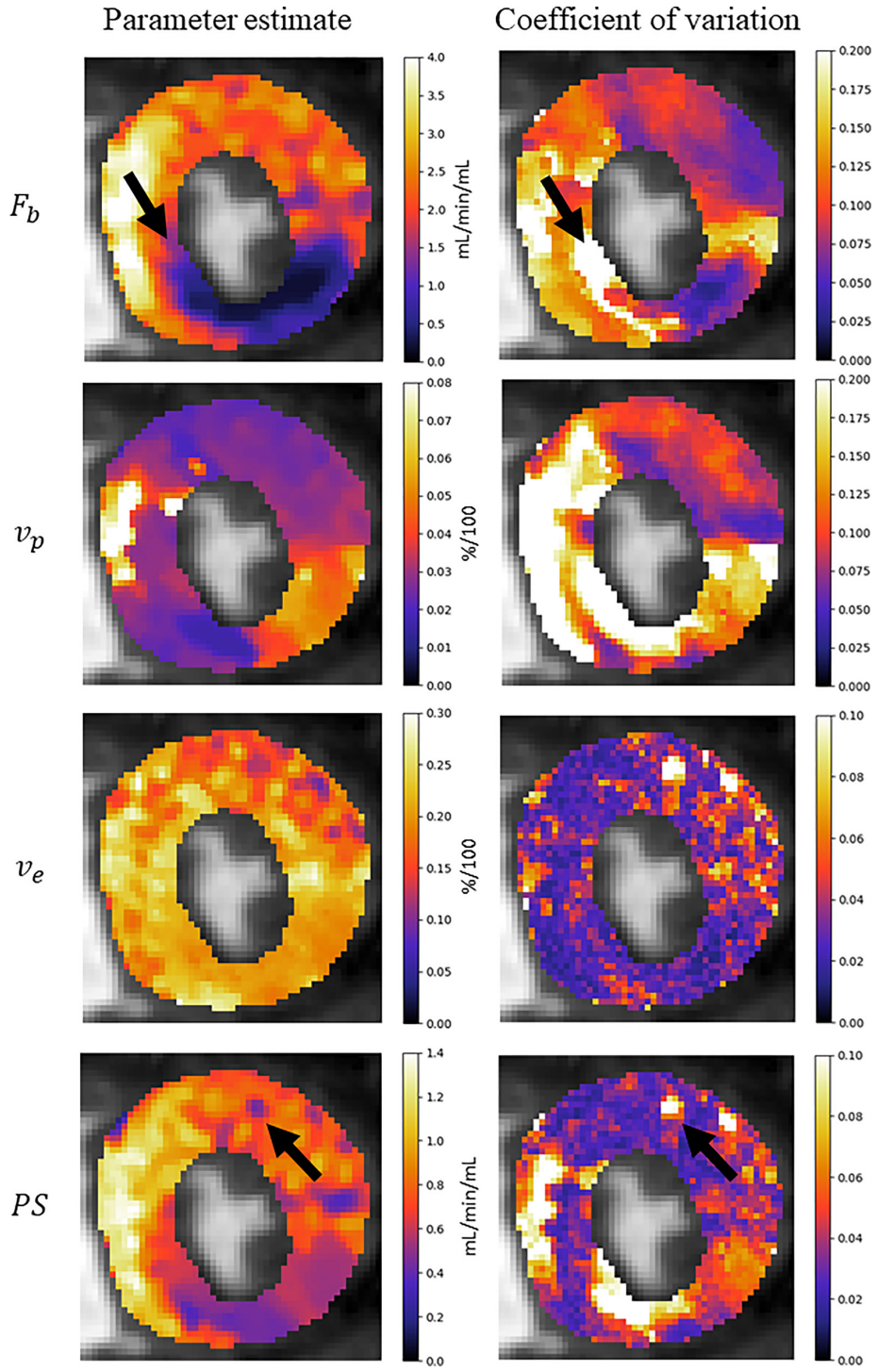

Fig. 7. Parameter maps for the four kinetic parameters of the 2CXM. The coefficient of variation represents the uncertainty about the parameter estimate and could be incorporated into the clinical decision making process. Black arrows are used to compare areas of high uncertainty to the respective parameter estimates.

treatment, leading to a temporal change in the kinetic parameters and thus two distinct groups of patients. This is different to our work which instead treats individual voxels in the spatial context as being from distinct groups, healthy or diseased. As such, in their study it is known *a priori* whether a scan was pre- or post-therapy, unlike in the current study where it is impossible to know whether a voxel is diseased.

Using the simulations, it was shown that the use of multiple different initial conditions improves the results of the non-linear least squares fitting as it helps the optimisation avoid local optima. However, it is still found in this work that the Bayesian inference technique presented is significantly more accurate than the standard least-squares fitting as evidenced by the NMSE between the estimated and true parameter values. Furthermore, the variability of the estimates is reduced, as shown by the lower standard deviation and the estimates are more reproducible across different noise realisations. The benefit of using a hierarchical model is also demonstrated. It is seen that in the presence of areas of reduced MBF, the prior knowledge of stress MBF values does not apply and the non-hierarchical model cannot account for the differences in groups of voxels (ischaemic and healthy). This leads to an averaging of the information from the data and the prior information and thus an over-estimation of MBF in these areas.

Naturally, there are no ground-truth values for comparison with the patient data estimates. However, the Bayesian parameter estimation leads to reduced numbers of outliers and failed fittings as compared to the least-squares fitting. The effect of this is shown in the parameter maps in Fig. 5. In this example, the perfusion defect in the inferior segment of the myocardium is clearly identified using both the Bayesian inference and least-squares fitting. However, there is still some speckle-like noise present in the least-squares estimates, even after 100 repeated fittings. The noisy estimates can make it difficult to delineate the boundaries of the ischaemia and in this case lead to the underestimation of the extent of the ischaemia. It is clear from that the Bayesian inference is identifying correctly the area of reduced contrast uptake in the inferior segment, which is visible in the original MR image at the correct windowing level and is easily picked up when assessing the quantitative flow maps.

Recent work, as presented by Kellman et al. (2017) has shown reproducible global MBF values, using similar tracer-kinetic models, in a consistent population of healthy volunteers (Brown et al., 2018) and a good correlation with the MBF values derived from positron emission tomography (PET) (Engblom et al., 2017) using a least-squares fitting approach. However, this work still shows a high within-subject variance between repeated studies. Furthermore, as shown in this study there is a high level of coupling between the model parameters and thus it is not possible to judge the reliability of the model fitting by evaluating a single parameter.

The unreliability of the tracer-kinetic parameter estimates has also been widely reported in the literature, Broadbent et al. (2013) reported failed fittings in 10% of cases on a segment-wise level. This is despite the fact they considered curves which have been averaged over a segment of the myocardium to boost SNR. Likhite et al. (2017) also showed incorrect model fits in a simulated setting as a result of the parameter coupling. Schwab et al. (2015) reports a median flow value (25th percentile, 75th percentile) of 3.055 (1.197,1168.4) mL/min/mL using the 2CXM model with the conventional least-squares fitting approach. The 75th percentile value reported is well in excess of 100 times of the range of values that are physiologically feasible. Both the mean and 75th percentile are lower in the results we have presented, due to the bounds used in the optimiser in our implementation but we also found a number of failed fittings and outliers. Furthermore, in this work the *PS* values are extremely variable which could be due to the short acquisition period. Capillary permeability is known to affect the later part of the curves and this process may not be fully observed. This indicates the unreliability of conventional perfusion estimates and hence the difficulty of the clinical translation of quantitative perfusion analysis is apparent.

The difficulty associated with the least-squares fitting is due to the ill-posedness of the parameter estimation problem and the complex nature of the cost function which can contain many local optima. The gradient-based optimisation schemes are thus sensitive to noise and susceptible to converging to the local minima and thus returning inaccurate parameter estimates (Dikaios et al., 2017; Kelm et al., 2009). This problem is exacerbated by the relative complexity of the 2CXM relative to the observed data and the complex errors introduced by the imaging process. The result of this is the noisy and often inaccurate estimates seen in this study.

Further well known issues with the standard least-squares fitting technique are that it is difficult to assess the uncertainty of the estimates and that these estimates are strongly dependant on the initial conditions of the optimisation process. The latter of these issues can be mitigated by using many randomly chosen initial positions but there is no structured or robust approach to doing this. These issues combine to limit the applicability of quantitative perfusion analysis in a clinical setting. Indeed, the patient data experiments show that the successful clinical classification of patients is worse with the least-squares fitting while perfect results are achieved with the Bayesian inference, albeit with a small sample size. The Bayesian inference does not depend on the initialisation of the optimisation as a burn-in period is used and these sample values are discarded. Furthermore, it provides a natural framework for quantifying the uncertainty of the estimates through the computation of the *a posteriori* probability distribution of the parameters.

In this work, using Bayesian inference, a median flow value (25th percentile, 75th percentile) of 2.35 (1.9, 2.68) mL/min/mL is computed. The 25th and 75th percentile values are well within the range of what is physiologically feasible, showing the increased reliability of the parameter estimates obtained using Bayesian inference. Despite the fact that these studies have been conducted with different cohort of patients it still serves to show the significant improvement that is gained by employing a Bayesian inference approach to the parameter estimation.

The coefficient of variation of the posterior distribution is used as a measure of uncertainty in the parameter estimate. The reported values indicate a reasonable level of confidence in the parameter estimates with the median coefficient of variation being 6.6%. However, higher coefficients of variation are also found, indicating high uncertainty in some regions. In Fig. 7., in the MBF parameter map (F_b), it is seen that there is a high level of uncertainty at the border between the ischaemic and healthy regions (indicated by arrows). It makes sense that there more uncertainty in these border regions and it could possibly be as a result of conflicting information from its neighbouring voxels which could be either ischaemic or healthy. In the *PS* parameter map, there is also an isolated area of reduced permeability. However, it is seen to be associated with a high level of uncertainty. This uncertainty can be incorporated into an assessment of whether or not there is reduced capillary permeability here. Thus, this uncertainty measure may prove to be useful in the clinical decision-making process but further work on this topic is warranted.

6. Limitations

One of the main criticisms of MCMC algorithms is the large computational cost involved in accurately approximating the posterior distribution, though the use of multiple random initialisations in the least-squares fitting is similarly computationally expensive.

In this work, the Bayesian takes approximately 30 min per imaging slice, as opposed to 3 min for the non-linear least squares fitting. However, the implementation of the Bayesian approach was not optimised and the computational cost could potentially be addressed using an efficient GPU-based implementation.

A limitation of tracer-kinetic modelling, in general, is that the models used are simplified versions of the underlying processes. The aim of this work was to examine whether Bayesian inference can yield more reliable parameter estimates that non-linear least squares fitting with the 2CXM. In the current work no effort was made to investigate whether this is the most suitable model for the application.

There are no ground-truth parameter values for patient data and as such there is no way to comment directly on the accuracy of the parameter estimates. The absolute quantitative accuracy needs validation in comparison to a gold standard technique such as microspheres. Further work is also required on the clinical utility of the findings. In this work, diagnostic accuracy is only compared with the expert clinical assessment, however future work will involve comparisons with the gold standard examinations, invasive coronary angiography and fractional flow reserve, in a larger patient cohort.

7. Conclusion

Tracer-kinetic parameters can be accurately and robustly inferred from myocardial perfusion MRI using hierarchical Bayesian inference. The use of a MCMC fitting scheme and the inclusion of spatial prior knowledge improves the reliability of the parameter estimation as compared with least-squares fitting. As a result of the improved model fitting, the diagnostic capabilities of the technique is increased.

Data statement

The datasets used and/or analysed during the current study are available from the corresponding author on reasonable request.

Declaration of Competing Interest

None.

Acknowledgements

The authors acknowledge financial support from the King's College London & Imperial College London EPSRC Centrefor Doctoral Training in Medical Imaging (EP/L015226/1); Philips Healthcare; The Alan Turing Institute under the EPSRC grant EP/N510129/1; The British Heart Foundation (TG/18/2/33768); The Department of Health via the National Institute for Health Research (NIHR) comprehensive Biomedical Research Centre award to Guy's & St Thomas' NHS Foundation Trust in partnership with King's College London and King's College Hospital NHS Foundation Trust and via the NIHR Cardiovascular MedTech Co-operative at Guy's and St Thomas' NHS Foundation Trust; The Centre of Excellence in Medical Engineering funded by the Wellcome Trust and EPSRC under grant number WT 088641/Z/09/Z.

Appendix

A.1. Residue function

The pair of coupled differential Eqs. (1) and (2) can be solved analytically using the Laplace transform to yield a solution in the form:

$$C_\Theta(t) = R_F(t,\Theta) * C_{AIF}(t-\tau_0)$$

The residue function R_F is given as: $R_F(t,\Theta) = A\ \exp(\alpha t) + (1-A)\ \exp(\beta t)$, where:

$$\alpha,\beta = \frac{1}{2}\left[-\left(\frac{PS}{v_p}+\frac{PS}{v_e}+\frac{F_p}{v_p}\right) \pm \sqrt{\left(\frac{PS}{v_p}+\frac{PS}{v_e}+\frac{F_p}{v_p}\right)^2 - 4\frac{PS}{v_e}\frac{F_p}{v_p}}\right]$$

$$A = \frac{\alpha + \frac{PS}{v_p} + \frac{PS}{v_e}}{\alpha-\beta}$$

References

Axel, L., 2018. Is qualitative cardiac perfusion MRI "Good enough"? JACC cardiovasc. Imaging 11, 719–721. https://doi.org/10.1016/j.jcmg.2017.11.038.

Bai, W., Sinclair, M., Tarroni, G., Oktay, O., Rajchl, M., Vaillant, G., Lee, A.M., Aung, N., Lukaschuk, E., Sanghvi, M.M., Zemrak, F., Fung, K., Paiva, J.M., Carapella, V., Kim, Y.J., Suzuki, H., Kainz, B., Matthews, P.M., Petersen, S.E., Piechnik, S.K., Neubauer, S., Glocker, B., Rueckert, D., 2018. Automated cardiovascular magnetic resonance image analysis with fully convolutional networks. J. Cardiovasc. Magn. Reson. 20, 1–12. https://doi.org/10.1186/s12968-018-0471-x.

Bardsley, J.M., 2012. Laplace-distributed increments, the Laplace prior, and edge-preserving regularization. J. Inverse Ill-Posed Probl. 20. https://doi.org/10.1515/jip-2012-0017.

Biglands, J.D., Ibraheem, M., Magee, D.R., Radjenovic, A., Plein, S., Greenwood, J.P., 2018. Quantitative myocardial perfusion imaging versus visual analysis in diagnosing myocardial ischemia: a CE-MARC substudy. JACC Cardiovasc. Imaging 11, 711–718. https://doi.org/10.1016/j.jcmg.2018.02.019.

Biglands, J.D., Magee, D.R., Sourbron, S.P., Plein, S., Greenwood, J.P., Radjenovic, A., 2015. Comparison of the diagnostic performance of four quantitative myocardial perfusion estimation methods used in cardiac MR imaging: CE-MARC substudy. Radiology 275, 393–402. https://doi.org/10.1148/radiol.14140433.

Broadbent, D.A., Biglands, J.D., Larghat, A., Sourbron, S.P., Radjenovic, A., Greenwood, J.P., Plein, S., Buckley, D.L., 2013. Myocardial blood flow at rest and stress measured with dynamic contrast-enhanced MRI: comparison of a distributed parameter model with a fermi function model. Magn. Reson. Med. 70, 1591–1597. https://doi.org/10.1002/mrm.24611.

Broadbent, D.A., Biglands, J.D., Ripley, D.P., Higgins, D.M., Greenwood, J.P., Plein, S., Buckley, D.L., 2016. Sensitivity of quantitative myocardial dynamic contrast-enhanced MRI to saturation pulse efficiency, noise and t1 measurement error: comparison of nonlinearity correction methods. Magn. Reson. Med. 75, 1290–1300. https://doi.org/10.1002/mrm.25726.

Brown, L.A.E., Onciul, S.C., Broadbent, D.A., Johnson, K., Fent, G.J., Foley, J.R.J., Garg, P., Chew, P.G., Knott, K., Dall'Armellina, E., Swoboda, P.P., Xue, H., Greenwood, J.P., Moon, J.C., Kellman, P., Plein, S., 2018. Fully automated, inline quantification of myocardial blood flow with cardiovascular magnetic resonance: repeatability of measurements in healthy subjects. J. Cardiovasc. Magn. Reson. 20. https://doi.org/10.1186/s12968-018-0462-y.

Buckley, D.L., 2002. Uncertainty in the analysis of tracer kinetics using dynamic contrast-enhanced T1-weighted MRI. Magn. Reson. Med. 47, 601–606. https://doi.org/10.1002/mrm.10080.

Cheng, A.S.H., Pegg, T.J., Karamitsos, T.D., Searle, N., Jerosch-Herold, M., Choudhury, R.P., Banning, A.P., Neubauer, S., Robson, M.D., Selvanayagam, J.B., 2007. Cardiovascular magnetic resonance perfusion imaging at 3-Tesla for the detection of coronary artery disease. A comparison with 1.5-Tesla. J. Am. Coll. Cardiol 49, 2440–2449. https://doi.org/10.1016/j.jacc.2007.03.028.

Cheong, L.H., Koh, T.S., Hou, Z., 2003. An automatic approach for estimating bolus arrival time in dynamic contrast MRI using piecewise continuous regression models. Phys. Med. Biol. 48. https://doi.org/10.1088/0031-9155/48/5/403.

Chiribiri, A., Bettencourt, N., Nagel, E., 2009. Cardiac magnetic resonance stress testing: results and prognosis. Curr. Cardiol. Rep 11, 54–60.

Dikaios, N., Atkinson, D., Tudisca, C., Purpura, P., Forster, M., Ahmed, H., Beale, T., Emberton, M., Punwani, S., 2017. A comparison of Bayesian and non-linear regression methods for robust estimation of pharmacokinetics in DCE-MRI and how it affects cancer diagnosis. Comput. Med. Imaging Graph. 56, 1–10. https://doi.org/10.1016/j.compmedimag.2017.01.003.

Engblom, H., Xue, H., Akil, S., Carlsson, M., Hindorf, C., Oddstig, J., Hedeer, F., Hansen, M.S., Aletras, A.H., Kellman, P., Arheden, H., 2017. Fully quantitative cardiovascular magnetic resonance myocardial perfusion ready for clinical use: a comparison between cardiovascular magnetic resonance imaging and positron emission tomography. J. Cardiovasc. Magn. Reson. 19, 1–9. https://doi.org/10.1186/s12968-017-0388-9.

Gelman, A., Rubin, D.B., 1992. Inference from iterative simulation using multiple sequences. Stat. Sci. 7, 457–472. https://doi.org/10.1214/ss/1177011136.

Hsu, L.-Y., Jacobs, M., Benovoy, M., Ta, A.D., Conn, H.M., Winkler, S., Greve, A.M., Chen, M.Y., Shanbhag, S.M., Bandettini, W.P., Arai, A.E., 2018. Diagnostic performance of fully automated pixel-wise quantitative myocardial perfusion imaging by cardiovascular magnetic resonance. JACC Cardiovasc. Imaging 1–11. https://doi.org/10.1016/j.jcmg.2018.01.005.

Ingrisch, M., Sourbron, S., 2013. Tracer-kinetic modeling of dynamic contrast-enhanced MRI and CT: a primer. J. Pharmacokinet. Pharmacodyn. 40, 281–300. https://doi.org/10.1007/s10928-013-9315-3.

Ishida, M., Schuster, A., Morton, G., Chiribiri, A., Hussain, S., Paul, M., Merkle, N., Steen, H., Lossnitzer, D., Schnackenburg, B., Alfakih, K., Plein, S., Nagel, E., 2011. Development of a universal dual-bolus injection scheme for the quantitative as-

sessment of myocardial perfusion cardiovascular magnetic resonance. J. Cardiovasc. Magn. Reson. 13, 28. https://doi.org/10.1186/1532-429X-13-28.

Jaarsma, C., Leiner, T., Bekkers, S.C., Crijns, H.J., Wildberger, J.E., Nagel, E., Nelemans, P.J., Schalla, S., 2012. Diagnostic performance of noninvasive myocardial perfusion imaging using single-photon emission computed tomography, cardiac magnetic resonance, and positron emission tomography imaging for the detection of obstructive coronary artery disease: a meta-anal. J. Am. Coll. Cardiol. 59, 1719–1728. https://doi.org/10.1016/j.jacc.2011.12.040.

Jacobs, M., Benovoy, M., Chang, L.-.C., Arai, A.E., Hsu, L.-.Y., 2016. Evaluation of an automated method for arterial input function detection for first-pass myocardial perfusion cardiovascular magnetic resonance. J. Cardiovasc. Magn. Reson. 18, 17. https://doi.org/10.1186/s12968-016-0239-0.

Jerosch-herold, M., 2010. Quantification of myocardial perfusion by cardiovascular magnetic resonance. J. Cardiovasc. Magn. Reson. 12, 1–16.

Jerosch-Herold, M., Stillman, A.E., Wilke, N., 1998. Magnetic resonance quantification of the myocardial perfusion reserve with a Fermi function model for constrained deconvolution. Med. Phys. 25, 73–84. https://doi.org/10.1118/1.598163.

Kellman, P., Hansen, M.S., Nielles-Vallespin, S., Nickander, J., Themudo, R., Ugander, M., Xue, H., 2017. Myocardial perfusion cardiovascular magnetic resonance: optimized dual sequence and reconstruction for quantification. J. Cardiovasc. Magn. Reson. 19, 43. https://doi.org/10.1186/s12968-017-0355-5.

Kelm, B.M., Menze, B.H., Nix, O., Zechmann, C.M., Hamprecht, F.A., 2009. Contrast-Enhanced MRI using spatial prior knowledge. IEEE Trans. Med. Imaging 28, 1534–1547.

Knott, K.D., Camaioni, C., Ramasamy, A., Augusto, J.A., Bhuva, A.N., Xue, H., Manisty, C., Hughes, R.K., Brown, L.A.E., Amersey, R., Bourantas, C., Kellman, P., Plein, S., Moon, J.C., 2019. Quantitative myocardial perfusion in coronary artery disease: a perfusion mapping study. J. Magn. Reson. Imaging.. https://doi.org/10.1002/jmri.26668.

Kramer, C.M., Barkhausen, J., Flamm, S.D., Kim, R.J., Nagel, E., 2013. Standardized cardiovascular magnetic resonance (CMR) protocols 2013 update. J. Cardiovasc. Magn. Reson 15, 1–10. https://doi.org/10.1186/1532-429X-15-91.

Larsson, H.B., Fritz-Hansen, T., Rostrup, E., Søndergaard, L., Ring, P., Henriksen, O., 1996. Myocardial perfusion modeling using MRI. Magn. Reson. Med 35, 716–726. https://doi.org/10.1002/mrm.1910350513.

Lehnert, J., Wübbeler, G., Kolbitsch, C., Chiribiri, A., Coquelin, L., Ebrard, G., Smith, N., Schaeffter, T., Elster, C., 2018. Pixel-wise quantification of myocardial perfusion using spatial Tikhonov regularization. Phys. Med. Biol. 63, 215017. https://doi.org/10.1088/1361-6560/aae758.

Li, M., Zhou, T., Yang, L.F., Peng, Z.H., Ding, J., Sun, G., 2014. Diagnostic accuracy of myocardial magnetic resonance perfusion to diagnose ischemic stenosis with fractional flow reserve as reference: systematic review and meta-analysis. JACC Cardiovasc. Imaging 7, 1098–1105. https://doi.org/10.1016/j.jcmg.2014.07.011.

Likhite, D., Suksaranjit, P., Adluru, G., Wilson, B., DiBella, E., 2017. Estimating extraction fraction and blood flow by combining first-pass myocardial perfusion and T1 mapping results. Quant. Imaging Med. Surg. 7, 480–495. https://doi.org/10.21037/qims.2017.08.07.

Montalescot, G., Sechtem, U., Achenbach, S., Andreotti, F., Arden, C., Budaj, A., Bugiardini, R., Crea, F., Cuisset, T., Di Mario, C., Ferreira, J.R., Gersh, B.J., Gitt, A.K., Hulot, J.-.S., Marx, N., Opie, L.H., Pfisterer, M., Prescott, E., Ruschitzka, F., Sabaté, M., Senior, R., Taggart, D.P., van der Wall, E.E., Vrints, C.J.M., Zamorano, J.L., Achenbach, S., Baumgartner, H., Bax, J.J., Bueno, H., Dean, V., Deaton, C., Erol, C., Fagard, R., Ferrari, R., Hasdai, D., Hoes, A.W., Kirchhof, P., Knuuti, J., Kolh, P., Lancellotti, P., Linhart, A., Nihoyannopoulos, P., Piepoli, M.F., Ponikowski, P., Sirnes, P.A., Tamargo, J.L., Tendera, M., Torbicki, A., Wijns, W., Windecker, S., Knuuti, J., Valgimigli, M., Bueno, H., Claeys, M.J., Donner-Banzhoff, N., Erol, C., Frank, H., Funck-Brentano, C., Gaemperli, O., Gonzalez-Juanatey, J.R., Hamilos, M., Hasdai, D., Husted, S., James, S.K., Kervinen, K., Kolh, P., Kristensen, S.D., Lancellotti, P., Maggioni, A, Pietro, Piepoli, M.F., Pries, A.R., Romeo, F., Rydén, L., Simoons, M.L., Sirnes, P.A., Steg, P.G., Timmis, A., Wijns, W., Windecker, S., Yildirir, A., Zamorano, J.L., 2013. 2013 ESC guidelines on the management of stable coronary artery disease. Eur. Heart J. 34, 2949–3003. https://doi.org/10.1093/eurheartj/eht296.

Nagel, E., Greenwood, J.P., McCann, G.P., Bettencourt, N., Shah, A.M., Hussain, S.T., Perera, D., Plein, S., Bucciarelli-Ducci, C., Paul, M., Westwood, M.A., Marber, M., Richter, W.-.S., Puntmann, V.O., Schwenke, C., Schulz-Menger, J., Das, R., Wong, J., Hausenloy, D.J., Steen, H., Berry, C., 2019. Magnetic resonance perfusion or fractional flow reserve in coronary disease. N. Engl. J. Med.. https://doi.org/10.1056/nejmoa1716734.

Nagel, E., Klein, C., Paetsch, I., Hettwer, S., Schnackenburg, B., Wegscheider, K., Fleck, E., 2003. Magnetic resonance perfusion measurements for the noninvasive detection of coronary artery disease. Circulation 108, 432–437. https://doi.org/10.1161/01.CIR.0000080915.35024.A9.

Orton, M.R., Collins, D.J., Walker-Samuel, S., D'Arcy, J.A., Hawkes, D.J., Atkinson, D., Leach, M.O., 2007. Bayesian estimation of pharmacokinetic parameters for DCE-MRI with a robust treatment of enhancement onset time. Phys. Med. Biol. 52, 2393–2408. https://doi.org/10.1088/0031-9155/52/9/005.

Patel, A.R., Antkowiak, P.F., Nandalur, K.R., West, A.M., Salerno, M., Arora, V., Christopher, J., Epstein, F.H., Kramer, C.M., 2010. Assessment of advanced coronary artery disease: advantages of quantitative cardiac magnetic resonance perfusion analysis. J. Am. Coll. Cardiol. 56, 561–569. https://doi.org/10.1016/j.jacc.2010.02.061.

Roberts, G.O., Gelman, A., Gilks, W.R., 1997. Weak convergence and optimal scaling of random walk metropolis algorithms. Ann. Appl. Probab. 7, 110–120. https://doi.org/10.1214/aoap/1034625254.

Romain, B., Rouet, L., Ohayon, D., Lucidarme, O., d'Alché-Buc, F., Letort, V., 2017. Parameter estimation of perfusion models in dynamic contrast-enhanced imaging: a unified framework for model comparison. Med. Image Anal. 35, 360–374. https://doi.org/10.1016/j.media.2016.07.008.

Rosenbaum, B., Raatz, M., Weithoff, G., Fussmann, G.F., Gaedke, U., 2019. Estimating parameters from multiple time series of population dynamics using Bayesian inference. Front. Ecol. Evol. 6. https://doi.org/10.3389/fevo.2018.00234.

Sammut, E.C., Villa, A.D.M., Di Giovine, G., Dancy, L., Bosio, F., Gibbs, T., Jeyabraba, S., Schwenke, S., Williams, S.E., Marber, M., Alfakih, K., Ismail, T.F., Razavi, R., Chiribiri, A., 2017. Prognostic value of quantitative stress perfusion cardiac magnetic resonance. JACC Cardiovasc. Imaging.. https://doi.org/10.1016/j.jcmg.2017.07.022.

Scannell, C.M., Villa, A.D.M., Lee, J., Breeuwer, M., Chiribiri, A., 2019. Robust non–rigid motion compensation of free-breathing myocardial perfusion MRI data. IEEE Trans. Med. Imaging 38, 1812–1820.

Schmid, V.J., Whitcher, B., Padhani, A.R., Jane Taylor, N., Yang, G.Z., 2009. A bayesian hierarchical model for the analysis of a longitudinal dynamic contrast-enhanced MRI oncology study. Magn. Reson. Med. 61, 163–174. https://doi.org/10.1002/mrm.21807.

Schmid, V.J., Whitcher, B., Padhani, A.R., Taylor, N.J., Yang, G.Z., 2006. Bayesian methods for pharmacokinetic models in dynamic contrast-enhanced magnetic resonance imaging. IEEE Trans. Med. Imaging 25, 1627–1636. https://doi.org/10.1109/TMI.2006.884210.

Schwab, F., Ingrisch, M., Marcus, R., Bamberg, F., Hildebrandt, K., Adrion, C., Gliemi, C., Nikolaou, K., Reiser, M., Theisen, D., 2015. Tracer kinetic modeling in myocardial perfusion quantification using MRI. Magn. Reson. Med. 73, 1206–1215. https://doi.org/10.1002/mrm.25212.

Seber, G.A.F., Wild, C.J., 1989. Nonlinear Regression, Wiley Series in Probability and Statistics. John Wiley & Sons, Inc., Hoboken, NJ, USA https://doi.org/10.1002/0471725315.

Sommer, J.C., Schmid, V.J., 2014. Spatial two-tissue compartment model for dynamic contrast-enhanced magnetic resonance imaging. J. R. Stat. Soc. Ser. C Appl. Stat. 63, 695–713. https://doi.org/10.1111/rssc.12057.

Sourbron, S.P., Buckley, D.L., 2013. Classic models for dynamic contrast-enhanced MRI. NMR Biomed 26, 1004–1027. https://doi.org/10.1002/nbm.2940.

Tofts, P.S., Kermode, A.G., 1991. Measurement of the blood-brain barrier permeability and leakage space using dynamic MR imaging. 1. fundamental concepts. Magn Reson Med 17, 357–367. https://doi.org/10.1002/mrm.1910170208.

Villa, A.D.M., Corsinovi, L., Ntalas, I., Milidonis, X., Scannell, C., Di Giovine, G., Child, N., Ferreira, C., Nazir, M.S., Karady, J., Eshja, E., De Francesco, V., Bettencourt, N., Schuster, A., Ismail, T.F., Razavi, R., Chiribiri, A., 2018. Importance of operator training and rest perfusion on the diagnostic accuracy of stress perfusion cardiovascular magnetic resonance. J. Cardiovasc. Magn. Reson. 20, 74. https://doi.org/10.1186/s12968-018-0493-4.

Villa, A.D.M., Sammut, E., Zarinabad, N., Carr-White, G., Lee, J., Bettencourt, N., Razavi, R., Nagel, E., Chiribiri, A., 2016. Microvascular ischemia in hypertrophic cardiomyopathy: new insights from high-resolution combined quantification of perfusion and late gadolinium enhancement. J. Cardiovasc. Magn. Reson. 18. https://doi.org/10.1186/s12968-016-0223-8.

Wilke, N., Jerosch-Herold, M., Wang, Y., Huang, Y., Christensen, B.V., Stillman, A.E., Ugurbil, K., McDonald, K., Wilson, R.F., 1997. Myocardial perfusion reserve: assessment with multisection, quantitative, first-pass MR imaging. Radiology 204, 373–384. https://doi.org/10.1148/radiology.204.2.9240523.

Windecker, S., Kolh, P., Alfonso, F., Collet, J.-.P., Cremer, J., Falk, V., Filippatos, G., Hamm, C., Head, S.J., Jüni, P., Kappetein, A.P., Kastrati, A., Knuuti, J., Landmesser, U., Laufer, G., Neumann, F.-.J., Richter, D.J., Schauerte, P., Sousa Uva, M., Stefanini, G.G., Taggart, D.P., Torracca, L., Valgimigli, M., Wijns, W., Witkowski, A., Zamorano, J.L., Achenbach, S., Baumgartner, H., Bax, J.J., Bueno, H., Dean, V., Deaton, C., Erol, Ç., Fagard, R., Ferrari, R., Hasdai, D., Hoes, A.W., Kirchhof, P., Knuuti, J., Kolh, P., Lancellotti, P., Linhart, A., Nihoyannopoulos, P., Piepoli, M.F., Ponikowski, P., Sirnes, P.A., Tamargo, J.L., Tendera, M., Torbicki, A., Wijns, W., Windecker, S., Sousa Uva, M., Achenbach, S., Pepper, J., Anyanwu, A., Badimon, L., Bauersachs, J., Baumbach, A., Beygui, F., Bonaros, N., De Carlo, M., Deaton, C., Dobrev, D., Dunning, J., Eeckhout, E., Gielen, S., Hasdai, D., Kirchhof, P., Luckraz, H., Mahrholdt, H., Montalescot, G., Paparella, D., Rastan, A.J., Sanmartin, M., Sergeant, P., Silber, S., Tamargo, J., ten Berg, J., Thiele, H., van Geuns, R.-.J., Wagner, H.-.O., Wassmann, S., Wendler, O., Zamorano, J.L., Weidinger, F., Ibrahimov, F., Legrand, V., Terzić, I., Postadzhiyan, A., Skoric, B., Georgiou, G.M., Zelizko, M., Junker, A., Eha, J., Romppanen, H., Bonnet, J.-.L., Aladashvili, A., Hambrecht, R., Becker, D., Gudnason, T., Segev, A., Bugiardini, R., Sakhov, O., Mirrakhimov, A., Pereira, B., Felice, H., Trovik, T., Dudek, D., Pereira, H., Nedeljkovic, M.A., Hudec, M., Cequier, A., Erlinge, D., Roffi, M., Kedev, S., Addad, F., Yildirir, A., Davies, J., 2014. 2014 ESC/EACTS guidelines on myocardial revascularization. Eur. Heart J. 35, 2541–2619. https://doi.org/10.1093/eurheartj/ehu278.

Zarinabad, N., Chiribiri, A., Hautvast, G.L.T.F., Breeuwer, M., Nagel, E., 2015. Influence of spatial resolution on the accuracy of quantitative myocardial perfusion in first pass stress perfusion CMR. Magn. Reson. Med. 73, 1623–1631. https://doi.org/10.1002/mrm.25249.

Zarinabad, N., Chiribiri, A., Hautvast, G.L.T.F., Ishida, M., Schuster, A., Cvetkovic, Z., Batchelor, P.G., Nagel, E., 2012. Voxel-wise quantification of myocardial perfusion by cardiac magnetic resonance. Feasibility and methods comparison. Magn. Reson. Med. 68, 1994–2004. https://doi.org/10.1002/mrm.24195.

Zhu, C., Byrd, R.H., Lu, P., Nocedal, J., 1997. Algorithm 778: L-BFGS-B: Fortran subroutines for large-scale bound-constrained optimization. ACM Trans. Math. Softw. 23, 550–560. https://doi.org/10.1145/279232.279236.

Jones, E., Oliphant, T., Peterson, P., others, 2001. SciPy: open source scientific tools for python. Available: http://www.scipy.org/.

6.3 Correction

In the appendix of Section 6.2, it is stated that:

$$R_F(t,\theta) = A\exp(\alpha t) + (1-A)\exp(\beta t). \tag{6.8}$$

This should read as:

$$R_F(t,\theta) = F_p \cdot (A\exp(\alpha t) + (1-A)\exp(\beta t)). \tag{6.9}$$

Chapter 7

Preliminary evaluation

7.1 Introduction

As discussed, stress perfusion CMR is now an established technique for the assessment of patients with CAD [2, 3] and it is playing an expanding role in the assessment of patients with angina and coronary microvascular dysfunction (MVD) [106]. Although a high diagnostic accuracy and prognostic value is found with visual assessment at experienced centres, quantification is required to make this a widespread clinical reality. Therefore, this chapter presents a preliminary, proof of principle evaluation of the automated pipeline for stress perfusion quantification that was presented in Chapters 4, 5, and 6. In particular, the ability of stress perfusion CMR to detect myocardial ischaemia is demonstrated, both in patients with obstructive epicardial CAD and MVD. This paves the way for a more thorough validation study and the subsequent clinical adoption of quantitative stress perfusion CMR.

7.2 Material and methods

7.2.1 Patients

In total, 47 patients were included in this study. Of these, 36 patients with known or suspected CAD referred on clinical grounds for a stress perfusion CMR, who had a subsequent invasive coronary angiography, were retrospectively included. A further 11 patients who had MVD diagnosed by exclusion, demonstrable ischaemia with angiographically smooth coronary arteries, were also included. All patients had invasive coronary angiography within 3 months and the cut-off point for coronary lumen stenosis was 70% for epicardial vessels. All invasive angiographic images have been reviewed by consensus of expert operators.

7.2.2 Image acquisition

All examinations were performed on a 3T system (Achieva TX, Philips Healthcare, Best, The Netherlands) using a 32-channel cardiac phased array receiver coil. Perfusion images were acquired in 3 LV short-axis slices (apical, mid-cavity, and basal) at mid-expiration with a saturation-recovery gradient echo method (repetition time 3.0 ms, echo time 1.0 ms, flip angle 15°, saturation-recovery delay 120 ms, sensitivity encoding (SENSE) parallel imaging, representative spatial resolution 1.5x1.5x10 mm^3). Stress images were acquired during adenosine-induced hyperaemia (140μg/kg/min). 0.075 mmol/kg of bodyweight gadolinium (Gd) extracellular contrast agent (gadobutrol, Gadovist, Bayer, Germany) was injected at 4 mL/s followed by a 20-mL saline flush for each perfusion acquisition. Each bolus of gadobutrol was preceded by a diluted pre-bolus with 10% of the dose to allow quantification of perfusion, according to published methods [48].

7.2.3 Image processing

The perfusion images were corrected for respiratory motion (Chapter 4) and processed fully-automatically using our deep learning-based processing pipeline (Chapter 5). Pixel-wise time signal intensity curves were extracted from the myocardial mask and signal intensity curves were subsequently split into the time intervals corresponding to the pre bolus injection and the main bolus injection for quantification, using Bayesian inference (Chapter 6). The pixel-wise MBF estimates were assigned to standard AHA segments using the automatically computed RV insertion points. AHA segments are attributed to coronary perfusion territories as described by Cerqueira et al. [107]. Each AHA segment is further sub-divided into an endocardial and epicardial layer to yield 32 segments. For the purpose of detecting CAD, Lockie et al. [79] validated the use of the mean value of the two lowest MBF values in a perfusion territory to represent that vessel. This work uses the mean of the four lowest MBF values as our segments are half the size.

7.2.4 Quantitative analysis

A series of comparisons are performed. The first of which is to assess the ability of quantitative stress CMR to detect ischaemia and thus compares the patients with no significant CAD (CAD-) against the groups of patients with ischaemia, that is those with significant CAD (CAD+) or MVD. The second assessment is the ability to distinguish between significant CAD and no significant CAD and compares the CAD+ and CAD-. This is done on both a per-patient and

	n = 47
Age (years)	59.66 ± 8.03
Male	26 (55)
BMI	28.11 ± 3.89
Hypertension	22 (47)
Hypercholesterolemia	25 (53)
Diabetes	14 (30)
Smoker	8 (17)
Ex-smoker	14 (30)
Previous PCI	12 (26)
Previous CABG	0 (0)

Values are n (%) or mean ± SD

Table 7.1 Baseline demographics of the patient cohort. PCI, percutaneous coronary intervention; CABG, coronary artery bypass grafting.

per-coronary vessel level. The final assessment is the ability to detect MVD in the setting of patients with anatomically smooth coronary arteries and thus compares CAD- against MVD.

7.2.5 Statistical analysis

The data are presented as mean ± standard deviation (SD) and compared using two-sided Student *t*-tests. p values < 0.05 were considered statistically significant. ROC curve analysis was used to report the diagnostic accuracy of the proposed approach. The data was analysed on both the per-patient and per-coronary vessel level. All statistical analysis was performed using SciPy and Pingouin [108, 109].

7.3 Results

The baseline patient characteristics are summarised in Table 7.1. 17 patients had no significant coronary lesions or MVD. In 19 patients with CAD, there was 38 vessels with significant lesions and 11 patients had MVD. The findings of the angiography data are shown in Table 7.2.

45/47 patients were successfully analysed with two having failed contrast injections. The mean MBF value over all patients was 1.93 ± 0.52 ml/min/g. The other microcirculatory parameters estimated were $v_b = 0.08 \pm 0.04$, $v_e = 0.18 \pm 0.08$, and $PS = 0.65 \pm 0.31$ ml/min/g. The distribution of global MBF values for the three patient groups (CAD+, MVD, and CAD-) is shown in Figure 7.1. The mean MBF in CAD- patients was 2.35 ± 0.46 ml/min/g, in MVD patients was 1.72 ± 0.3 ml/min/g, and in CAD+ patients was 1.67 ± 0.36 ml/min/g. The

	n = 47
No significant CAD	17 (36)
1-vessel disease	7 (15)
2-vessel disease	2 (4)
3-vessel disease	10 (21)
MVD	11 (23)

Values are n (%)

Table 7.2 Angiographic findings

MBF was significantly reduced in both the CAD+ and MVD groups as compared to the CAD- group (both $p < 0.01$), indicating the presence of significant ischaemia. There was no statistical difference in the mean MBF between the MVD and CAD+ patients ($p = 0.53$).

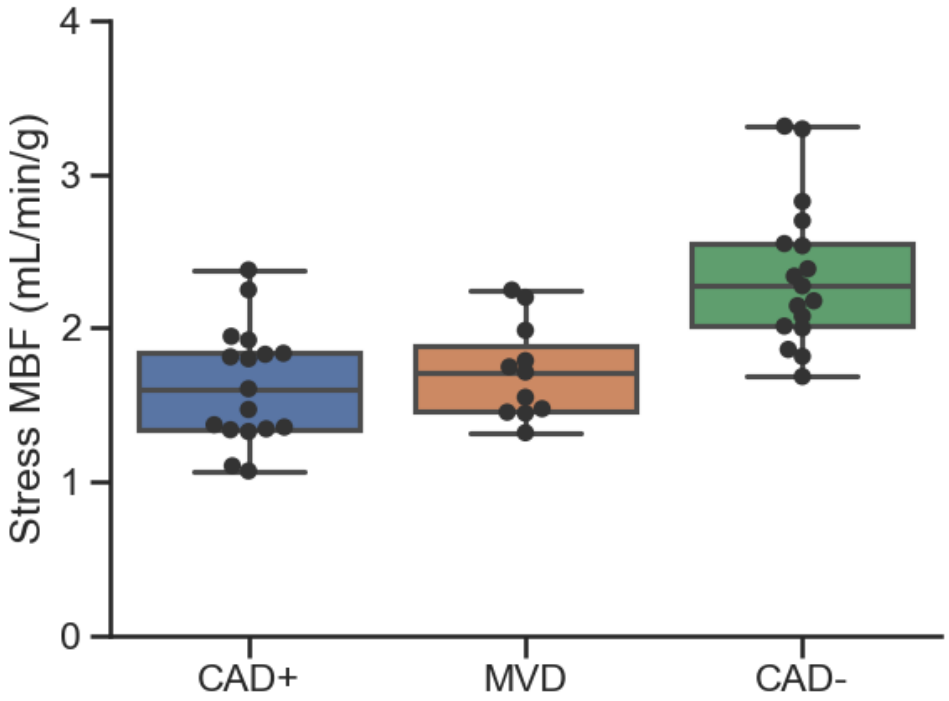

Fig. 7.1 The distributions of global MBF values in the different patient groups.

In the setting of patients with known or suspected CAD, the ROC curve in Figure 7.2 shows that quantitative stress perfusion CMR distinguishes well between CAD- and CAD+ patients. The area under the curve (AUC) of the ROC curve was 0.94 and using an threshold of 1.34 ml/ min /g to detect CAD achieved a sensitivity of 94.4%, a specificity of 93.8%, and a diagnostic accuracy of 91%. Figures 7.3 and 7.4 show examples of quantitative perfusion maps

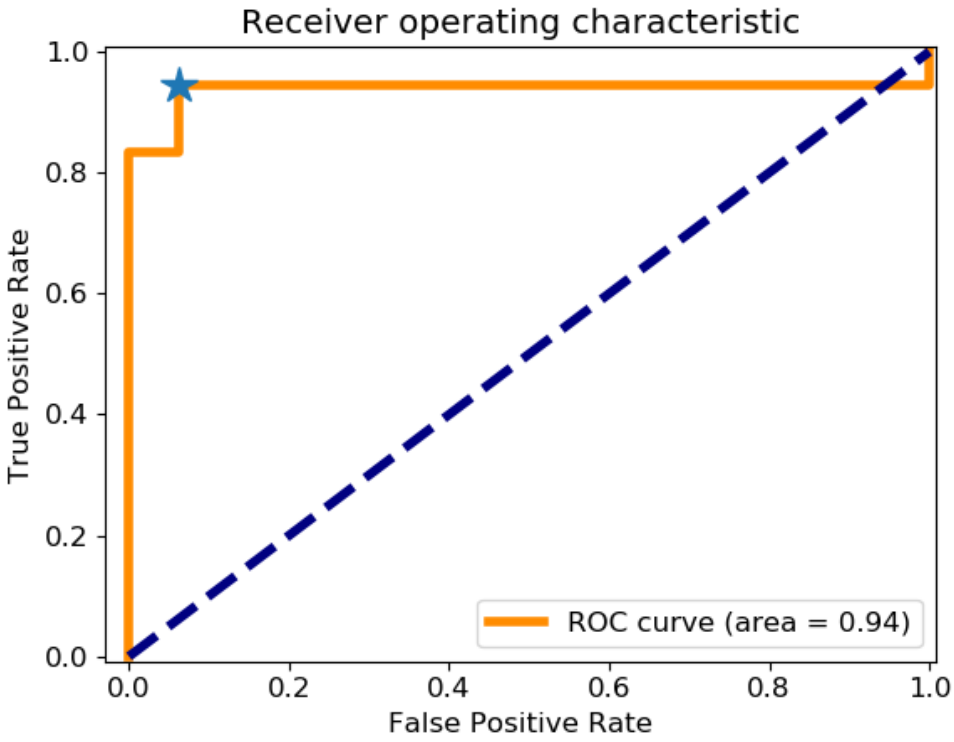

Fig. 7.2 The ROC analysis for the diagnosis of CAD on a per-patient level.

and the corresponding segmental analysis for patients correctly classified as CAD- and CAD+, respectively.

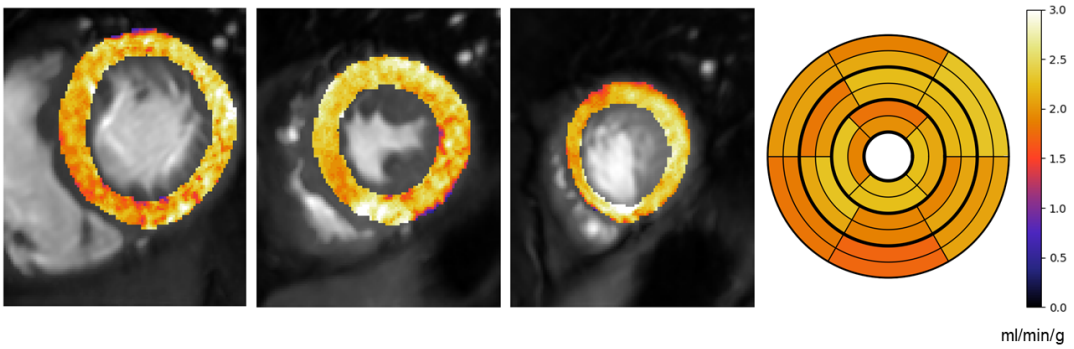

Fig. 7.3 Quantitative MBF maps and 32 segment representation for a CAD- patient.

This diagnostic power is reduced on the per-vessel assessment. The ROC curve is shown in Figure 7.5 and the AUC of the ROC curve is 0.86, with the threshold of 1.31 ml/min/g giving a sensitivity of 87.3%, a specificity of 77.1%, and a diagnostic accuracy of 83.3%. The mean MBF in regions supplied by vessels with a stenosis was 1.19 ± 0.28 ml/min/g. This was

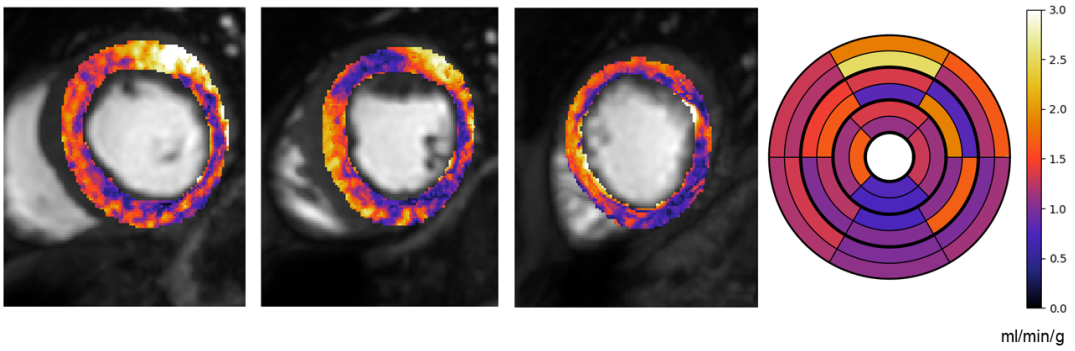

Fig. 7.4 Quantitative MBF maps and 32 segment representation for a CAD+ patient.

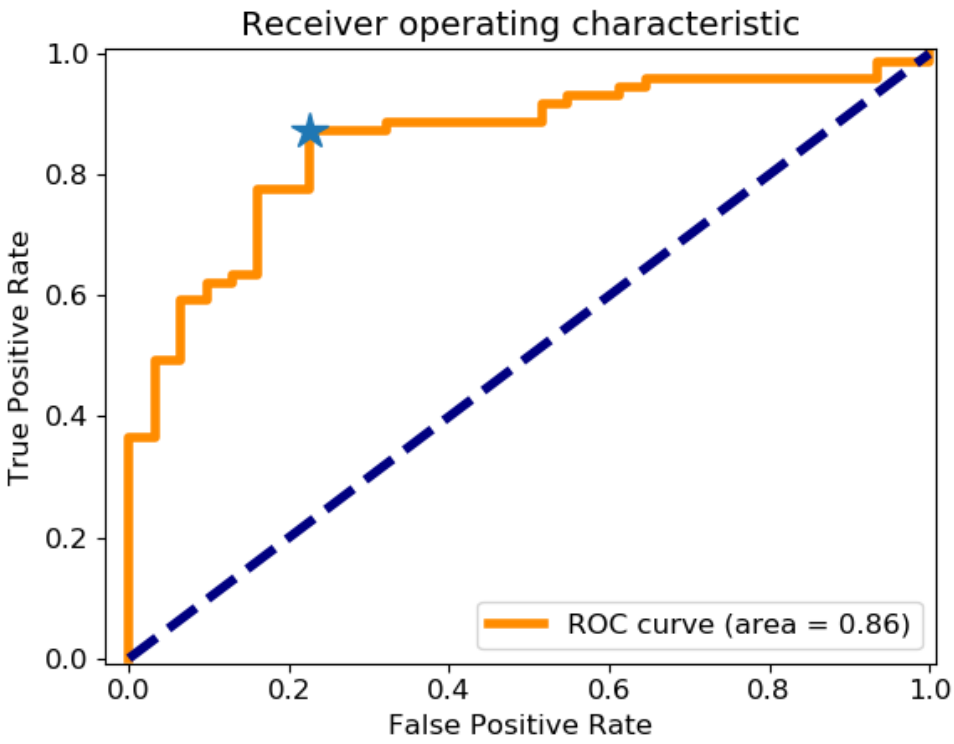

Fig. 7.5 The ROC analysis for the diagnosis of CAD on a per-vessel level.

significantly higher in regions supplied by vessels without a stenosis at 1.8 ± 0.59 ml/ min /g ($p < 0.01$). An example patient with misclassified vessels is shown in Figure 7.7. This patient has triple vessel disease but is classified as being ischaemic in only the LAD territory. The ischaemia in the circumflex region is subtle and restricted to sub-endocardial region in the mid slice which is not picked up by the segmental analysis. Furthermore, the ischaemia in the RCA territory is visible in the septal/inferoseptal segments of the mid and apical slices but the perfusion values are in an intermediate range and do not fall below the threshold for ischaemia.

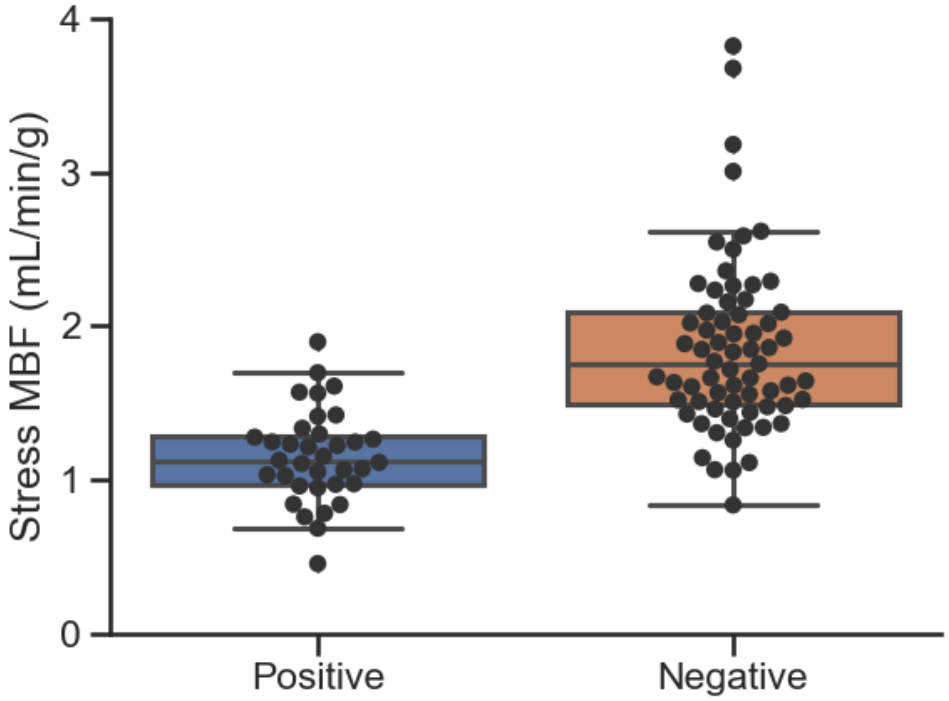

Fig. 7.6 The distribution of MBF values recorded for each vessel in the CAD+ patients, divided between positive (for CAD) and negative.

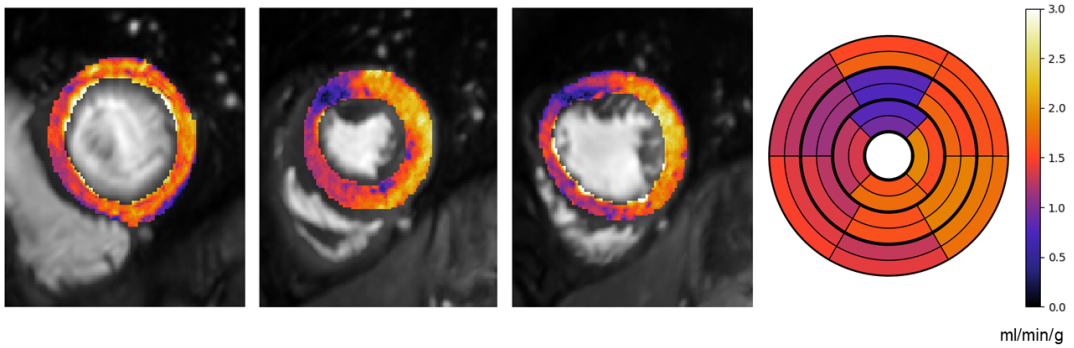

Fig. 7.7 An example of a misclassified patient. The patient has triple vessel disease and while they are correctly identified as CAD+ by the MBF values, they are misclassified as having single vessel disease (LAD). There are significant lesions but not significant ischaemia in the LCx and RCA.

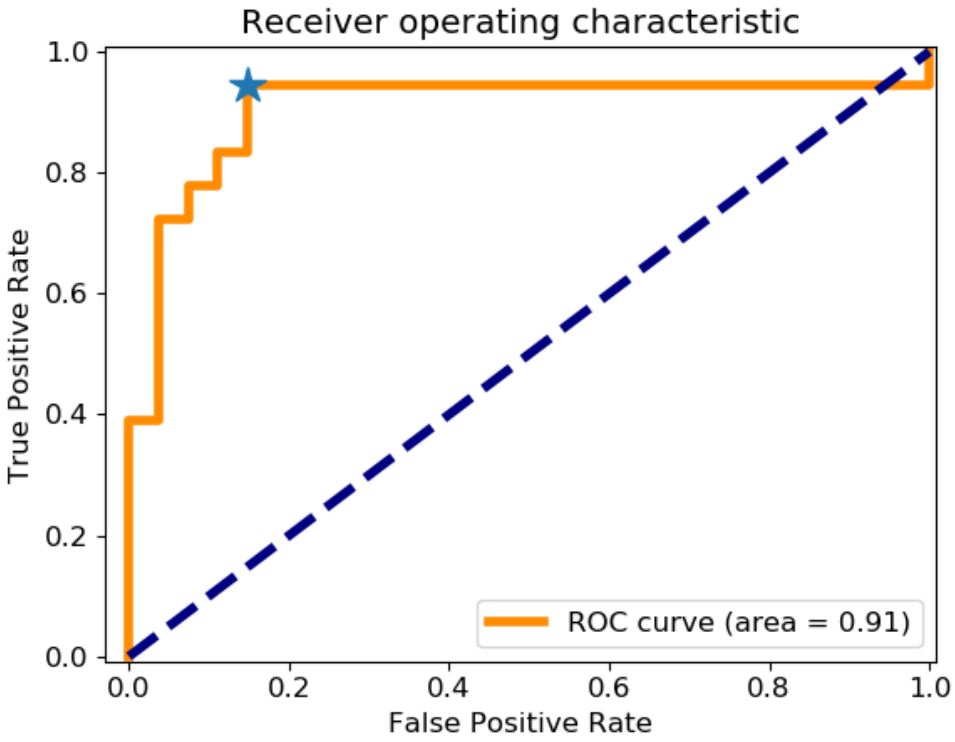

Fig. 7.8 The ROC analysis for the detection of ischaemia on a per-patient level.

With the inclusion of patients with MVD, the ability of quantitative stress perfusion CMR to detect patients with myocardial ischaemia is good, as demonstrated by the ROC curve in Figure 7.8. The AUC of the ROC analysis was 0.91. The optimal threshold for detecting ischaemia was 1.34 ml/min/g. This threshold gave a sensitivity of 94.4%, a specificity of 85.2% and an overall diagnostic accuracy of 86.7%.

If only the patients with anatomically smooth coronary vessels are included, it gives a realistic clinical setting to test if quantitative stress CMR can distinguish between CAD- and MVD patients. The ROC analysis for this situation is shown in Figure 7.9. The AUC is 0.91, sensitivity is 100% and specificity of 71.7% so that the overall diagnostic accuracy is 85.7%. In the patients with MVD, the typical diffuse, sub-endocardial ischaemia is seen, particularly in the (systolic) mid-slice [110]. Examples of these patients are shown in Figures 7.10 and 7.11.

7.4 Discussion

This is a small proof of principle study to establish the feasibility of fully-automatic quantitative stress perfusion CMR using the methods presented in Chapters 4, 5, and 6. That is, it has

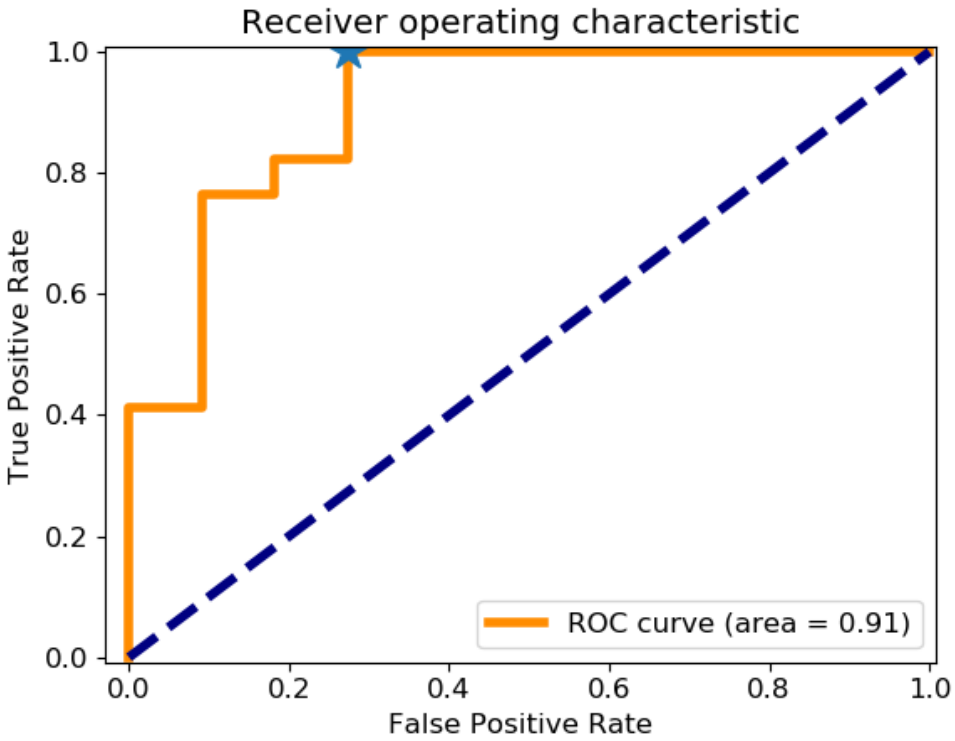

Fig. 7.9 The ROC analysis for the detection of MVD on a per-patient level.

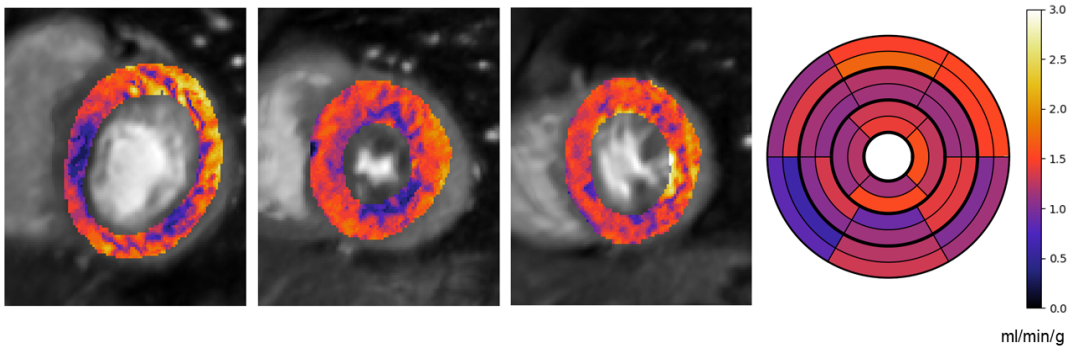

Fig. 7.10 Quantitative MBF maps and 32 segment representation for a MVD patient.

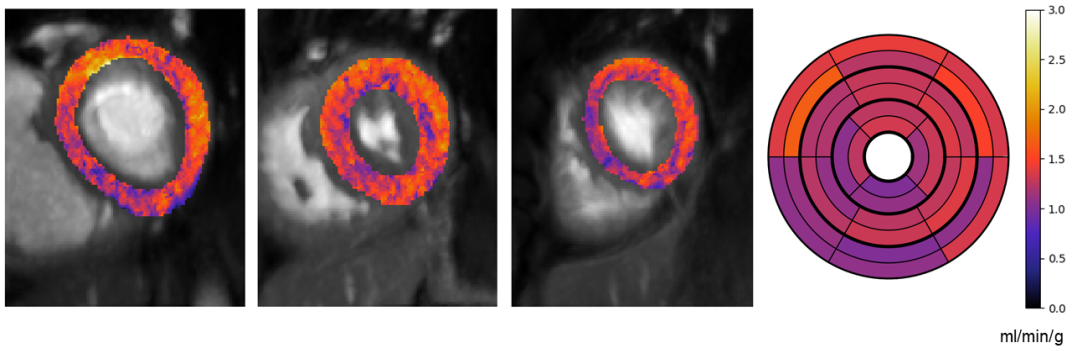

Fig. 7.11 Quantitative MBF maps and 32 segment representation for a MVD patient.

been shown that a stress perfusion CMR image series can be automatically processed, motion compensated, segmented, and tracer-kinetic models can be fit to automatically infer myocardial blood flow which has a high level of diagnostic accuracy for detecting CAD and MVD. It removes the subjectivity and laborious processing of the analysis. If these results are found to generalise well to larger and independent patient groups, this will really make the case for the widespread clinical adoption of stress perfusion CMR.

The diagnostic accuracy and even the cut-off threshold values found are very similar to recent, concurrently run, studies [82, 111]. The main advantage of this study is that it was the first to be truly automatic, including myocardial segmentation and disease classification.

There are, however, limitations to this work. Most notable are the small sample size and the comparison of the functional perfusion test to an anatomical reference standard. It is well discussed that the anatomical measurements do not always correlate well to their functional significance. Therefore, a follow-up study is warranted in which quantitative stress CMR is compared to appropriate reference standards: fractional and coronary flow reserve.

There is also further future work required. This study was conducted with dual-bolus acquisitions, methods for dual-sequence acquisitions are now becoming available and should ease the workflow of future studies [58] but the different acquisition may need different cut-off thresholds. The diagnostic accuracy could also benefit from future developments. While the per-patient diagnostic accuracy is very high, this drops significantly when assessing which vessels are diseased. A physiological cause of this may be some microvascular dysfunction causing ischaemia in the remote territories of patients with CAD leading to false positives. It is also likely a consequence of the limitations of the segmental analysis. Small areas of ischaemia may be averaged out making a segment to be a false negative. False positives are also possible when the area of ischaemia extends into the neighbouring territory. Two examples of patients with these characteristics are shown in Figure 7.12. The patient on the left has a single RCA lesion and the patient on the right has LCx and LAD lesions. Despite the patient on

the left having disease in fewer vessels, they have more ischaemia and the amount of disease is over-estimated as the ischaemia extends into the LCx territory. On the right, the disease is not picked up as the ischaemic burden is not high enough. However, the diagnosis would be clear to a visual reader based on this quantitative maps and the use of machine learning classifiers to mimic this may lead to more refined diagnoses. The ability detect CAD from CAD- patients and MVD from CAD- is shown but the ultimate aim would be to be able to distinguish the three groups from each other and this may benefit from a similar machine learning classifier.

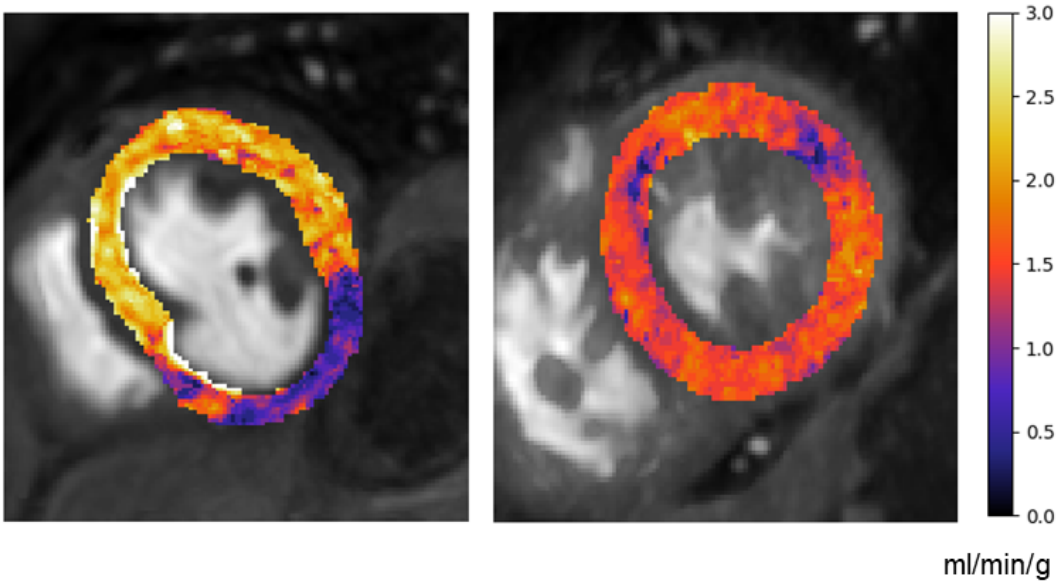

Fig. 7.12 Example MBF maps from two patients. The patient on the left has extensive ischaemia arising from disease in one vessel. The patient on the left has two vessel disease but much less ischaemia. This did not reach the derived threshold for CAD and is misclassified.

Chapter 8

Conclusion

8.1 Thesis summary

This thesis has dealt with the challenging problem of myocardial perfusion quantification from stress perfusion CMR images. Myocardial perfusion CMR is a powerful diagnostic tool for coronary artery disease and has the potential to play a big role in the management of patients with microvascular dysfunction. It has been, so far, limited by the difficulty of interpreting the images (as well as factors such as the lack of availability, and the problem of reimbursement in the United States). Quantitative stress perfusion CMR is potentially the solution to this as it is not subjective and thus requires less expertise.

This idea is not new and perfusion quantification has been an active research topic for many years [112]. A major drawback of all these early solutions, however, was that they required a lot of manual processing, such as segmenting the AIF, segmenting the myocardium, and motion compensation. Biglands et al. [81] reported that it took roughly one hour per patient to manually correct the myocardial contours for motion. This level of manual interaction is clearly not feasible on a routine basis in the clinic. Furthermore, the reliability of the analysis, particularly the model fitting [6, 55], has been often questioned. This motivated the aim of this thesis, which was to make the analysis fast, automatic, and more reliable. This work has led to a solution for quantitative stress perfusion CMR that is robust and truly automated.

Chapter 4 presented an approach for the compensation of respiratory motion which often precludes accurate quantification. Motion compensation is particularly challenging in DCE-MRI as it uses saturation recovery sequences and injections of contrast boluses. The contrast bolus passes rapidly through the region of interest leaving a series of time dynamics with very different levels and regions of contrast enhancement. As traditional image registration approaches assume there is a constant mapping between anatomical regions and signal intensity values, this assumption is invalidated by the passing contrast. Outside of where and when

the contrast is passing, the signal is saturated. With little signal to work with, intensity-based registrations are sensitive to noise and subject to failing.

The data decomposition technique robust PCA is shown to be able to separate the dynamic contrast-enhancement from the baseline anatomical signal. The rigid motion can then be estimated in the absence of the dynamic contrast-enhancement and subsequently applied to the original image series. The remaining motion appears to be noise-like and can be removed using a PCA-decomposition and the image series can again be registered to the de-noised motionless synthetic image series to remove any remaining motion. It is well documented that the validation of image registrations is challenging [113], in this work the quantitative evaluation is based on assumptions about motionless image series. It is shown that the time-intensity curves evolve more smoothly and that the rest perfusion maps show more spatial homogeneity after motion compensation. Perhaps more telling is that expert readers visually scored the quality of the motion compensation higher than the state-of-the-art approach.

In Chapter 5, the first deep learning-based pipeline for stress perfusion CMR was described. This leverages the huge advances made in computer vision and image processing, based on convolutional neural networks, to give a previously unseen level of automation to the processing. The pipeline seeks to mimic how a manual operator would have processed the data in the past. A first CNN picks the time dynamic with maximum contrast and this image is then fed to a further network which computes a bounding box around the LV and myocardium. Motion compensation is then performed within this bounding box. The resulting image series is finally segmented and the RV insertion point is detected. The training labels were produced by expert operators with a vast amount of experience in perfusion quantification. The algorithms were validated against labels from the same operators on the held-out test set. The automated deep learning approach was shown to closely match the expert labels at all stages. Most importantly, there was also a good agreement between the derived MBF values from both the automated and manual systems.

Chapter 6 aimed to improve the reliability of the kinetic parameters being inferred. This was done by enforcing well-known and physiological prior information. In particular, the knowledge that neighbouring pixels are likely to have similar kinetics was exploited. This prior information can be naturally included in a Bayesian inference framework and was combined with probabilistic constraints to ensure the estimated parameters were within physiological ranges. Since ground-truth kinetic values are not available *in vivo*, this was first validated in a series of simulated studies and shown to outperform the traditional non-linear least squares fitting estimates. Visually, the parameters estimated with Bayesian inference in patients outperformed the least-squares parameters and in a small cohort they were shown to match the clinical assessment of the patients.

The main validation for the combined approaches from Chapters 4, 5, and 6 comes in Chapter 7. Here it is shown, in a cohort of 47 patients that the automatically derived quantitative MBF values can diagnose CAD and in the setting of patient with smooth coronary arteries, it can diagnose coronary MVD. As discussed, this study is somewhat limited and a follow-up study in a larger cohort versus a functional marker, such as FFR, is warranted.

8.2 Context

Stress perfusion CMR has undoubted high diagnostic accuracy [2] and has outperformed SPECT in randomised trials [3]. It has been shown to have high prognostic value and be cost-effective [29]. Perhaps most importantly, the results of MR-INFORM [4] showed that it is non-inferior to invasive FFR measurements for the management of patients [4]. Additional advantages over the alternative nuclear perfusion imaging techniques are the higher spatial resolution and lack of ionising radiation. Thus, it should play a significant role in the management of patients with suspected CAD. The use of stress perfusion CMR should only benefit from the analysis being made easier and less subjective.

This works comes at an important time. Through-out the last 20 years there has been a trend away from anatomical imaging towards functional assessments of CAD. This trend made sense based on the intuition that there must be demonstrable ischaemia for a patient to benefit from being revascularised. It also seemed to be backed up by the FAME I and FAME II trials which showed better outcomes for patients guided by functional or ischaemia tests [114, 115].

However, recently, anatomical imaging has undergone a resurgence based on the results of the PROMISE trial [116] (and followed-up by the SCOT-HEART trial [117]) which showed that patients can be equally well managed by anatomical CCTA imaging. This resurgence has been accelerated by the (mis-)interpretation of the results of the ISCHEMIA trial [118]. Despite the fact that the trial was designed to compare invasive interventions versus optimal medical therapy and not to compare imaging tests, it was reported that there was no correlation between ischaemia and benefit from revascularisation. It is important to observe that the ISCHEMIA used local reads for the stress tests. As discussed extensively in this thesis, the diagnostic accuracy of stress imaging tests falls dramatically outside of highly experienced centres and this is likely to have impacted the results. This is clearly an area where emerging technology, such as quantitative perfusion CMR, has the potential to add real value. Furthermore, the use of CCTA in ISCHEMIA to exclude left main disease has led to it being marketed as the first in line imaging test for CAD. This is all in spite of CCTA only being able to reliably rule out CAD and not having a positive predictive value, as it does not infer the presence of ischaemia.

Finally, a further major advantage of ischaemia testing over anatomical imaging is in patients that present with anatomically smooth coronary arteries and angina, from microvascular dysfunction. MVD causes ischaemia [106] and as was shown in this thesis, there is a role for ischaemia imaging in these patients. The quantitative analysis may finally allow these patients to be managed on the basis of a non-invasive test.

8.3 Future work

The methods presented in this thesis represent a significant improvement on methods previously used in the field. The robust motion compensation alleviates one of the significant challenges and automated processing makes it more accessible. This is the first deep learning system for stress perfusion CMR, though more are now becoming available [119]. However, there are still opportunities for future work in the field. As discussed, the output of the quantification would be a suitable input for a further machine learning classifier for disease classification and staging. This would circumnavigate the discussed limitations of the AHA segment model. A limitation of the proposed methods is the processing time taken for the analysis, the image registration and Bayesian inference are computationally intensive. These steps could be replaced with deep learning systems [120] which are quicker to deploy on new data.

The power of deep learning could be utilised in a range of other tasks from which the analysis would benefit. This includes the image reconstruction, to allow images to be acquired faster, and super resolution algorithms to increase both the in-plane spatial resolution and the LV coverage. There has also been a recent interest in developing quality control measures for automated processing systems [121, 122]. The system presented in this thesis is not infallible and would benefit from an assessment of image quality prior to processing and a method to detect failed cases.

In conclusion, while this work has laid the foundations of fully automatic quantitative stress perfusion CMR, much more work can be done to make the analysis more accurate, reliable, and fast. This further work will likely leverage the tremendous improvements in image processing made possible by advances in machine learning. The results presented, and in the literature, are promising, but in the end trials will be needed to validate it, preferably including less specialised centres.

References

[1] G. Montalescot, U. Sechtem, S. Achenbach, F. Andreotti, C. Arden, A. Budaj, R. Bugiardini, F. Crea, T. Cuisset, C. Di Mario, J. R. Ferreira, B. J. Gersh, A. K. Gitt, J.-S. Hulot, N. Marx, L. H. Opie, M. Pfisterer, E. Prescott, F. Ruschitzka, M. Sabaté, R. Senior, D. P. Taggart, E. E. van der Wall, C. J. Vrints, J. L. Zamorano, S. Achenbach, H. Baumgartner, J. J. Bax, H. Bueno, V. Dean, C. Deaton, C. Erol, R. Fagard, R. Ferrari, D. Hasdai, A. W. Hoes, P. Kirchhof, J. Knuuti, P. Kolh, P. Lancellotti, A. Linhart, P. Nihoyannopoulos, M. F. Piepoli, P. Ponikowski, P. A. Sirnes, J. L. Tamargo, M. Tendera, A. Torbicki, W. Wijns, S. Windecker, J. Knuuti, M. Valgimigli, H. Bueno, M. J. Claeys, N. Donner-Banzhoff, C. Erol, H. Frank, C. Funck-Brentano, O. Gaemperli, J. R. Gonzalez-Juanatey, M. Hamilos, D. Hasdai, S. Husted, S. K. James, K. Kervinen, P. Kolh, S. D. Kristensen, P. Lancellotti, A. P. Maggioni, M. F. Piepoli, A. R. Pries, F. Romeo, L. Rydén, M. L. Simoons, P. A. Sirnes,, "2013 ESC guidelines on the management of stable coronary artery disease," *European Heart Journal*, vol. 34, no. 38, pp. 2949–3003, 2013.

[2] J. P. Greenwood, N. Maredia, J. F. Younger, J. M. Brown, J. Nixon, C. C. Everett, P. Bijsterveld, J. P. Ridgway, A. Radjenovic, C. J. Dickinson, S. G. Ball, and S. Plein, "Cardiovascular magnetic resonance and single-photon emission computed tomography for diagnosis of coronary heart disease (CE-MARC): a prospective trial," *The Lancet*, vol. 379, no. 9814, pp. 453–460, 2012.

[3] J. Schwitter, C. M. Wacker, N. Wilke, N. Al-Saadi, E. Sauer, K. Huettle, S. O. Schönberg, A. Luchner, O. Strohm, H. Ahlstrom, T. Dill, N. Hoebel, T. Simor, and M.-I. Investigators, "MR-IMPACT II: Magnetic Resonance Imaging for Myocardial Perfusion Assessment in Coronary artery disease Trial: perfusion-cardiac magnetic resonance vs. single-photon emission computed tomography for the detection of coronary artery disease: a comparative," *European heart journal*, vol. 34, no. 10, pp. 775–781, 2013.

[4] E. Nagel, J. P. Greenwood, G. P. McCann, N. Bettencourt, A. M. Shah, S. T. Hussain, D. Perera, S. Plein, C. Bucciarelli-Ducci, M. Paul, M. A. Westwood, M. Marber, W.-S. Richter, V. O. Puntmann, C. Schwenke, J. Schulz-Menger, R. Das, J. Wong, D. J. Hausenloy, H. Steen, and C. Berry, "Magnetic Resonance Perfusion or Fractional Flow Reserve in Coronary Disease," *New England Journal of Medicine*, 2019.

[5] A. D. M. Villa, L. Corsinovi, I. Ntalas, X. Milidonis, C. Scannell, G. Di Giovine, N. Child, C. Ferreira, M. S. Nazir, J. Karady, E. Eshja, V. De Francesco, N. Bettencourt, A. Schuster, T. F. Ismail, R. Razavi, and A. Chiribiri, "Importance of operator training

and rest perfusion on the diagnostic accuracy of stress perfusion cardiovascular magnetic resonance," *Journal of Cardiovascular Magnetic Resonance*, vol. 20, no. 1, p. 74, 2018.

[6] D. L. Buckley, "Uncertainty in the analysis of tracer kinetics using dynamic contrast-enhanced T1-weighted MRI," *Magnetic Resonance in Medicine*, vol. 47, no. 3, pp. 601–606, 2002.

[7] J. R. Levick, *An Introduction to Cardiovascular Physiology*. London: Hodder Arnold, 5th ed., 2010.

[8] "Wikipedia." https://en.wikipedia.org/wiki/File:Heart_diagram-en.svg. Accessed: 10-04-2020.

[9] "Wikipedia." https://en.wikipedia.org/wiki/Cardiac_muscle. Accessed: 10-04-2020.

[10] E. O. Feigl, "Coronary physiology," 1983.

[11] R. E. Klabunde, "Cardiovascular physiology concepts, coronary anatomy and blood flow." https://www.cvphysiology.com/Blood%20Flow/BF001. Accessed: 10-04-2020.

[12] "Wikipedia." https://en.wikipedia.org/wiki/Coronary_artery_ectasia. Accessed: 10-04-2020.

[13] R. E. Klabunde, "Cardiovascular physiology concepts, autoregulation of organ blood flow." https://www.cvphysiology.com/Blood%20Flow/BF004. Accessed: 10-04-2020.

[14] R. E. Klabunde, "Cardiovascular physiology concepts, metabolic mechanisms of vasodilation." https://www.cvphysiology.com/Blood%20Flow/BF008. Accessed: 10-04-2020.

[15] "World health organization." https://www.who.int/en/news-room/fact-sheets/detail/cardiovascular-diseases-(cvds). Accessed: 17-04-2020.

[16] J.-M. R. Detry, "The pathophysiology of myocardial ischaemia," *European Heart JournalEur Heart J*, vol. 17, no. 17, pp. 48–52, 1996.

[17] A. Ansari and J. Puthumana, "The "Ischemic Cascade"," in *Echocardiography in Acute Coronary Syndrome*, pp. 149–160, London: Springer London, 2009.

[18] R. E. Klabunde, "Cardiovascular physiology concepts, electrophysiological changes during cardiac ischemia." https://www.cvphysiology.com/CAD/CAD012. Accessed: 17-04-2020.

[19] R. E. Klabunde, "Cardiovascular physiology concepts, myocardial infaction." https://www.cvphysiology.com/CAD/CAD010. Accessed: 17-04-2020.

[20] S. D. Fihn, J. M. Gardin, J. Abrams, K. Berra, J. C. Blankenship, A. P. Dallas, P. S. Douglas, J. M. Foody, T. C. Gerber, A. L. Hinderliter, S. B. King, P. D. Kligfield, H. M. Krumholz, R. Y. Kwong, M. J. Lim, J. A. Linderbaum, M. J. MacK, M. A. Munger, R. L.

Prager, J. F. Sabik, L. J. Shaw, J. D. Sikkema, C. R. Smith, S. C. Smith, J. A. Spertus, and S. V. Williams, "2012 ACCF/AHA/ACP/AATS/PCNA/SCAI/STS guideline for the diagnosis and management of patients with stable ischemic heart diseass," *Circulation*, vol. 126, no. 25, 2012.

[21] D. L. Mann, D. P. Zipes, P. Libby, R. O. Bonow, and E. Braunwald, *Braunwald's heart disease: A textbook of cardiovascular medicine*. Philadelphia, PA: Elsevier/Saunders, tenth ed., 2015.

[22] R. Votavová, A. Linhartová, J. Kořínek, J. Marek, and A. Linhart, "Echocardiography in coronary artery disease," *Cor et Vasa*, vol. 57, no. 6, pp. e408–e418, 2015.

[23] G. A. Beller and R. C. Heede, "SPECT Imaging for Detecting Coronary Artery Disease and Determining Prognosis by Noninvasive Assessment of Myocardial Perfusion and Myocardial Viability," *Journal of Cardiovascular Translational Research*, vol. 4, no. 4, pp. 416–424, 2011.

[24] J. D. Schuijf, L. J. Shaw, W. Wijns, H. J. Lamb, D. Poldermans, A. de Roos, E. E. van der Wall, and J. J. Bax, "Cardiac imaging in coronary artery disease: differing modalities.," *Heart (British Cardiac Society)*, vol. 91, no. 8, pp. 1110–7, 2005.

[25] A. J. Moss, M. C. Williams, D. E. Newby, and E. D. Nicol, "The Updated NICE Guidelines: Cardiac CT as the First-Line Test for Coronary Artery Disease," 2017.

[26] R. T. George, A. Arbab-Zadeh, J. M. Miller, K. Kitagawa, H. J. Chang, D. A. Bluemke, L. Becker, O. Yousuf, J. Texter, A. C. Lardo, and J. A. Lima, "Adenosine stress 64-and 256-row detector computed tomography angiography and perfusion imaging a pilot study evaluating the transmural extent of perfusion abnormalities to predict atherosclerosis causing myocardial ischemia," *Circulation: Cardiovascular Imaging*, vol. 2, no. 3, pp. 174–182, 2009.

[27] M. Dewey, M. Siebes, M. Kachelrieß, K. F. Kofoed, P. Maurovich-Horvat, K. Nikolaou, W. Bai, A. Kofler, R. Manka, S. Kozerke, A. Chiribiri, T. Schaeffter, F. Michallek, F. Bengel, S. Nekolla, P. Knaapen, M. Lubberink, R. Senior, M.-X. Tang, J. J. Piek, T. van de Hoef, J. Martens, L. Schreiber, and o. b. o. t. Q. C. I. S. Group, "Clinical quantitative cardiac imaging for the assessment of myocardial ischaemia," *Nature Reviews Cardiology*, 2020.

[28] J. P. Greenwood, D. P. Ripley, C. Berry, G. P. McCann, S. Plein, C. Bucciarelli-Ducci, E. D. Armellina, A. Prasad, P. Bijsterveld, J. R. Foley, K. Mangion, M. Sculpher, S. Walker, C. C. Everett, D. A. Cairns, L. D. Sharples, and J. M. Brown, "Effect of care guided by cardiovascular magnetic resonance, myocardial perfusion scintigraphy, or NICE guidelines on subsequent unnecessary angiography rates :The CE-MARC 2 randomized clinical trial," *JAMA - Journal of the American Medical Association*, vol. 316, no. 10, pp. 1051–1060, 2016.

[29] R. Y. Kwong, Y. Ge, K. Steel, S. Bingham, S. Abdullah, K. Fujikura, W. Wang, A. Pandya, Y.-Y. Chen, J. R. Mikolich, S. Boland, A. E. Arai, W. P. Bandettini, S. M. Shanbhag, A. R. Patel, A. Narang, A. Farzaneh-Far, B. Romer, J. F. Heitner, J. Y. Ho, J. Singh, C. Shenoy, A. Hughes, S. W. Leung, M. Marji, J. A. Gonzalez, S. Mehta, D. J. Shah, D. Debs, S. V. Raman, A. Guha, V. A. Ferrari, J. Schulz-Menger, R. Hachamovitch, M. Stuber, and O. P. Simonetti, "Cardiac Magnetic Resonance Stress Perfusion Imaging for Evaluation of Patients With Chest Pain," *Journal of the American College of Cardiology*, vol. 74, no. 14, pp. 1741 LP – 1755, 2019.

[30] C. M. Kramer, "Integrated approach to ischemic heart disease. The one-stop shop.," *Cardiology clinics*, vol. 16, no. 2, pp. 267–276, 1998.

[31] A. Bustin, I. Rashid, G. Cruz, R. Hajhosseiny, T. Correia, R. Neji, R. Rajani, T. F. Ismail, R. M. Botnar, and C. Prieto, "3D whole-heart isotropic sub-millimeter resolution coronary magnetic resonance angiography with non-rigid motion-compensated PROST," *Journal of Cardiovascular Magnetic Resonance*, vol. 22, no. 1, p. 24, 2020.

[32] E. C. Sammut, A. D. Villa, G. Di Giovine, L. Dancy, F. Bosio, T. Gibbs, S. Jeyabraba, S. Schwenke, S. E. Williams, M. Marber, K. Alfakih, T. F. Ismail, R. Razavi, and A. Chiribiri, "Prognostic Value of Quantitative Stress Perfusion Cardiac Magnetic Resonance," *JACC: Cardiovascular Imaging*, 2017.

[33] K. D. Knott, A. Seraphim, J. B. Augusto, H. Xue, L. Chacko, N. Aung, S. E. Petersen, J. A. Cooper, C. Manisty, A. N. Bhuva, T. Kotecha, C. V. Bourantas, R. H. Davies, L. A. Brown, S. Plein, M. Fontana, P. Kellman, and J. C. Moon, "The Prognostic Significance of Quantitative Myocardial Perfusion: An Artificial Intelligence Based Approach Using Perfusion Mapping," *Circulation*, 2020.

[34] D. J. Atkinson, D. Burstein, and R. R. Edelman, "First-pass cardiac perfusion: evaluation with ultrafast MR imaging.," *Radiology*, vol. 174, no. 3 Pt 1, pp. 757–62, 1990.

[35] B. L. Gerber, S. V. Raman, K. Nayak, F. H. Epstein, P. Ferreira, L. Axel, and D. L. Kraitchman, "Journal of Cardiovascular Magnetic Resonance Cardiovascular magnetic resonance features of caseous calcification of the mitral annulus," *Journal of Cardiovascular Magnetic Resonance*, vol. 5, no. Lv, pp. 1–5, 2008.

[36] M. Salerno and G. A. Beller, "Noninvasive assessment of myocardial perfusion," *Circulation: Cardiovascular Imaging*, vol. 2, no. 5, pp. 412–424, 2009.

[37] D. A. Broadbent, J. D. Biglands, D. P. Ripley, D. M. Higgins, J. P. Greenwood, S. Plein, and D. L. Buckley, "Sensitivity of quantitative myocardial dynamic contrast-enhanced MRI to saturation pulse efficiency, noise and t ₁ measurement error: Comparison of nonlinearity correction methods," *Magnetic Resonance in Medicine*, vol. 75, no. 3, pp. 1290–1300, 2016.

[38] S. Plein, J. Greenwood, and J. P. Ridgway, *Cardiovascular MR Manual*. Springer, second ed., 2015.

[39] A. Lupi, A. Buffon, M. L. Finocchiaro, E. Conti, A. Maseri, and F. Crea, "Mechanisms of adenosine-induced epicardial coronary artery dilatation," *European Heart Journal*, vol. 18, no. 4, pp. 614–617, 1997.

[40] D. R. Messroghli, G. J. Bainbridge, K. Alfakih, T. R. Jones, S. Plein, J. P. Ridgway, and M. U. Sivananthan, "Assessment of regional left ventricular function: Accuracy and reproducibility of positioning standard short-axis sections in cardiac MR imaging," *Radiology*, vol. 235, no. 1, pp. 229–236, 2005.

[41] P. Kellman and A. E. Arai, "Imaging Sequences for First Pass Perfusion—A Review," *Journal of Cardiovascular Magnetic Resonance*, vol. 9, pp. 525–537, 2007.

[42] R. Jogiya, S. Kozerke, G. Morton, K. De Silva, S. Redwood, D. Perera, E. Nagel, and S. Plein, "Validation of dynamic 3-dimensional whole heart magnetic resonance myocardial perfusion imaging against fractional flow reserve for the detection of significant coronary artery disease," *Journal of the American College of Cardiology*, vol. 60, no. 8, pp. 756–765, 2012.

[43] M. S. Nazir, R. Neji, P. Speier, F. Reid, D. Stäb, M. Schmidt, C. Forman, R. Razavi, S. Plein, T. F. Ismail, A. Chiribiri, and S. Roujol, "Simultaneous multi slice (SMS) balanced steady state free precession first-pass myocardial perfusion cardiovascular magnetic resonance with iterative reconstruction at 1.5 T," *Journal of Cardiovascular Magnetic Resonance*, vol. 20, no. 1, pp. 1–11, 2018.

[44] H. P. Do, V. Ramanan, X. Qi, J. Barry, G. A. Wright, N. R. Ghugre, and K. S. Nayak, "Non-contrast assessment of microvascular integrity using arterial spin labeled cardiovascular magnetic resonance in a porcine model of acute myocardial infarction," *Journal of Cardiovascular Magnetic Resonance*, vol. 20, no. 1, p. 45, 2018.

[45] R. Manka, I. Paetsch, B. Schnackenburg, R. Gebker, E. Fleck, and C. Jahnke, "BOLD cardiovascular magnetic resonance at 3.0 tesla in myocardial ischemia.," *Journal of cardiovascular magnetic resonance : official journal of the Society for Cardiovascular Magnetic Resonance*, vol. 12, no. 1, p. 54, 2010.

[46] A. F. Members, S. Windecker, P. Kolh, F. Alfonso, J.-P. Collet, J. Cremer, V. Falk, G. Filippatos, C. Hamm, S. J. Head, P. Jüni, A. P. Kappetein, A. Kastrati, J. Knuuti, U. Landmesser, G. Laufer, F.-J. Neumann, D. J. Richter, P. Schauerte, M. Sousa Uva, G. G. Stefanini, D. P. Taggart, L. Torracca, M. Valgimigli, W. Wijns, A. Witkowski, E. S. C. C. f. P. Guidelines, J. L. Zamorano, S. Achenbach, H. Baumgartner, J. J. Bax, H. Bueno, V. Dean, C. Deaton, Ç. Erol, R. Fagard, R. Ferrari, D. Hasdai, A. W. Hoes, P. Kirchhof, J. Knuuti, P. Kolh, P. Lancellotti, A. Linhart, P. Nihoyannopoulos, M. F. Piepoli, P. Ponikowski, P. A. Sirnes, J. L. Tamargo, M. Tendera, A. Torbicki, W. Wijns, S. Windecker, E. C. G. Committee, M. Sousa Uva, D. Reviewers, S. Achenbach, J. Pepper, A. Anyanwu, L. Badimon, J. Bauersachs, A. Baumbach, F. Beygui, N. Bonaros, M. De Carlo, C. Deaton, D. Dobrev, J. Dunning, E. Eeckhout, S. Gielen, D. Hasdai, P. Kirchhof, H. Luckraz, H. Mahrholdt, G. Montalescot, "2014 ESC/EACTS Guidelines

on myocardial revascularization: The Task Force on Myocardial Revascularization of the European Society of Cardiology (ESC) and the European Association for Cardio-Thoracic Surgery (EACTS)Developed with the special contribution o," *European Heart Journal*, vol. 35, no. 37, pp. 2541–2619, 2014.

[47] L. Bokacheva, H. Rusinek, Q. Chen, N. Oesingmann, C. Prince, M. Kaur, E. Kramer, and V. S. Lee, "Quantitative determination of Gd-DTPA concentration in T 1-weighted MR renography studies," *Magnetic Resonance in Medicine*, vol. 57, no. 6, pp. 1012–1018, 2007.

[48] M. Ishida, A. Schuster, G. Morton, A. Chiribiri, S. Hussain, M. Paul, N. Merkle, H. Steen, D. Lossnitzer, B. Schnackenburg, K. Alfakih, S. Plein, and E. Nagel, "Development of a universal dual-bolus injection scheme for the quantitative assessment of myocardial perfusion cardiovascular magnetic resonance.," *Journal of cardiovascular magnetic resonance : official journal of the Society for Cardiovascular Magnetic Resonance*, vol. 13, p. 28, 2011.

[49] S. P. Sourbron and D. L. Buckley, "Tracer kinetic modelling in MRI: estimating perfusion and capillary permeability," *Physics in Medicine and Biology*, vol. 57, no. 2, pp. R1–R33, 2011.

[50] S. P. Sourbron and D. L. Buckley, "Classic models for dynamic contrast-enhanced MRI," *NMR in Biomedicine*, vol. 26, no. 8, pp. 1004–1027, 2013.

[51] M. Jerosch-herold, "Quantification of myocardial perfusion by cardiovascular magnetic resonance," *Journal of Cardiovascular Magnetic Resonance*, vol. 12, no. 57, pp. 1–16, 2010.

[52] T. S. Ahearn, R. T. Staff, T. W. Redpath, and S. I. Semple, "The use of the Levenberg-Marquardt curve-fitting algorithm in pharmacokinetic modelling of DCE-MRI data," *Physics in Medicine and Biology*, vol. 50, no. 9, pp. N85–N92, 2005.

[53] D. W. Marquardt, "An Algorithm for Least-Squares Estimation of Nonlinear Parameters," *Journal of the Society for Industrial and Applied Mathematics*, vol. 11, no. 2, pp. 431–441, 1963.

[54] M. Jerosch-Herold, C. Swingen, and R. T. Seethamraju, "Myocardial blood flow quantification with MRI by model-independent deconvolution.," *Medical physics*, vol. 29, no. 5, pp. 886–897, 2002.

[55] D. Likhite, P. Suksaranjit, G. Adluru, B. Wilson, and E. DiBella, "Estimating extraction fraction and blood flow by combining first-pass myocardial perfusion and T1 mapping results," *Quantitative Imaging in Medicine and Surgery*, vol. 7, no. 5, pp. 480–495, 2017.

[56] M. T. Le, N. Zarinabad, T. D'Angelo, I. Mia, R. Heinke, T. J. Vogl, A. Zeiher, E. Nagel, and V. O. Puntmann, "Sub-segmental quantification of single (stress)-pass perfusion CMR improves the diagnostic accuracy for detection of obstructive coronary artery disease," *Journal of Cardiovascular Magnetic Resonance*, vol. 22, no. 1, p. 14, 2020.

[57] F. Calamante, D. G. Gadian, and A. Connelly, "Delay and dispersion effects in dynamic susceptibility contrast MRI: Simulations using singular value decomposition," *Magnetic Resonance in Medicine*, vol. 44, no. 3, pp. 466–473, 2000.

[58] J. Sánchez-González, R. Fernandez-Jiménez, N. D. Nothnagel, G. López-Martín, V. Fuster, and B. Ibañez, "Optimization of dual-saturation single bolus acquisition for quantitative cardiac perfusion and myocardial blood flow maps," *Journal of Cardiovascular Magnetic Resonance*, vol. 17, no. 1, p. 21, 2015.

[59] J. D. Biglands, D. R. Magee, S. P. Sourbron, S. Plein, J. P. Greenwood, and A. Radjenovic, "Comparison of the Diagnostic Performance of Four Quantitative Myocardial Perfusion Estimation Methods Used in Cardiac MR Imaging: CE-MARC Substudy," *Radiology*, vol. 275, no. 2, pp. 393–402, 2015.

[60] L. Y. Hsu, D. W. Groves, A. H. Aletras, P. Kellman, and A. E. Arai, "A quantitative pixel-wise measurement of myocardial blood flow by contrast-enhanced first-pass CMR perfusion imaging: Microsphere validation in dogs and feasibility study in humans," *JACC: Cardiovascular Imaging*, vol. 5, no. 2, pp. 154–166, 2012.

[61] G. Morton, A. Chiribiri, M. Ishida, S. T. Hussain, A. Schuster, A. Indermuehle, D. Perera, J. Knuuti, S. Baker, E. Hedström, P. Schleyer, M. O'Doherty, S. Barrington, and E. Nagel, "Quantification of Absolute Myocardial Perfusion in Patients With Coronary Artery Disease: Comparison Between Cardiovascular Magnetic Resonance and Positron Emission Tomography," *Journal of the American College of Cardiology*, vol. 60, no. 16, pp. 1546–1555, 2012.

[62] A. Schuster, M. Sinclair, N. Zarinabad, M. Ishida, J. P. Van Den Wijngaard, M. Paul, P. Van Horssen, S. T. Hussain, D. Perera, T. Schaeffter, J. A. Spaan, M. Siebes, E. Nagel, and A. Chiribiri, "A quantitative high resolution voxel-wise assessment of myocardial blood flow from contrast-enhanced first-pass magnetic resonance perfusion imaging: microsphere validation in a magnetic resonance compatible free beating explanted pig heart model," *European Heart Journal Cardiovascular Imaging*, vol. 16, no. 10, pp. 1082–1092, 2015.

[63] P. D. Gatehouse, A. G. Elkington, N. A. Ablitt, G.-Z. Yang, D. J. Pennell, and D. N. Firmin, "Accurate assessment of the arterial input function during high-dose myocardial perfusion cardiovascular magnetic resonance," *Journal of Magnetic Resonance Imaging*, vol. 20, no. 1, pp. 39–45, 2004.

[64] P. Kellman, M. S. Hansen, S. Nielles-Vallespin, J. Nickander, R. Themudo, M. Ugander, and H. Xue, "Myocardial perfusion cardiovascular magnetic resonance: optimized dual sequence and reconstruction for quantification," *Journal of Cardiovascular Magnetic Resonance*, vol. 19, no. 1, p. 43, 2017.

[65] J. K. Mendes, G. Adluru, D. Likhite, M. J. Fair, P. D. Gatehouse, Y. Tian, A. Pedgaonkar, B. Wilson, and E. V. R. DiBella, "Quantitative 3D myocardial perfusion with an efficient

arterial input function," *Magnetic Resonance in Medicine*, vol. 83, no. 6, pp. 1949–1963, 2020.

[66] E. Nagel, C. Klein, I. Paetsch, S. Hettwer, B. Schnackenburg, K. Wegscheider, and E. Fleck, "Magnetic resonance perfusion measurements for the noninvasive detection of coronary artery disease," *Circulation*, vol. 108, no. 4, pp. 432–437, 2003.

[67] T. Giang, D. Nanz, R. Coulden, M. Friedrich, M. Graves, N. Al-Saadi, T. Luscher, G. von Schulthess, and J. Schwitter, "Detection of coronary artery disease by magnetic resonance myocardial perfusion imaging with various contrast medium doses: first european multi-centre experience," *European Heart Journal*, vol. 25, no. 18, pp. 1657–1665, 2004.

[68] S. Plein, A. Radjenovic, J. P. Ridgway, D. Barmby, J. P. Greenwood, S. G. Ball, and M. U. Sivananthan, "Coronary artery disease: Myocardial perfusion MR imaging with sensitivity encoding versus conventional angiography," *Radiology*, vol. 235, no. 2, pp. 423–430, 2005.

[69] J. Rieber, A. Huber, I. Erhard, S. Mueller, M. Schweyer, A. Koenig, T. M. Schiele, K. Theisen, U. Siebert, S. O. Schoenberg, M. Reiser, and V. Klauss, "Cardiac magnetic resonance perfusion imaging for the functional assessment of coronary artery disease: a comparison with coronary angiography and fractional flow reserve," *European Heart Journal*, vol. 27, no. 12, pp. 1465–1471, 2006.

[70] J. Schwitter, D. Nanz, S. Kneifel, K. Bertschinger, M. Buechi, P. R. Knuesel, B. Marincek, T. F. Luescher, and G. K. von Schulthess, "Assessment of Myocardial Perfusion in Coronary Artery Disease by Magnetic Resonance," *Circulation*, vol. 103, no. 18, pp. 2230–2235, 2001.

[71] T. Ibrahim, S. G. Nekolla, K. Schreiber, K. Odaka, S. Volz, J. Mehilli, M. Güthlin, W. Delius, and M. Schwaiger, "Assessment of coronary flow reserve: Comparison between contrast-enhanced magnetic resonance imaging and positron emission tomography," *Journal of the American College of Cardiology*, vol. 39, no. 5, pp. 864–870, 2002.

[72] N. Al-Saadi, E. Nagel, M. Gross, A. Bornstedt, B. Schnackenburg, C. Klein, W. Klimek, H. Oswald, and E. Fleck, "Noninvasive Detection of Myocardial Ischemia From Perfusion Reserve Based on Cardiovascular Magnetic Resonance," *Circulation*, vol. 101, no. 12, pp. 1379–1383, 2000.

[73] F. E. Mordini, T. Haddad, L. Y. Hsu, P. Kellman, T. B. Lowrey, A. H. Aletras, W. P. Bandettini, and A. E. Arai, "Diagnostic accuracy of stress perfusion CMR in comparison with quantitative coronary angiography: Fully quantitative, semiquantitative, and qualitative assessment," *JACC: Cardiovascular Imaging*, vol. 7, no. 1, pp. 14–22, 2014.

[74] G. L. T. F. Hautvast, A. Chiribiri, T. Lockie, M. Breeuwer, E. Nagel, and S. Plein, "Quantitative analysis of transmural gradients in myocardial perfusion magnetic resonance images," *Magnetic Resonance in Medicine*, vol. 66, no. 5, pp. 1477–1487, 2011.

[75] A. Chiribiri, A. D. Villa, E. Sammut, M. Breeuwer, and E. Nagel, "Perfusion dyssynchrony analysis," *European heart journal cardiovascular Imaging*, vol. 17, no. 12, pp. 1414–1423, 2016.

[76] T. Fritz-Hansen, J. D. Hove, K. F. Kofoed, H. Kelbaek, and H. B. Larsson, "Quantification of MRI measured myocardial perfusion reserve in healthy humans: A comparison with positron emission tomography," *Journal of Magnetic Resonance Imaging*, vol. 27, no. 4, pp. 818–824, 2008.

[77] G. Morton, A. Chiribiri, M. Ishida, S. T. Hussain, A. Schuster, A. Indermuehle, D. Perera, J. Knuuti, S. Baker, E. Hedström, P. Schleyer, M. O'Doherty, S. Barrington, and E. Nagel, "Quantification of Absolute Myocardial Perfusion in Patients With Coronary Artery Disease," *Journal of the American College of Cardiology*, vol. 60, no. 16, pp. 1546–1555, 2012.

[78] C. A. Miller, J. H. Naish, M. P. Ainslie, C. Tonge, D. Tout, P. Arumugam, A. Banerji, R. M. Egdell, D. Clark, P. Weale, C. D. Steadman, G. P. McCann, S. G. Ray, G. J. Parker, and M. Schmitt, "Voxel-wise quantification of myocardial blood flow with cardiovascular magnetic resonance: Effect of variations in methodology and validation with positron emission tomography," *Journal of Cardiovascular Magnetic Resonance*, vol. 16, no. 1, pp. 1–15, 2014.

[79] T. Lockie, M. Ishida, D. Perera, A. Chiribiri, K. De Silva, S. Kozerke, M. Marber, E. Nagel, R. Rezavi, S. Redwood, and S. Plein, "High-resolution magnetic resonance myocardial perfusion imaging at 3.0-tesla to detect hemodynamically significant coronary stenoses as determined by fractional flow reserve," *Journal of the American College of Cardiology*, vol. 57, no. 1, pp. 70–75, 2010.

[80] G. Papanastasiou, M. C. Williams, M. R. Dweck, S. Alam, A. Cooper, S. Mirsadraee, D. E. Newby, and S. I. Semple, "Quantitative assessment of myocardial blood flow in coronary artery disease by cardiovascular magnetic resonance: Comparison of Fermi and distributed parameter modeling against invasive methods," *Journal of Cardiovascular Magnetic Resonance*, vol. 18, no. 1, p. 57, 2016.

[81] J. D. Biglands, M. Ibraheem, D. R. Magee, A. Radjenovic, S. Plein, and J. P. Greenwood, "Quantitative Myocardial Perfusion Imaging Versus Visual Analysis in Diagnosing Myocardial Ischemia: A CE-MARC Substudy," *JACC: Cardiovascular Imaging*, vol. 11, no. 5, pp. 711–718, 2018.

[82] L.-Y. Hsu, M. Jacobs, M. Benovoy, A. D. Ta, H. M. Conn, S. Winkler, A. M. Greve, M. Y. Chen, S. M. Shanbhag, W. P. Bandettini, and A. E. Arai, "Diagnostic Performance of Fully Automated Pixel-Wise Quantitative Myocardial Perfusion Imaging by Cardiovascular Magnetic Resonance," *JACC: Cardiovascular Imaging*, pp. 1–11, 2018.

[83] H. Xue, L. A. Brown, S. Nielles-Vallespin, S. Plein, and P. Kellman, "Automatic in-line quantitative myocardial perfusion mapping: Processing algorithm and implementation," *Magnetic Resonance in Medicine*, vol. 83, no. 2, pp. 712–730, 2020.

[84] H. Engblom, H. Xue, S. Akil, M. Carlsson, C. Hindorf, J. Oddstig, F. Hedeer, M. S. Hansen, A. H. Aletras, P. Kellman, and H. Arheden, "Fully quantitative cardiovascular magnetic resonance myocardial perfusion ready for clinical use: A comparison between cardiovascular magnetic resonance imaging and positron emission tomography," *Journal of Cardiovascular Magnetic Resonance*, vol. 19, no. 1, pp. 1–9, 2017.

[85] B. Pontre, B. R. Cowan, E. DiBella, S. Kulaseharan, D. Likhite, N. Noorman, L. Tautz, N. Tustison, G. Wollny, A. A. Young, and A. Suinesiaputra, "An Open Benchmark Challenge for Motion Correction of Myocardial Perfusion MRI," *IEEE Journal of Biomedical and Health Informatics*, vol. 21, no. 5, pp. 1315–1326, 2017.

[86] "Perception and Decision Laboratory (PDL), University of Illinois. \\ http://perception.csl.illinois.edu/matrix-rank/home.html."

[87] E. Candes, X. Li, Y. Mia, and J. Wright, "Robust principal component analysis?," *Neural computation*, vol. 21, no. 11, pp. 3179–3213, 2009.

[88] B. K. Natarajan, "Sparse Approximate Solutions to Linear Systems," *SIAM Journal on Computing*, vol. 24, no. 2, pp. 227–234, 1995.

[89] Z. Lin, R. Liu, and Z. Su, "Linearized Alternating Direction Method with Adaptive Penalty for Low-Rank Representation," in *NIPS*, 2011.

[90] C. M. Scannell, A. D. M. Villa, J. Lee, M. Breeuwer, and A. Chiribiri, "Robust Non-Rigid Motion Compensation of Free-Breathing Myocardial Perfusion MRI Data," *IEEE Transactions on Medical Imaging*, vol. 38, no. 8, 2019.

[91] A. Krizhevsky, I. Sutskever, and G. E. Hinton, "Imagenet classification with deep convolutional neural networks," in *Advances in Neural Information Processing Systems 25* (F. Pereira, C. J. C. Burges, L. Bottou, and K. Q. Weinberger, eds.), pp. 1097–1105, Curran Associates, Inc., 2012.

[92] O. Russakovsky, J. Deng, H. Su, J. Krause, S. Satheesh, S. Ma, Z. Huang, A. Karpathy, A. Khosla, M. Bernstein, A. C. Berg, and L. Fei-Fei, "ImageNet Large Scale Visual Recognition Challenge," *International Journal of Computer Vision (IJCV)*, vol. 115, no. 3, pp. 211–252, 2015.

[93] G. Litjens, T. Kooi, B. E. Bejnordi, A. A. A. Setio, F. Ciompi, M. Ghafoorian, J. A. W. M. van der Laak, B. van Ginneken, and C. I. Sánchez, "A survey on deep learning in medical image analysis.," *Medical image analysis*, vol. 42, pp. 60–88, 2017.

[94] T. Leiner, D. Rueckert, A. Suinesiaputra, B. Baeßler, R. Nezafat, I. Išgum, and A. A. Young, "Machine learning in cardiovascular magnetic resonance: Basic concepts and applications," 2019.

[95] L. Tautz, O. Friman, A. Hennemuth, A. Seeger, and H.-O. Peitgen, "Automatic Detection of a Heart ROI in Perfusion MRI Images," *Bildverarbeitung für die Medizin 2011*, pp. 259–263, 2011.

[96] I. Goodfellow, Y. Bengio, and A. Courville, *Deep Learning*. MIT Press, 2016. http://www.deeplearningbook.org.

[97] O. Ronneberger, P. Fischer, and T. Brox, "U-Net: Convolutional Networks for Biomedical Image Segmentation," in *Medical Image Computing and Computer-Assisted Intervention – MICCAI 2015* (N. Navab, J. Hornegger, W. M. Wells, and A. F. Frangi, eds.), (Cham), pp. 234–241, Springer International Publishing, 2015.

[98] D. P. Kingma and J. Ba, "Adam: A Method for Stochastic Optimization," *Proceedings of the 3rd International Conference on Learning Representations (ICLR)*, 2014.

[99] C. M. Scannell, M. Veta, A. D. Villa, E. C. Sammut, J. Lee, M. Breeuwer, and A. Chiribiri, "Deep-Learning-Based Preprocessing for Quantitative Myocardial Perfusion MRI," *Journal of Magnetic Resonance Imaging*, vol. 51, no. 6, pp. 1689–1696, 2020.

[100] B. Romain, L. Rouet, D. Ohayon, O. Lucidarme, F. D'Alché-Buc, and V. Letort, "Parameter estimation of perfusion models in dynamic contrast-enhanced imaging: a unified framework for model comparison," *Medical Image Analysis*, vol. 35, pp. 360–374, 2017.

[101] M. Jerosch-Herold, N. Wilke, Y. Wang, G. R. Gong, A. M. Mansoor, H. Huang, S. Gurchumelidze, and A. E. Stillman, "Direct comparison of an intravascular and an extracellular contrast agent for quantification of myocardial perfusion," *International Journal of Cardiac Imaging*, vol. 15, no. 6, pp. 453–464, 1999.

[102] D. A. Broadbent, J. D. Biglands, A. Larghat, S. P. Sourbron, A. Radjenovic, J. P. Greenwood, S. Plein, and D. L. Buckley, "Myocardial blood flow at rest and stress measured with dynamic contrast-enhanced MRI: Comparison of a distributed parameter model with a fermi function model," *Magnetic Resonance in Medicine*, vol. 70, no. 6, pp. 1591–1597, 2013.

[103] F. Schwab, M. Ingrisch, R. Marcus, F. Bamberg, K. Hildebrandt, C. Adrion, C. Gliemi, K. Nikolaou, M. Reiser, and D. Theisen, "Tracer kinetic modeling in myocardial perfusion quantification using MRI," *Magnetic Resonance in Medicine*, vol. 73, no. 3, pp. 1206–1215, 2015.

[104] M. Betancourt, "A Conceptual Introduction to Hamiltonian Monte Carlo," *arXiv preprint arXiv:1701.02434*, 2017.

[105] C. M. Scannell, A. Chiribiri, A. D. Villa, M. Breeuwer, and J. Lee, "Hierarchical Bayesian myocardial perfusion quantification," *Medical Image Analysis*, vol. 60, p. 101611, 2020.

[106] H. Rahman, M. Ryan, M. Lumley, B. Modi, H. McConkey, H. Ellis, C. Scannell, B. Clapp, M. Marber, A. Webb, A. Chiribiri, and D. Perera, "Coronary Microvascular Dysfunction Is Associated With Myocardial Ischemia and Abnormal Coronary Perfusion During Exercise.," *Circulation*, vol. 140, no. 22, pp. 1805–1816, 2019.

[107] M. D. Cerqueira, N. J. Weissman, V. Dilsizian, A. K. Jacobs, S. Kaul, W. K. Laskey, D. J. Pennell, J. A. Rumberger, T. Ryan, M. S. Verani, and American Heart Association Writing Group on Myocardial Segmentation and Registration for Cardiac Imaging, "Standardized myocardial segmentation and nomenclature for tomographic imaging of the heart. A statement for healthcare professionals from the Cardiac Imaging Committee of the Council on Clinical Cardiology of the American Heart Association.," *Circulation*, vol. 105, no. 4, pp. 539–42, 2002.

[108] P. Virtanen, R. Gommers, T. E. Oliphant, M. Haberland, T. Reddy, D. Cournapeau, E. Burovski, P. Peterson, W. Weckesser, J. Bright, S. J. van der Walt, M. Brett, J. Wilson, K. J. Millman, N. Mayorov, A. R. Nelson, E. Jones, R. Kern, E. Larson, C. J. Carey, l. Polat, Y. Feng, E. W. Moore, J. VanderPlas, D. Laxalde, J. Perktold, R. Cimrman, I. Henriksen, E. A. Quintero, C. R. Harris, A. M. Archibald, A. H. Ribeiro, F. Pedregosa, P. van Mulbregt, A. Vijaykumar, A. P. Bardelli, A. Rothberg, A. Hilboll, A. Kloeckner, A. Scopatz, A. Lee, A. Rokem, C. N. Woods, C. Fulton, C. Masson, C. Häggström, C. Fitzgerald, D. A. Nicholson, D. R. Hagen, D. V. Pasechnik, E. Olivetti, E. Martin, E. Wieser, F. Silva, F. Lenders, F. Wilhelm, G. Young, G. A. Price, G. L. Ingold, G. E. Allen, G. R. Lee, H. Audren, I. Probst, J. P. Dietrich, J. Silterra, J. T. Webber, J. Slavič, J. Nothman, J. Buchner, J. Kulick, J. L. Schönberger, J. V. de Miranda Cardoso, J. Reimer, J. Harrington, J. L, "SciPy 1.0: fundamental algorithms for scientific computing in Python," *Nature Methods*, vol. 17, no. 3, pp. 261–272, 2020.

[109] R. Vallat, "Pingouin: statistics in Python," *Journal of Open Source Software*, vol. 3, no. 31, p. 1026, 2018.

[110] J. R. Panting, P. D. Gatehouse, G.-Z. Yang, F. Grothues, D. N. Firmin, P. Collins, and D. J. Pennell, "Abnormal Subendocardial Perfusion in Cardiac Syndrome X Detected by Cardiovascular Magnetic Resonance Imaging," *New England Journal of Medicine*, vol. 346, no. 25, pp. 1948–1953, 2002.

[111] K. D. Knott, C. Camaioni, A. Ramasamy, J. A. Augusto, A. N. Bhuva, H. Xue, C. Manisty, R. K. Hughes, L. A. Brown, R. Amersey, C. Bourantas, P. Kellman, S. Plein, and J. C. Moon, "Quantitative myocardial perfusion in coronary artery disease: A perfusion mapping study," *Journal of Magnetic Resonance Imaging*, 2019.

[112] N. Wilke, M. Jerosch-Herold, Y. Wang, Y. Huang, B. V. Christensen, A. E. Stillman, K. Ugurbil, K. McDonald, and R. F. Wilson, "Myocardial perfusion reserve: assessment with multisection, quantitative, first-pass MR imaging.," *Radiology*, vol. 204, no. 2, pp. 373–84, 1997.

[113] J. P. Pluim, S. E. Muenzing, K. A. Eppenhof, and K. Murphy, "The truth is hard to make: Validation of medical image registration," *Proceedings - International Conference on Pattern Recognition*, pp. 2294–2300, 2017.

[114] N. H. Pijls, W. F. Fearon, P. A. Tonino, U. Siebert, F. Ikeno, B. Bornschein, M. Van'T Veer, V. Klauss, G. Manoharan, T. Engstrøm, K. G. Oldroyd, P. N. Ver Lee, P. A. MacCarthy, and B. De Bruyne, "Fractional flow reserve versus angiography for guiding percutaneous coronary intervention in patients with multivessel coronary artery disease: 2-Year follow-up of the FAME (fractional flow reserve versus angiography for multivessel evaluation) study," *Journal of the American College of Cardiology*, vol. 56, no. 3, pp. 177–184, 2010.

[115] B. De Bruyne, N. H. Pijls, B. Kalesan, E. Barbato, P. A. Tonino, Z. Piroth, N. Jagic, S. Möbius-Winkler, G. Rioufol, N. Witt, P. Kala, P. MacCarthy, T. Engström, K. G. Oldroyd, K. Mavromatis, G. Manoharan, P. Verlee, O. Frobert, N. Curzen, J. B. Johnson, P. Jüni, and W. F. Fearon, "Fractional Flow Reserve–Guided PCI versus Medical Therapy in Stable Coronary Disease," *New England Journal of Medicine*, vol. 367, no. 11, pp. 991–1001, 2012.

[116] P. S. Douglas, U. Hoffmann, M. R. Patel, D. B. Mark, H. R. Al-Khalidi, B. Cavanaugh, J. Cole, R. J. Dolor, C. B. Fordyce, M. Huang, M. A. Khan, A. S. Kosinski, M. W. Krucoff, V. Malhotra, M. H. Picard, J. E. Udelson, E. J. Velazquez, E. Yow, L. S. Cooper, and K. L. Lee, "Outcomes of Anatomical versus Functional Testing for Coronary Artery Disease," *New England Journal of Medicine*, vol. 372, no. 14, pp. 1291–1300, 2015.

[117] M. C. Williams, A. Hunter, A. Shah, V. Assi, S. Lewis, K. Mangion, C. Berry, N. A. Boon, E. Clark, M. Flather, J. Forbes, S. McLean, G. Roditi, E. J. Van Beek, A. D. Timmis, D. E. Newby, T. Pawade, A. Flapan, A. Hargreaves, S. Leslie, S. Lewis, G. McKillop, J. Reid, J. Spratt, N. Uren, L. Clark, P. Craig, T. Barlow, C. McCormack, S. Shepherd, M. Bucukoglu, R. Parker, A. Krishan, F. Wee, A. Wackett, A. Walker, L. Milne, and K. Oatey, "Symptoms and quality of life in patients with suspected angina undergoing CT coronary angiography: A randomised controlled trial," *Heart*, vol. 103, no. 13, pp. 995–1001, 2017.

[118] D. J. Maron, J. S. Hochman, H. R. Reynolds, S. Bangalore, S. M. O'Brien, W. E. Boden, B. R. Chaitman, R. Senior, J. López-Sendón, K. P. Alexander, R. D. Lopes, L. J. Shaw, J. S. Berger, J. D. Newman, M. S. Sidhu, S. G. Goodman, W. Ruzyllo, G. Gosselin, A. P. Maggioni, H. D. White, B. Bhargava, J. K. Min, G. B. J. Mancini, D. S. Berman, M. H. Picard, R. Y. Kwong, Z. A. Ali, D. B. Mark, J. A. Spertus, M. N. Krishnan, A. Elghamaz, N. Moorthy, W. A. Hueb, M. Demkow, K. Mavromatis, O. Bockeria, J. Peteiro, T. D. Miller, H. Szwed, R. Doerr, M. Keltai, J. B. Selvanayagam, P. G. Steg, C. Held, S. Kohsaka, S. Mavromichalis, R. Kirby, N. O. Jeffries, F. E. Harrell, F. W. Rockhold, S. Broderick, T. B. Ferguson, D. O. Williams, R. A. Harrington, G. W. Stone, and Y. Rosenberg, "Initial Invasive or Conservative Strategy for Stable Coronary Disease," *New England Journal of Medicine*, vol. 382, no. 15, pp. 1395–1407, 2020.

[119] H. Xue, E. Tseng, K. D. Knott, T. Kotecha, L. Brown, S. Plein, M. Fontana, J. C. Moon, and P. Kellman, "Automated detection of left ventricle in arterial input function images for inline perfusion mapping using deep learning: A study of 15,000 patients," *Magnetic Resonance in Medicine*, vol. n/a, no. n/a, 2020.

[120] C. M. Scannell, P. van den Bosch, A. Chiribiri, J. Lee, M. Breeuwer, and M. Veta, "Deep learning-based prediction of kinetic parameters from myocardial perfusion mri," *arXiv Preprint arXiv:1907.11899*, 2019.

[121] R. Robinson, V. V. Valindria, W. Bai, H. Suzuki, P. M. Matthews, C. Page, D. Rueckert, and B. Glocker, "Automatic Quality Control of Cardiac MRI Segmentation in Large-Scale Population Imaging," pp. 720–727, Springer, Cham, 2017.

[122] B. Ruijsink, E. Puyol-Antón, I. Oksuz, M. Sinclair, W. Bai, J. A. Schnabel, R. Razavi, and A. P. King, "Fully Automated, Quality-Controlled Cardiac Analysis From CMR: Validation and Large-Scale Application to Characterize Cardiac Function," *JACC: Cardiovascular Imaging*, vol. 13, no. 3, pp. 684–695, 2020.